Ph.D thesis within the Warsaw-4-PhD Doctoral School at the

Institute of Physical Chemistry
Polish Academy of Sciences

Department of Soft Condensed Matter
Kasprzaka 44/52, 01-224 Warsaw

Novel Microfluidic Strategies for Droplet Generation and Flow Control with Applications in Biotechnology

Supervisor
Prof. Piotr Garstecki
Auxiliary supervisor
Dr. Marco Costantini

Ph.D. Candidate
M.Sc. Francesco Nalin

Warsaw, September 2023

“Io stimo più il trovar un vero, benché di cosa leggiera, che ’l disputar lungamente delle massime questioni senza conseguir verità nissuna.”

- Galileo Galilei

“I value more the discovery of a truth, even if it is about lightweight matters, than the lengthy debate of the greatest questions without achieving any truth at all.”

- Galileo Galilei

Acknowledgements

My deepest gratitude goes to the individuals and groups whose support and guidance have been fundamental in my journey towards completing this Ph.D. thesis.

First I acknowledge my supervisors: Prof. Piotr Garstecki for his inspiring discussions, support, and the opportunity to be a part of the lab, and Dr. Marco Costantini, whose remarkable passion for science, motivation, and unwavering support have served as a constant source of inspiration. They have truly been role models, and their guidance has been invaluable.

My sincere thanks go to Dr. Alex Dajkovic, who supervised my internship in Paris and continued to provide valuable support and mentorship even after the internship concluded, and to Dr. Witold Postek for engaging discussions and for suggesting my collaboration with Marco, which has been a pivotal part of my research journey.

I thank Dr. Ladislav Derzsi for his involvement during the early stages of my Ph.D. and within EVOdrops, and acknowledge Prof. Matteo Pierno, Dr. Daniele Filippi, and the LaFSI for the fruitful cooperation and positive working relationship throughout these years.

I am indebted to all the members and friends from room 137, groups 11 and 32, as well as the workshop of IChF, the colleagues at EVOdrops, Biomillenia and the Sci-Fi team for their invaluable camaraderie, collaboration, and support throughout my research journey.

I dedicate this page to express my heartfelt appreciation for the people who have offered invaluable non-scientific support. To my family, relatives, friends from university (particularly those in group 10, and my fellow Tommaso), as well as the everlasting Fun's Fans, my high school companions, and the friends from Warsaw, your enduring encouragement, emotional support, and firm faith in me have been truly priceless.

You all hold a special place in my heart, and you have contributed not only to shaping my personal growth but also to enriching my life in countless ways.

Funding acknowledgements

This thesis is part of a project that has received funding from the European Union's Horizon 2020 research and innovation programme under the Marie Skłodowska-Curie grant agreement No. 813786 (EVOdrops).

This project was developed within the Warsaw PhD School in Natural and BioMedical Sciences (Warsaw-4-PhD Doctoral School) at the Institute of Physical Chemistry of the Polish Academy of Sciences.

List of publications

Publications related to the thesis:

1. **Nalin F.**, Tirelli M.C., Postek W., Garstecki P., Costantini M. "Tunastep: Tunable Parallelized Step Emulsification for the Generation of Droplets with Dynamic Volume Control to 3D Print Functionally Graded Porous Materials" ***Lab on a Chip***, 2023, under revision. Pre printed on *arXiv:2307.05259*

2. **Nalin F.**, Escribano-Vazquez U., Kiselev A., Garstecki P., Loeffert D., Dajkovic A., "High-throughput culturomics of gut and oral microbiota using droplet microfluidics allows isolation of uncultured bacteria" ***FEMS Microbes***, 2023, under revision

Other publications:

3. Filippi D., Derzsi L., **Nalin F.**, Vezzani A., Ferraro D, Zaltron A., Mistura G., Pierno M., "Boost and Contraction of Flow by Herringbone Surface Design on the Microfluidic Channel Wall" ***Adv. Mater. Technol.***, 2023, **8: 2201748**.

4. Weber P., Cai L., Aguilar Rojas F. J., Garciamendez-Mijares C. E., Tirelli M. C., **Nalin F.**, Jaroszewicz J., Święszkowski W., Costantini M., Zhang Y. S., "Microfluidic Bubble-Generator Enables Digital Light Processing 3D Printing of Porous Structures" ***Aggregate***, 2023, **00, e409**.

Patents:

1. Pilz M., **Nalin F.**, Kwapiszewska K., Makuch K., Derzsi L., Hołyst R., *Układ mikroprzepływowy oraz sposób pomiaru wnikania cząstek do komórek adherentnych.* **P. 439015A1**, 2021.

Conferences:

1. **Nalin F.**, Pilz M., Kwapiszewska K., Derzsi L., Makuch K., Garstecki P., Hołyst R., "Accurate Measurement Of Drug Uptake Time Of Cancer Cells" ***MicroTAS***, 2021, **Poster presentation**.

2. **Nalin F**., Pilz M., Kwapiszewska K., Derzsi L., Makuch K., Garstecki P., Hołyst R., "Novel Method For The Accurate Quantification Of Drug Uptake Time In Cancer Cells" ***NanoBioTech***, 2022, **Poster presentation**.

3. **Nalin F.**, Pilz M., Kwapiszewska K., Derzsi L., Makuch K., Garstecki P., Hołyst R., "Accurate Measurement Of Drug Uptake Time Of Cancer Cells" ***MicroSymposium***, 2022, **Poster presentation**
   * This poster received the **Audience Award**.

4. **Nalin F.**, Tirelli M.C., Postek W., Garstecki P., Costantini M., "Tuna Step: A Tunable Step Emulsification For Dynamic Control Of Droplet Volume To 3D Print Functionally Graded Materials" ***MicroTAS***, 2023, **Oral presentation**.

5. **Nalin F.**, Tirelli M.C., Postek W., Garstecki P., Costantini M., "Tuna Step: Tunable Step Emulsification For 3D Printing Of Porously-Graded Functional Materials" ***NanoBioTech***, 2023, **Oral presentation**.

Other public presentations:

I gave talks at eight EVOdrops ITN seminars, and two international Sci-Fi meetings (From Scientists to Innovators for Industry - co-funded by the European Union EIT Health). I presented my findings in four PhD seminars, as well as regular group meetings at IChF and Biomillenia.

Abstract

The outstanding advancement of microfluidics during the past few decades has progressed from the early phases of pure development of microfluidic technologies to its widespread use as a versatile instrument for multiple scientific disciplines.
Simultaneously, biotechnologies have been progressively evolving towards innovative directions, with an increasing emphasis on tailoring medical treatments to the patient. This paradigm shift toward tailored therapies and personalized medicine provides new prospects for improving and transforming healthcare.
The role of microfluidics in this developing environment is crucial, thanks to outstanding properties such as good repeatability, precise controllability, and a high degree of customisation. The intrinsic versatility of microfluidics makes it perfect for developing *ad hoc* solutions in a variety of biological applications.
This thesis has been envisioned in this context with a clear goal to develop microfluidic-based solutions for current relevant biotechnological challenges.
We introduce novel methodologies, such as the one detailed in Chapter 2, where the precise flow control of microfluidics enables to measure the drug uptake times in cancer cells with unprecedented temporal resolution.
In Chapter 3, we show how a microfluidics-driven workflow, enables the isolation and cultivation of previously uncultured bacteria from the human gut microbiota.
Furthermore, this work explores the potential for innovative microfluidic technologies, as demonstrated in Chapter 4. Here, a novel strategy for generating droplets with dynamic control over their volume range is

introduced.
The integration of this system within a 3D printing platform is further analyzed on chapter 5, allowing the manufacture of porous, functionally graded soft hydrogels that are relevant for the advancement of tissue engineering.
In summary, in an era marked by the convergence of microfluidics and personalized medicine, this thesis illuminates the transformational potential of microfluidic technologies, revealing unique approaches and creative solutions very promising for the development of biotechnology and healthcare.

Streszczenie

Wybitny postęp w dziedzinie mikrofluidyki w ciągu ostatnich kilkudziesięciu lat przeszedł od wczesnych faz czystego rozwoju technologii mikrofluidycznych do jej powszechnego wykorzystania jako wszechstronnego narzędzia w wielu dziedzinach naukowych.
Równocześnie biotechnologie stopniowo ewoluują w innowacyjnym kierunku, ze wzrastającym naciskiem na dostosowanie leczenia medycznego do potrzeb pacjenta. Ta zmiana paradygmatu ku dostosowanym terapiom i medycynie personalizowanej otwiera nowe perspektywy poprawy i transformacji opieki zdrowotnej.
Rola mikrofluidyki w tym dynamicznym środowisku jest kluczowa, dzięki wyjątkowym cechom, takim jak wysoka powtarzalność, precyzyjna kontrolowalność i wysoki stopień dostosowania. Wszechstronność mikrofluidyki sprawia, że jest doskonała do opracowywania mikroprzepływowych rozwiązań dostosowanych do różnorodnych zastosowań biologicznych.
Ta praca doktorska została stworzona w tym kontekście z wyraźnym celem opracowania rozwiązań dla bieżących wyzwań biotechnologicznych.
Przedstawiamy nowatorskie metody, takie jak ta opisana w Rozdziale 2, gdzie precyzyjna kontrola przepływu mikrofluidyki pozwala na pomiar czasu absorpcji leku przez komórki nowotworowe z niespotykaną rozdzielczością czasową.
W Rozdziale 3 pokazujemy, jak mikrofluidyczny przepływ pracy umożliwia izolację i hodowlę wcześniej niehodowlanych bakterii z mikrobioty jelitowej człowieka.
Ponadto, ta praca bada potencjał innowacyjnych technologii mikrofluidycznych, jak to zostało zademonstrowane w Rozdziale 4. Przedstawiono nowatorską strategię generowania kropel z dynamiczną kontrolą nad ich

zakresem objętości.
Integracja tego systemu w platformę druku 3D jest dodatkowo analizowana w Rozdziale 5, co umożliwia produkcję porowatych, funkcjonalnie ocenionych miękkich hydrożeli, które są istotne dla rozwoju inżynierii tkankowej.
Podsumowując, w erze wykorzystywania mikrofluidyki na potrzeby medycyny spersonalizowanej, ta praca doktorska odkrywa potencjał transformacyjny technologii mikrofluidycznych, ujawniając unikalne podejścia i kreatywne rozwiązania, które mają ogromny potencjał dla rozwoju biotechnologii i opieki zdrowotnej.

Contents

1 Introduction

Contents

The study of fluids has fascinated scientists for centuries, from the formulations of Archimedes on buoyancy to the development of the Navier-Stokes equation. This path, adorned by illustrious figures such as da Vinci, Euler, Bernoulli, and many more, has guided us to contemporary fluid dynamics, elucidating the intricate nature of fluid behavior, and enabling groundbreaking advances in engineering and scientific applications.
Fluid dynamics encompasses a wide range of phenomena, from the macroscopic currents regulating the oceans and the weather patterns, to the microscopic flow of blood within our bodies.
As we will see in the following sections, the scale at which fluid dynamics is examined plays a central role, since it determines the dominant forces, flow patterns, and transport properties. This thesis project is primarily focused on microfluidics, which is the study of fluids at the microscale, as well as the application of this knowledge. In section 1.1 we introduce microfluidics and discuss the main phenomena that are relevant to this thesis. In section 1.2 we discuss common methods that improved our understanding and the applicability of microfluidics. In section 1.3 we discuss three applications of microfluidics that are in the interest of this thesis.

1.1 Principles of Microfluidics

Physics of fluids at the microscale In Physics of fluids, one major difference between macro and micro scales is the different contribution of forces. At the micro scale, where the characteristic length and velocity are small, the influence of viscous forces and molecular interactions dominates over inertial forces. This disparity of forces is responsible for a vast range of events that affect our daily lives, as well as numerous practical applications.
In this section we focus on three aspects of fluids at the microscopic

scale that affected undoubtedly the experiments during this thesis: in subsection 1.1.1 we describe the effects on the flow of a single phase fluid, in subsection 1.1.2 we discuss the interaction at the interface between two fluids and the surface forces, and in subsection 1.1.3 we discuss the contact between three phases that originates wetting.

1.1.1 Laminar Flow

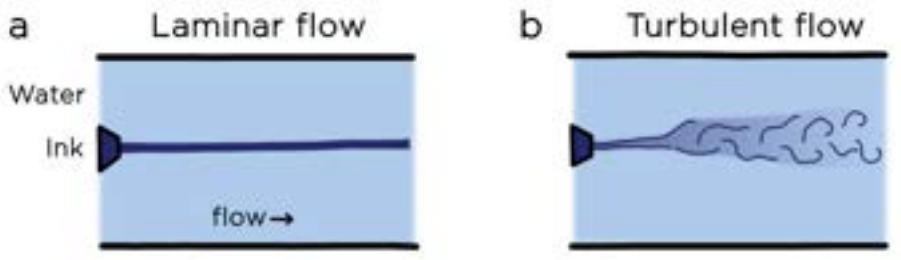

Figure 1.1: A stream of ink in water in conditions of laminar flow (**a**) and in conditions of turbulent flow (**b**)

In 1883, Osborne Reynolds made a remarkable observation on the effects of viscous forces in different regimes of fluid dynamics, reinforcing the notion previously offered by George Stokes [1, 2]. He injected a narrow stream of ink into a bigger stream of water, and observed how the path of the ink stream altered with flow rates. This allowed to identify two regimes. At low flow rates, the ink followed a straight course (Figure 1.1 **a**), whereas an uneven path with chaotic movements was seen at high flow rates (Figure 1.1 **b**). The first regime is known as *laminar* flow because the fluid flows in parallel layers, whereas the second is known as *turbulent* flow because of the disorganized routes. The shift between these two regimes was measured using a parameter named after him: Reynolds' number

$$Re = Ud/\nu \tag{1.1}$$

where U is the mean velocity of the fluid, d is the diameter of the tube, and ν is the kinematic viscosity that characterizes the liquid (see the following paragraph). Even considering different systems, we can observe the transition between laminar and turbulent flows at $Re \sim 2000$.
The Reynolds number is a dimensionless variable that represents the ratio of inertial forces to viscous forces. In the low Reynolds number regime, typically encountered in microfluidic systems, viscous forces act as a governing factor, resulting in the absence of turbulent flows, the prevalence of laminar flow patterns, and the tendency of fluid streams to exhibit high stability and predictable behaviour. These characteristics make low Reynolds number flows ideal for precise control and manipulation, forming the basis for microfluidic applications.

Viscosity One critical parameter in equation 1.1 is viscosity, which is a property of all fluids. Viscosity is a measure of the resistance of fluids to flow and has lower values for liquids that flow more easily.
As an example, one can consider honey and water: the lower viscosity of water allows it to stream more freely from the tap than honey pouring from the spoon.
Experimentally, the viscosity is often determined by comparing the force required to deform a fluid with the resulting degree of deformation. When viscosity is higher, one will observe less deformation under the same shear stress.
This approach allows for the classification of fluids into categories based on their viscosity. Fluids that exhibit a linear relationship between applied stress and shear rate are called *Newtonian* fluids, and all the other fluids fall under the category of *non-Newtonian* fluids. The viscosity of non-Newtonian fluids does not assume only a single, fixed value but rather exhibits different values in relation with the level of shear stress.

Poiseuille Flow The most relevant example of laminar flow in microfluidics is called *Poiseuille* flow, after the French physicist Jean Léonard Marie Poiseuille. This phenomenon characterizes the flow of viscous fluids pushed through parallel plates by a pressure gradient without moving the plates, and can be extended to describe the flow in a round tube (*circular Poiseuille flow*) [1].

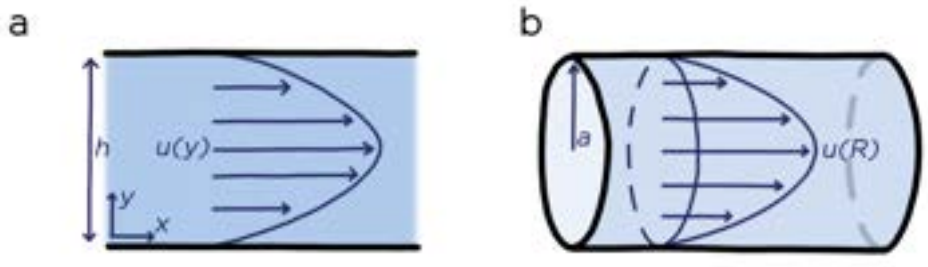

Figure 1.2: Scheme of velocity profiles for Poiseuille flows in square (**a**) and round (**b**) channels.

When a constant pressure gradient ($dp/dx \neq 0$) is applied across the ends of two plates parallel to x and located at $y = 0$ and $y = h$, the fluid moves steadily and uniformly, and the velocity of the flow $u(y)$ follows a parabolic profile (Figure 1.2, **a**).

$$u(y) = -\frac{1}{2\mu}\frac{dp}{dx}y(h-y) \tag{1.2}$$

Similarly, in a round tube aligned along x and with radius a, a pressure gradient dp/dx would cause a parabolic velocity profile with its maximum in the center of the tube and decreasing towards the tube wall (Figure 1.2, **b**).

$$u(R) = \frac{R^2 - a^2}{4\mu}\frac{dp}{dx} \tag{1.3}$$

Because these two scenarios depict square and circular channels, they provide a decent notion of flow regimes in microfluidics; hence, we will not explore this section further. Nevertheless, there are certain immediate cases where these descriptions would not apply:

- serpentine channels and patterned microchannels where the geometry is intentionally adjusted to interrupt the laminar flow and facilitate mixing between layers.
- non-Newtonian fluids, where the viscosity depends on the applied shear stress and hence the flow profiles are different.

1.1.2 Surface Tension

Surface tension is a fascinating property of a liquid that arises from the cohesive forces between molecules. When the attraction between molecules is stronger than the thermal agitation, molecules stick together and prefer a liquid phase over a gas phase. Since molecules in bulk encounter attractive forces from a greater number of neighbors than molecules on the surface, liquids try to minimize the surface area assuming the lowest energy structure [3](Figure 1.3, **a**).
The ease in creating surfaces on a liquid can be characterised with the surface tension γ which relates the supplied energy dW and the increase in surface area dA.

$$dW = \gamma \cdot dA \tag{1.4}$$

The minimization of surface area underpins various intriguing phenomena, for example the spherical shape of droplets and bubbles, or the mesmerizing ability of water bugs to traverse effortlessly across the smooth surface of tranquil ponds.
The energy required to create curved interfaces explains the work necessary

to form foams and emulsions, as well as the challenging issue of maintaining their stability over time. As we will see in the following paragraph, the size and curvature of droplets determine their stability.

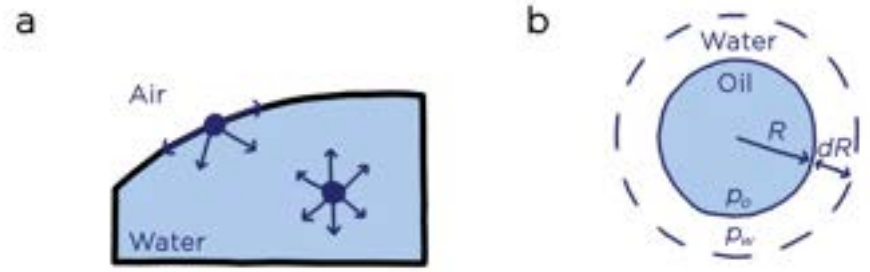

Figure 1.3: (**a**) Scheme of two molecules in a drop of water. The contribution of attractive forces is lower at the surface. (**b**) Scheme of an oil droplet surrounded by water.

Laplace Pressure The energy required to form curved surfaces is at the root of the overpressure observed in the interior of droplets and bubbles. Laplace defined the relationship between surface curvature and overpressure in 1805, and we can study it with an oil droplet in equilibrium in a water phase (Figure 1.3 **b**) [3].
He calculated the work dW done by capillary force and pressure as

$$dW = p_w dV - p_o dV + \gamma dA \tag{1.5}$$

where dV is the increase in volume of the drop, dA is the increase in surface, p_o and p_w are the pressures of oil and water phases. With a shift in coordinates ($dV = 4\pi R^2 dR$ and $dA = 8\pi R dR$) and at the mechanical equilibrium $dW = 0$, we obtain

$$\Delta p = p_o - p_w = \frac{2\gamma}{R} \tag{1.6}$$

This equation can be generalised to describe a non-spherical surface by introducing the curvature $C = (\frac{1}{R_1} + \frac{1}{R_2})$ where R_1 and R_2 are the

two radii of curvature of the surface. In this case, the difference in hydrostatic pressure will be

$$\Delta p = \gamma C \tag{1.7}$$

Laplace pressure may be used to explain a variety of phenomena, for example, in an emulsion we observe *Ostwald's ripening*: tiny droplets have a lower stability and disappear over time in favour of larger ones. Furthermore, this notion is important in comprehending the step emulsification process discussed in section 1.2.

1.1.3 Wetting

So far, we discussed the physics of a single phase flowing in microchannels and the interaction between two phases. An equally relevant case is the contact between three phases, known as *wetting*, as it holds pertinence in numerous applications, including microfluidics [3].

A simple illustration of this phenomenon is observed when a water droplet rests on a tabletop. In this particular scenario, the droplet represents the liquid phase, making contact with both the solid phase of the table and the gas phase of the surrounding air. Based on the nature of the tabletop material, the water droplet can either readily spread out, maximizing its surface area, or maintain a rounded shape. This fundamental distinction leads to the classification of wetting into two types: *total wetting* and *partial wetting* (Figure 1.4, **a**).

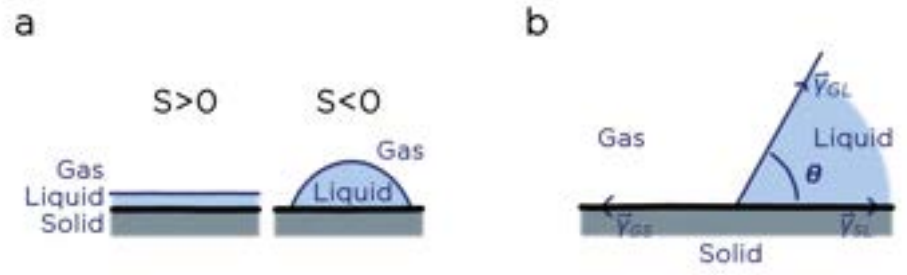

Figure 1.4: (**a**) Scheme of total ($S > 0$) and partial ($S < 0$) wetting. (**b**) Scheme of the contact angle θ in relation to the surface tensions between solid, liquid and gas phases.

We introduce the spreading parameter S to distinguish between these two scenarios. S denotes the difference in surface energy between a dry substrate and a wet substrate:

$$S = [E_{substrate}]_{dry} - [E_{substrate}]_{wet} \tag{1.8}$$

When $S > 0$ we observe total wetting, and when $S < 0$ the partial wetting appears.

In the second case, when the liquid does not spread to cover the whole surface, we observe a round cap wetting only a part of the substrate. The shape of the cap depends once again on the interaction between phases, and can be quantified with the *contact angle* θ between the drop and the substrate (Figure 1.4, **b**).

The angle can be calculated at the line of contact between three phases, and it will appear at the equilibrium between three capillary forces: $\vec{F}_{GL}$, $\vec{F}_{GS}$ and $\vec{F}_{LS}$ corresponding to the forces between gas-liquid, gas-solid and liquid-solid phases. From the projection on the solid plane we obtain

$$F_{GS} - F_{LS} - F_{GL}cos\theta = 0 \tag{1.9}$$

After the normalization of forces to a unit length, we obtain

$$\gamma_{GL}cos\theta = \gamma_{GS} - \gamma_{LS} \tag{1.10}$$

Finally, substituting the definition of $S = [\gamma_{GS} - (\gamma_{LS} + \gamma_{GL})]$ we obtain the law of *Young-Dupré*

$$S = \gamma_{GL}(cos\theta - 1) \tag{1.11}$$

These principles, including the concept of the contact angle, extend beyond systems where the three phases are limited to gas-liquid-solid interactions. For example when a water droplet is enclosed by oil within microfluidic channels.
When discussing a surface and its contact angle in relation to water, we categorize it as *hydrophilic* if $\theta < 90°$, and *hydrophobic* if $\theta > 90°$.

1.2 Methods of Microfluidics

1.2.1 Soft Lithography

Since its introduction in the early 1990s, *soft lithography* revolutionized the way microfluidic devices are developed and manufactured [4, 5].
Whitesides and colleagues introduced elastomeric materials for the replication of features and patterns, enabling the fabrication of sophisticated fluidic structures with high precision and versatility, quickly establishing polydimethylsiloxane (PDMS) as a cornerstone of microfluidics. PDMS offers remarkable features such as optical transparency, biocompatibility, and ease of fabrication, making it an ideal choice for the creation of microchannels and structures.
The standard soft lithography protocol consists of a few key steps. First, a master mold is fabricated using traditional photolithography techniques[6, 7] or other methods such as micromilling[8] or laser ablation[9]. The master mold contains the desired pattern or structure that will be replicated in the final device. Next, the uncured PDMS is poured onto the master mold and baked to create a flexible replica of the mold. This PDMS replica, can then be used as a master to obtain positive replicas, or bonded with

another surface to obtain microchannels.

Plasma activation of PDMS and glass surfaces is the standard method for bonding PDMS[4, 5, 10] (Figure 1.5). A brief exposure to plasma (one minute is sufficient) breaks the bonds on the PDMS surface, removing the hydrocarbon groups and freeing silanol groups (Si-O-H). When we position the PDMS on plasma-treated glass slides, the silanol groups of PDMS interact with the OH groups of the glass, establishing covalent Si-O-Si bonds with the release of water molecules, and permanently sealing the glass slide to the PDMS (Figure 1.5). Other popular methods for bonding PDMS, especially relevant to create multilayer PDMS devices, are discussed in subsection 1.2.6.

The simplicity and relative low cost of soft lithography increased the accessibility to microfluidics, and accelerated innovation in the field. At the same time, in a mutually beneficial relationship, the interest in these materials increased thanks to the microfluidic applications that appeared during time.

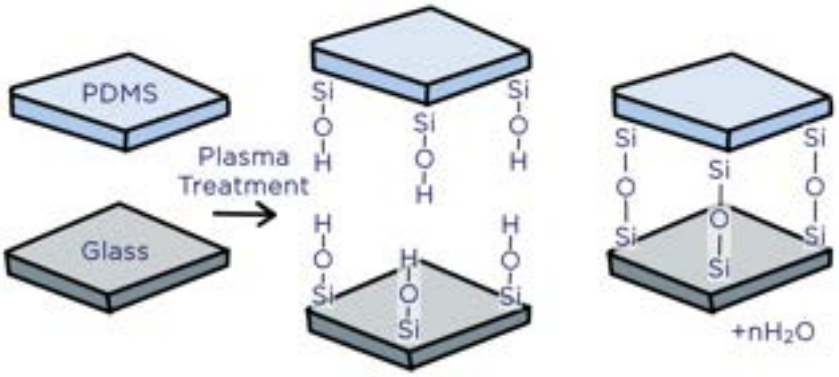

Figure 1.5: Bonding cured polydimethylsiloxane with a glass slide: The plasma treatment activates the surfaces of glass and PDMS, and when put in contact they form Si-O-Si covalent bonds with release of water molecules.

1.2.2 Surfactants

In subsection 1.1.2 we discussed the mechanism of surface tension γ and how it impacts the stability of interfaces in droplets and bubbles. Of course, lowering γ improves the process of droplet generation and the stability of droplets, since it allows to lower the energy necessary to increase the area of interfaces.

Effective strategies for lowering surface tension are part of our everyday life: detergents for dishes or laundry are one obvious example. Adding a few drops of soap to a sponge not only aids in eliminating oil residues from dishes but also leads to the formation of visible foams.

This fascinating phenomenon is made possible by the inclusion of *surfactants*, compounds that lower the surface tension of liquids [3, 11]. As a result, droplets are readily formed from the oil stains, and their stability is maintained, allowing them to seamlessly flow with the water.

Surfactants are molecules with two distinct parts, where each part exhibits affinity for either the oil or water phase. This is due to the chemical composition of surfactants: they have an hydrophilic head and a hydrophobic tail (Figure 1.6 a). The hydrophobic tail is generally formed by one or more aliphatic chains $CH_3(CH_2)_n$, therefore it has higher affinity with the similar oil molecules. The hydrophilic part could be an ion, forming a polar head that prefers polar liquids like water, or it could be a short chain of neutral units soluble in water. Thanks to this structure, when we add surfactants to a mixture of water and oil, they readily position at the interface between the two liquids (Figure 1.6 b), taking the inconvenient place of water and oil molecules, and lowering the surface tension [3, 12, 13].

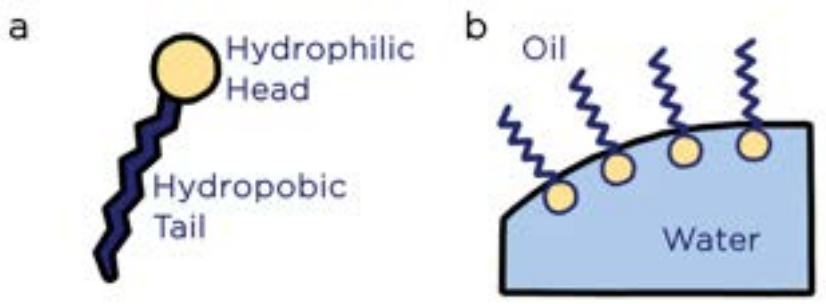

Figure 1.6: Schemes of (**a**) structure of surfactants, and (**b**) surfactant disposition on the surface of a water droplet surrounded by oil.

Surfactants in Microfluidics Surfactants are important in microfluidics because of their unique capacity to regulate the characteristics at the interface between phases and hence enhance the performance of microfluidic devices. Surfactants are widely employed to stabilize the droplet interface and prevent droplet coalescence, which is the essential requirement for using droplets as microreactors [14, 15].

We can identify three major processes in which emulsion stability is threatened and surfactant selection is critical: i) *coalscence* [16], ii) *Ostwald's ripening* [17], iii) *phase partitioning* [18].

Coalescence occurs naturally to lower the surface energy of the emulsion, causing the droplets to merge over time. Surfactants slow down this process via two mechanisms: (i) They cause repulsion between droplets due to surfactant steric repulsion; (ii) the movement of droplets generates surfactant gradients at the droplet interfaces. These gradients in surfactant concentration create gradients in surface tension that pull the liquids to the area with the highest surface tension for the mechanism called Marangoni effect [3, 11, 15]. This induces a thickening in the continuous layer between two droplets, making the emulsion more stable.

Ostwald's ripening is the gradual increase in droplet size with the smaller droplets dissolving in the larger ones. This is a consequence of the higher Laplace pressure experienced from the smaller droplets (subsection 1.1.2).

One approach to reduce this phenomenon is based on osmotic pressure: by introducing molecules in the droplets that are not soluble in the oil, we can increase the osmotic pressure of the disperse phase, reducing the exchange of the disperse phase.

Finally, droplet stability can be compromised by direct partitioning of the dispersion phase into the continuous phase or the formation of freely moving micelles. The selected continuous phase should not allow a high solubility of disperse phase to avoid partitioning. To avoid the formation of micelles, the concentration of surfactants must be carefully chosen: below the *critical micelle concentration*, surfactants are free to diffuse along the droplet interface, but once this concentration is achieved, they tend to separate from the droplets [19].

Another critical aspect to consider in microfluidics applications, particularly in biomedical and biological investigations, is *biocompatibility*. The reaction should be as efficient in droplets as in bulk, therefore, testing surfactant biocompatibility is required to guarantee that surfactants do not jeopardize the viability, functioning, or integrity of the biological entities being examined or modified inside the microfluidic platform. Moreover, surfactants have been reported to interfere with investigations because their ionic head groups may interact with biomolecules such as nucleic acids or proteins, gathering these molecules towards the droplet surface [20]. Therefore, several solutions have been reported, suggesting different surfactants for different microfluidic applications [14, 21–24].

1.2.3 Surface Modification

Figure 1.7: A few water droplets deposited on blades of grass after a rainy day in Warsaw. The surface properties of the grass influence shape and sliding of the droplets.

The properties of surfaces assume a pivotal role in microfluidics, since they influence the behaviours and interactions of fluids at the microscale. Surface qualities such as wettability, roughness, and chemical composition have such an impact on fluid flow that a slight modification can enable or prevent the success of experiments. Moreover, in biological experiments, the chemical composition might have an enormous impact in terms of biocompatibility. For these reasons, scientists developed several strategies to modify the surface properties of microchannels.

The majority of techniques for surface modification rely on physical or chemical methods, or on the combination of both [25, 26]. Physical methods involve altering the surface topography through techniques like plasma treatment [27], laser ablation [28], or nanoimprinting [29], while chemical methods utilize functional groups [30] or coatings [31] to modify

the surface chemistry. Additionally, methods relying on biology utilized biomolecules [32] to achieve the desired surface properties. These surface modifications provide tailored solutions for diverse applications, including sample preparation, cell manipulation, drug delivery, and biosensing. Overall, surface modification techniques offer an extensive toolbox for researchers to customize and optimize microfluidic systems.

1.2.4 Droplet Microfluidics

One fundamental branch of microfluidics deals with the study and manipulation of discrete droplets in microscale environments, and therefore it is called *droplet microfluidics*. Droplets can be used as microcompartments, allowing to confine chemical or bio-reactions in discrete volumes, with unique features such as i) high-throughput parallelization of the reactions, ii) automated handling of the reactions, iii) reduced reagent consumption, and iv) study of parameters that would be challenging or impossible to measure [33].
The working principle of droplet microfluidics is combining two immiscible phases (usually oil and water) to obtain an emulsion with controllable droplet volume, concentration of reagents and allowing further droplet manipulation.

Methods for droplet generation Several ways to generate droplets have been published and successfully applied since the inception of microfluidics.

One simple and effective chip design for the generation of droplets is the *T-junction* (Figure 1.8, **a**) [34]. The liquid phase to-be-dispersed flows into a T-shaped junction, where it breaks thanks to the side flow of continuos

phase. This design is particularly suitable since it allows to control the droplet size with different droplet generation regimes depending on the flow rates, but also with the active control of the two phases to generate droplets-on-demand (DOD) [35].

Flow focusing is one of the most extensively used technologies due to its simple chip design, which consists of a cross-shaped junction where a liquid phase is pushed and split into droplets by two side flows of continuous phase (Figure 1.8, **b**) [36]. This arrangement enables robust droplet formation as well as variable droplet size management in proportion to the flow rates of the two phases. One disadvantage of this technology is its inability to scale up: the reliance on flow rates renders its design unsuitable for parallelization. Furthermore, the volume fraction between dispersed and continuous phases depends significantly on droplet size and throughput.

Another versatile approach to generate droplets is the *co-flow* [37], where two coaxial channels inject the stream of the dispersed phase into the continuous phase (Figure 1.8, **c**). This design is particularly suitable for core-shell systems and it can easily be extended to generate double emulsions (typically Water-in-Oil-in-Water or Oil-in-Water-in-Oil emulsions). The size of droplets in this system is highly dependent on the flow rates, making this design not easy to parallelize. Moreover, the first reported designs were based on coaxial pulled capillaries difficult to replicate and therefore requiring a new characterization for every new chip. The advent of 3D printed microchips increased the appeal of these systems in recent times [38].

Step emulsification, discussed more in details in subsection 1.2.5, is a robust method for droplet generation, in which the disperse phase is pushed through a narrow constriction until it meets a sharp change in

channel height (the step) and enters into a wide emulsification chamber filled with the external phase (Figure 1.8, **d**). Then, the dispersed phase assumes a spherical shape and spontaneously splits into a droplet with a volume hard-wired to the geometry of the emulsifying nozzle. The diameter is almost not depending on the flow rates as long as they are less than a critical value. This method is differentiated from the others by its simplicity of parallelization and ability to achieve suitable volume fractions between the two liquid phases [39].

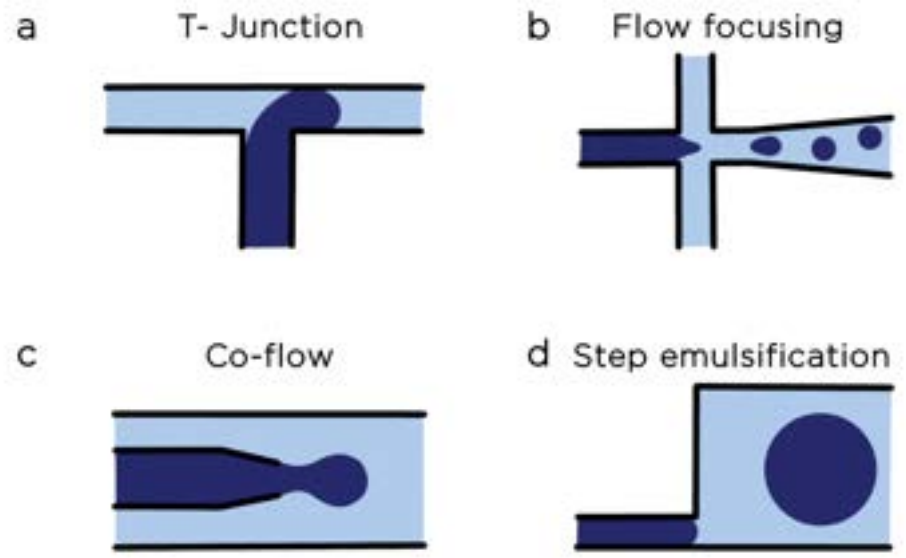

Figure 1.8: Schemes of different microfluidic strategies to generate droplets: (**a**) T-junction, (**b**) Flow-focusing, (**c**) Co-flow, and (**d**) Step Emulsification

Methods for droplet control and further manipulation Besides droplet generation, several techniques have been developed to complete the microfluidics toolbox with the further manipulation and control of droplets. External forces, like electric fields[35, 40] or acoustic waves[41, 42], are used in active manipulation methods to move[41], merge[35], split[43], and sort droplets[40, 42] as required. Passive manipulation, on

the other hand, uses the geometry[44, 45] and surface properties[46] of the chip to guide and restrict droplets, allowing activities such as trapping[45] and sorting[44].
These technologies, both active and passive, make microfluidics a viable tool for a wide range of applications while still leaving room for advancement of the present technology.

Overall, droplet microfluidics includes many well-established technologies, that enabled to explore diverse applications including single-cell analysis, high-throughput screening, emulsion-based chemical reactions, drug encapsulation, and diagnostic assays. Even if many of these applications rely on microfluidics as a tool and prefer robust and tested methods, some aspects still have room for improvement, such as increasing droplet generation throughput, or improving the control over droplet volume, material compatibility and volume fraction.
Integrating microfluidics with other technologies is not an obvious task, often the complexity of the system is increased, requiring experienced researchers to carry on the tasks. Droplet stability, crosstalk between droplets and potential issues in material compatibility might cause additional problems.

1.2.5 Step Emulsification

Droplet production using step emulsifiers - or Step Emulsification - is a popular droplet generation approach that plays an important part in this thesis. Keeping a consistent droplet volume guided from the chip design, and the ability to manufacture monodisperse droplets while changing the volume fraction of the final emulsion, are defining characteristics of this technology. As long as the flow rates are below a threshold value, variations in flow rates will have little effects on the diameter of the droplets. This

phenomenon, together with the simple geometry of the emulsifying nozzle, makes step emulsification particularly appealing for huge parallelization, resulting in high-throughput formation of monodisperse droplets that is difficult to match by other conventional droplet generation methods.

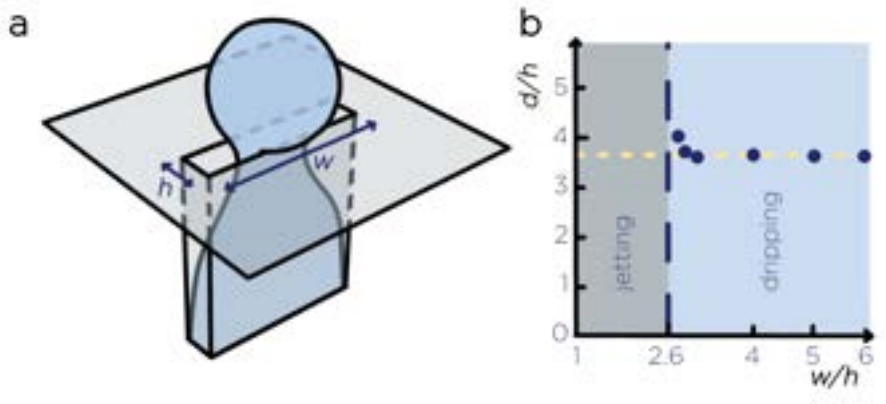

Figure 1.9: (**a**) Scheme of step emulsification in a nozzle with height h and width w, (**b**) Scheme of normalised droplet diameter (d/h) in function of the w/h ratio. Droplets are generated when $w/h \sim 2.6$ and the diameter assumes a constant value for $w/h > 4$.

Mechanism of Step Emulsification The mechanism below step emulsification has been widely studied with detailed theoretical explanations and numerical simulations [39, 47–50].

The phase to-be-dispersed is pushed through a wide and narrow constriction, where it assumes a pancake-like shape that is particularly unfavourable for the small radius of curvature and the high Laplace pressure that is resulting (equation 1.7). A sudden increase in the channel height frees the liquid phase that assumes a more convenient spherical shape with a larger radius of curvature and a lower Laplace pressure (Figure 1.9, **a**). Then, the pressure gradient brings the liquid phase inside the sphere, and if the nozzle does not provide enough liquid (namely, the

flow rate is low enough) a thin neck is formed between the sphere and the pancake-shaped interfaces. When the difference in pressures is high enough, the neck disappears and the sphere can finally separate from the continuous phase, forming the droplet.

The flow regime low enough to produce the neck and generate droplets is known as *dripping* regime, and it differs from the *jetting* regime, in which the liquid flows too quickly and the neck cannot form.
It has been shown how the ratio between the nozzle width w and height h plays a key role in this process: below $w/h \sim 2.6$ a smooth transition appears and the droplets cannot be generated, while, above $w/h \sim 4$, the droplet diameter appears to be independent on the width (see scheme in Figure 1.9, **b**).
The nozzle height can be considered the crucial parameter since simulations and experiments agree that the droplet diameter $d \sim 4h$ in the dripping regime [48].
Finally, it has been shown how the viscosity of the liquids affects the droplet generation process: as we may expect, more viscous fluids slow down the droplet generation process, characterising a decrease in the critical flow rate as the viscosity of the disperse phase increases[48, 51].

Overall, Step Emulsification has been widely studied and adapted for the high-throughput generation of droplets [39]or for the generation of double emulsions in a complex step [52] or in two cascaded devices [53], exploting this technology for its passive droplet generation [54], or to generate emulsions with a required volume fraction [55].
Some drawbacks of this technology that might make it less favourable than other standard techniques for droplet generation are i) the increase in channel height makes the chip fabrication more complex than a chip with a fixed height, ii) the communicating nozzles make it more difficult to clean the chip after use, and in case some of them would be clogged, it

would be tricky to wash them, and iii) once the chip is ready, it is not possible to change the height of the nozzle, meaning that the droplet size is fixed until a new chip is prepared.

1.2.6 Membranes and Actuators

One crucial aspect of microfluidics is the flow control. Even if the movement of liquids in microchannels can be highly predictable (section 1.1.1), more complex operations might require additional strategies. One example is given by *on-chip micro-valves*.
These are microfluidic components embedded in the chip that can be controlled to modify the chip design and regulate the fluid flow within the device [56].
The greatest advantage of these valves as opposed to external valves (for example electromagnetic valves) is that the flow of liquids can be controlled locally within the chip, allowing for rapid exchange of reagents and avoiding the contact between reagents and external valves.
The standard design relies on two layers of PDMS aligned on top of each other and bonded to a glass slide. The bottom layer is generally thin (thickness $\sim 100\ \mu$m) and includes some microchannels. In such a way, only a thin PDMS membrane divides the two layers. When an empty chamber on the top layer is overlapping with an empty chamber on the bottom layer, the membrane between them can be actuated. Generally, one layer is used for the flow of reagents (*flow layer*) and one is used for the control of the membranes (*control layer*). There are two standard configurations for these layers: the *push-up*, with the flow layer on top, and the bottom layer used to deflect the membrane and close the channels, and the *push-down* where the flow layer is on the bottom, and the control layer on top (Figure 1.10).

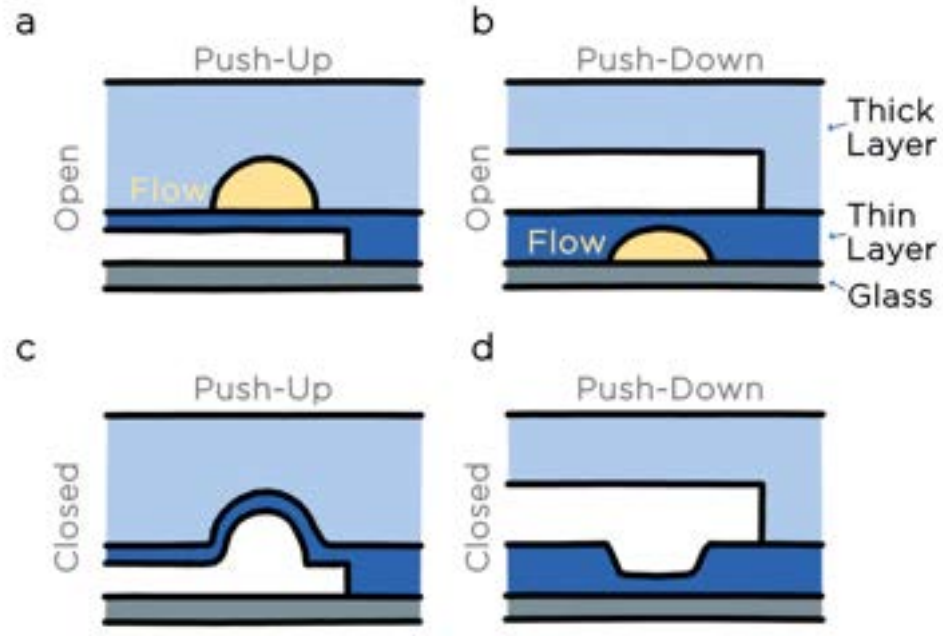

Figure 1.10: Scheme of on-chip microvalves in the push-up configuration (**a**) open and (**c**) closed, and in the push-down configuration (**b**) open and (**d**) closed.

The push-up configuration is easier to reproduce, since it can be actuated with lower pressures, and the pressurised air does not act against the bonding between the two PDMS layers, but on the bonding between glass and PDMS (generally stronger). Moreover, in the push-up configuration, even square-sectioned channels can be effectively closed, while the push-down configuration requires to fabricate round-section channels for the valve actuation, requiring a more complex process for fabrication of the masters. Nevertheless, there are good reasons to adopt the push-down configuration, for example, having the reagents in direct contact with the glass slide. This aspect might be crucial in some microscopy settings (for example when objectives have a low working distance) or in detection techniques that would be disturbed from the

thin PDMS layer.
Since the introduction of this technology, on-chip micro-valves showed interesting to control the flow, extending the design with multilayer lithography allowed to create multiplexed systems for the automated serial control of numerous valves within the same chip. The fabrication and control of these valves might be an obstacle that is stopping many scientists from adopting this technology, or in general, a good reason to reduce the number of valves and use them only when strictly necessary.

Common methods for PDMS-PDMS bonding The creation of PDMS devices involving two or more PDMS layers necessitates a process for bonding PDMS with PDMS. Various methods have been proposed for this purpose, with some similarities to the surface treatment techniques used in PDMS-glass bonding[57].
One commonly used approach involves plasma activation of the surfaces, similarly to the method employed in PDMS-glass bonding[58]. However, this technique has its limitations as it leads to an immediate bond between the PDMS surfaces, making it challenging to achieve precise alignment of the layers.
To address this issue, alternative methods have been explored. For example, using uncured or partially-cured PDMS[59]. Partially cured PDMS is relatively fragile, making it susceptible to tearing during the punching of microfluidic chip inlets. Therefore, it is advisable to perform the punching only once the PDMS is fully cured. Moreover, it is sticky, and therefore it is recommended to handle it in a clean-room to avoid gluing dust particles on the surfaces irreversibly.
Another effective approach involves employing two PDMS layers with different crosslinking agent-to-PDMS ratios[56]. The PDMS structures produced with this method have different elastic properties compared to standard PDMS, since the rigidity of the resulting structure increases

with a higher concentration of the crosslinking agent.
In Chapters 2 and 4 of this thesis, we adopted the *stamp-and-stick* approach. This technique involves stamping cured PDMS onto a carrier substrate previously coated with either uncured PDMS [60] or a curing agent[61]. The PDMS is then transferred to the final substrate, where it forms strong bonds. An advantage of the method described by *Samel* et al.[61], is that it enables to avoid plasma treatment and simplifies the alignment process, while using fully cured PDMS slices that are more resistant and easy to handle. The use of substrates coated with curing agent make this method particularly useful for large-scale production of microfluidic chips, since the substrates can be prepared in advance and stored for extended periods.

1.3 Applications of Microfluidics

The rapid development of microfluidics and its precise control and manipulation of fluid flow at a small scale revolutionized many scientific and technological fields, opening up new applications in healthcare, biotechnology, and material sciences.
In this section, we describe three applications of microfluidics that we explored within the thesis. These examples demonstrate the impact of microfluidics on scientific and technological advancements, and at the same time indicate areas where microfluidics still has room for innovation and exploration.

1.3.1 Cellular Uptake of Anticancer Drugs in Cancerous Cells

Understanding the structure and function of cells has been a focus of biologists for over a century[62–64], and lead to the definition of cells as

the smallest building blocks of living forms, characterized by a cellular membrane which encloses a cytoplasm, many macromolecules such as DNA, RNA, or proteins, as well as smaller molecules such as metabolites and nutrients.

More recently, scientists have concentrated on the activities inside the cell, as well as the interactions between the cell and external particles (such as drugs): these insights would not only expand our understanding of cell mechanisms, but would also be very useful in modern drug development[65, 66].

The cytoplasm can be described as a complex network of polymers containing a high concentration of macromolecules and organelles[63], and its complex structure makes it particularly difficult to explain the dynamics inside cells. As a consequence, describing the kinetics of biochemical reactions within cells is even more challenging, since diffusion and interactions between biomolecules are affected by the dynamics in the cytoplasm[66].

Recent studies [66–69] modelled the dynamics of small particles moving inside cells, or in cell agglomerates with the study of the effective viscosity of the cytoplasm at a nanoscale. These studies demonstated how the dynamics of particles can change in relation to their characteristics (size, shape, polarity), and they employed monolayers[66–68], or multicellular spheroids[69], to observe cells after they reach a stationary drug concentration (i.e. when the probes were already inside the cells).

The phenomenon of particles entering the cells, is called *cellular uptake*. Characterizing the uptake time of particles in cells, and more generally understanding the dynamics of these intricate phenomena, are fundamental steps to design modern drug treatments. Studies of cellular uptake of particles are generally executed in bulk, and with longer timescales (minutes/hours)[65, 70], due to the limitations in measuring such parameter. These investigations, especially at the single cell level, are particularly difficult, since they require a sensitive detection of the particles

within the cells, as well as rapid and regulated drug administration. Moreover, when the reagents are added to a bulk culture of cells, the relatively long diffusion time of reagents makes it impossible to quantify the cellular uptake with high-resolution in time.
In chapter 2, we present our new method to quantify cellular uptake time of anticancer drugs in cancerous cells, obtained by the combination of Time-Correlated Single-Photon Counting (TCSPC) with on-chip microvalves described in section 1.2.6.

1.3.2 Microfluidics for Single-cell Culturomics

The bacteria population that lives in our gastrointestinal tract is known as the Human Gut Microbiota (HGM). The state of health or disease of a human individual is greatly influenced by the composition and diversity of its microbiota [71–74].
An essential task of microbiology is to culture and isolate bacteria from the gut microbiota, since it allows to study their individual characteristics and functions, and provides potential therapeutic applications. Despite the dedication of researchers to this goal, the majority of species from the HGM are still considered "unculturable" i.e. they cannot be grown in laboratory with the current techniques [75–77].
The very unique characteristics of the gut environment create a bottleneck in the culture of its bacterial communities. Recreating these settings in the lab is difficult, not only because stringent anaerobic conditions must be maintained, but also because of the diversity of the microenvironments present in the gut and the particular growth requirements of the resident bacteria[78]. Furthermore, because different species and strains in the gut microbiome appear at widely varied rates, isolation attempts may result in growing the most abundant members of the consortium while completely ignoring the rare ones. Finally, many attempts to isolate environmental bacteria in the lab run into the dilemma of viable but

unculturable cells - bacteria that do not increase in biomass under typical laboratory settings, but can be demonstrated as viable[79].
As a result, the majority of knowledge on the bacterial community comes from culture-independent approaches that characterized community composition[80, 81], environmental influences[82, 83], and possible links between the gut microbial community and human health[84, 85].
At the same time, culture-independent methods do not offer a thorough picture of the gut bacterial ecology. Indeed, there is no distinction between the DNA collected from live or dead cells, causing issues of interpretation with abundance data and preventing comprehension of mechanistic functions of specific bacterial species in human physiology and illness without their isolation in laboratory culture. Furthermore, because to their low abundance, certain strains may not be discovered, or are detected poorly, by sequencing, therefore their whole genomes may not be readily (if all) rebuilt by metagenomic sequencing. Finally, in vitro trials with model microbiota, which can only be composed of bacterial strains recovered in the laboratory, would greatly improve investigations of gut and oral microbial ecology.
For these reasons, several strategies for increasing the quantity of culturable bacteria from the HGM have been developed during the last few decades[79, 86–104]. Culture-based procedures have enabled the enrichment of various portions of the microbial distribution through a wide range of culturing conditions, including media for the selective growth of bacteria. These approaches expanded the list of cultured bacteria and enabled the isolation of species with low abundance that would have gone unnoticed in sequencing-based methods [96, 98–103]. Implementing various culturing conditions on agar plates, on the other hand, is limited by i) significant labor effort, ii) massive reagent and consumable consumption, iii) limited throughput, and iv) fast-growing species potentially outnumbering slow-growing ones.
In recent times, the swift evolution of microfluidic techniques has opened

up novel avenues for utilization within the area of microbiology[105]. This progress has a wide range of applications, including examples in culturing-related methodologies, thanks to features such as lowering reagent use, enhancing automation and generating unique culture conditions for bacteria within droplets.

The process of encapsulating bacteria within micro-droplets offers the simultaneous and compact cultivation of numerous clonal cultures. This approach leads to reduced reagent consumption, higher throughput, and the establishment of a microenvironment potentially suitable to fostering bacteria for laboratory cultivation.

Notably, isolating bacterial cells within culture vessels with a size comparable with bacterial cell dimensions may offer benefits in terms of reviving cells from a live but non-culturable condition[106, 107]. Previous research has proven the effectiveness of droplet-based culture methods in gaining access to previously inaccessible species in laboratory settings[87, 94, 104]. Furthermore, the isolate collections have been enhanced by combining encapsulation with other types of culture media[92] or by additional manipulation of the droplets[86, 91, 94, 95].

In Chapter 3 we discuss our method for culturing bacterial species from the human gut and oral microbiota, with high-throughput single-cell encapsulation of bacteria in droplets.

1.3.3 Microfluidics for Porous Materials

Material science is one research area where microfluidic techniques demonstrated their value promoting notable steps forward. Within this field, these techniques have facilitated significant advancements, especially in the creation of porous materials. These materials find applications in various areas, such as catalysis in porous media, fluid filtration, heat storage, energy adsorption, and tissue engineering..

Recent papers [108–110] employed microfluidics to finely control the porosity of materials with a superior precision in pore size, shape and distribution, creating complex structures that are challenging to achieve using standard methods. Moreover, thanks to microfluidics, they improved scalability, reproducibility and uniformity of the porous structures.
In these examples, microfluidics allowed to generate porous materials with controlled properties. For instance, controlling the size and monodisperisity of droplets or bubbles in emulsions or foams, allowed to control the porosity of the final structures. In the case of emulsions, it is possible to solidify the continuous phase, for example through polymerization, and later remove the dispersed phase and obtain a solid porous structure (Figure 1.11).
The immediate approach to generate droplets is using a flow focusing device and tune the porous size by supplying time-varying flow rates of the continuous and dispersed phases.
Other articles reported the use of a valve-based flow-focusing (vFF) chip, allowing to control the droplet size thanks to flexible channel walls that could deform the orifice of the cross junction at the center of the chip[111, 112]. Adopting the flow focusing approach enabled to achieve robust and easy droplet generation, and in the valve-based case, the variation of droplet size could be controlled through an external pressure source. However, owing to the difficulty of parallelization, this geometry is not ideal for upscaling, hence additional refinement is necessary to make these designs viable for manufacturing.
Other methods based on step emulsification have demonstrated improved production rates in comparison to the conventional flow-focusing technique [55]. Additionally, the adoption of step emulsification has enabled the manipulation of reagent concentrations and provided greater precision in governing localized material properties. However, it's important to note that these approaches still face a constraint: step emulsification is restricted in its ability to produce only a single droplet size throughout

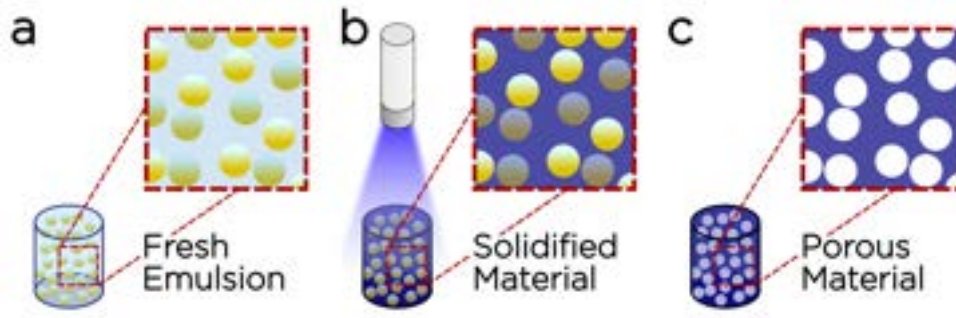

Figure 1.11: Scheme of three steps for the generation of functional porous materials: (**a**) Deposition of Oil-in-Water emulsion, (**b**) Polymerization of the external phase uder UV light, and (**c**) Removal of the internal phase to obtain the porous structures.

the generation process.

The important results that have been achieved so far could have even more promise if they were used on a bigger scale. In a larger sense, these results point to a hopeful way to improve, especially by speeding up the development of porous structures with more precise details.

To address these challenges, we developed a novel microfluidic technology based on a tunable step for the parallelised droplet generation with a dynamic range of volumes (in Chapter 4), and applied this technology for the 3D printing of porous materials (in chapter 5).

2

Novel Method to Measure Uptake Time in Cancer Cells

Contents

2.1 Introduction

As highlighted in subsection 1.3.1, the development of novel methods for drug design and delivery hinges on a thorough understanding of the complex dynamics driving cell-tissue penetration and drug-cell interactions. The drug uptake time is a critical yet understudied factor, since prior research has primarily assessed it merely minutes after the drug arrives at the cell membrane [113, 114]. Improving the temporal precision of such measures is a daunting task that requires precise control over the local cellular environment. Furthermore, it is critical to synchronize the cell exposure to drugs with the signal acquisition from a high-sensitivity detector with a high temporal resolution.
In this project, we introduced an innovative method for measuring uptake time on a hundreds-of-microsecond timescale. This approach combines the capabilities of microfluidics with time-correlated single-photon counting (TCSPC). TCSPC enables us to detect small changes in drug concentration both inside and outside cells, achieving a resolution below a millisecond. To ensure precise control and swift adjustments of the drug concentration surrounding the cells, we designed a microfluidic device equipped with on-chip microvalves (subsection 1.2.6).
We designed a two-layer PDMS device to recreate the on-chip micro-valve technology[56, 115], in the top-down configuration, i.e. with the flow layer on the bottom (thin layer) and the control layer on the top (thick layer). The fabrication of devices with this layout is more complex than in the bottom-up configuration, due to four reasons mentioned in section 1.2.6: i) it requires to fabricate round section channels to fully close the valve, ii) it requires higher pressures to close the valve, iii) the height of the channels in the flow layer (thin layer) is limited, and iv) the pressurised air acts on the bond between the two PDMS layers that is generally weaker than the PDMS-glass bonding. Nevertheless this study required to position the cancerous cells in contact with the glass slide, to make

the chip viable for the time correlated single photon counting (TCSPC) in the confocal microscope.
Since every module for cell incubation is only viable for a single-use, and the repetition of biological experiments required more than 100 modules, we optimised our method for the large-scale production of robust and reproducible chips using the stamp-and-stick approach [61].
This project demanded not only the development, testing, and optimization of procedures for measuring cellular uptake time (subsection 2.2.3) but also necessitated the creation of a custom experimental setup (subsection 2.2.4). To achieve synchronization of the signal with the opening of the valve, an innovative approach involved the incorporation of an LED within the system, that was introduced to generate a square signal just before opening the valve, ensuring precise timing coordination. Additionally, custom software programming was a crucial component (subsection 2.2.5).

Contribution of the Author This project is the fruit of cooperation with other scientists from the Institute of Physical Chemistry, PAS (Marta Pilz, Karina Kwapiszewska, Ladislav Derzsi, Karol Makuch, Piotr Garstecki and Robert Hołyst). My participation within this project included designing and preparing the microfluidic chips, defining custom procedures for the chip realization, preparing the setup for the automated flow control, and writing the software. I contributed in creating visual representations for the patent (used also for the conferences or future papers), and defining, validating and describing our novel method.

2.2 Materials and Methods

2.2.1 Scheme of the Chip

We designed a microfluidic chip for the incubation of cancerous cells and the controlled injection of anticancer drugs (scheme in Figure 2.1). The chip consisted in a two-layer PDMS device bonded on a glass slide, with one thick layer on the top (*control layer*) and one thin layer (*flow layer*) between the glass and the control layer.
The flow layer consisted of one central chamber in which we incubated the cells (length 5000 μm, width 500 μm and height 50 μm) and four serpentine channels. One serpentine channel connected the cell incubation chamber to one outlet of the chip, while the other three channels were used to inject reagents or as secondary outlets and were connected on the second side of the culture chamber through a round-section channel (length 1600 μm, width 120 μm, height 20 μm) that served as valve of the chip. The round channel was aligned with a square chamber in the control layer of the chip, enabling to apply pressure on the round channel and deform it. The round-section channel was used to manage the stream of drugs inside the cell culture chamber.

2.2.2 Fabrication of the Microfluidic Device

Preparation of the masters The production of two-layer PDMS devices required two distinct masters for the two layers, designed through Computer Aided Design (CAD, Autodesk Autocad). We prepared them with different strategies to address the requirements of each layer.
Thick layer: the master was created with standard photolithography[6], aiming for $\sim$ 50 μm features. We coated a 3" silicon wafer with SU-8 2050 photoresist (MicroChem Corp, USA) and performed the spin-coating at 3000 rpm for 30 seconds. Then we placed the master on a hot plate to

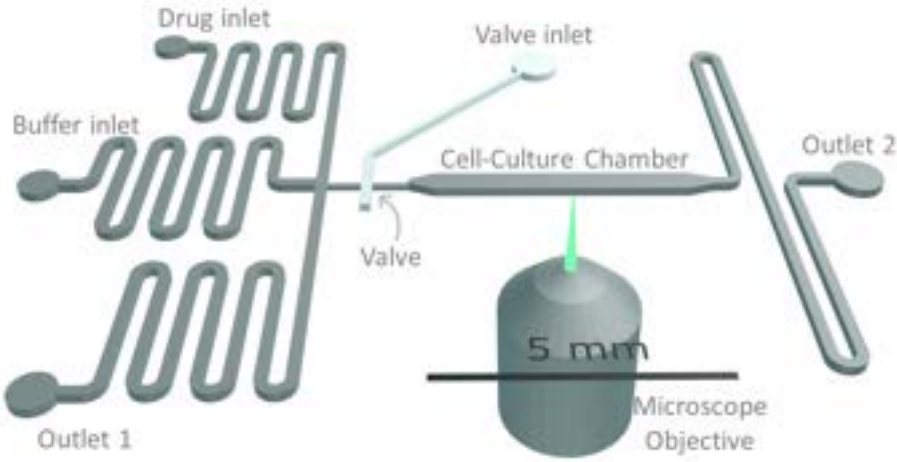

Figure 2.1: Scheme of the chip. On the left, two inlet channels (one for drug ad one for buffer) and one outlet channel connected to the reservoir for waste collection. A thin round channel connects the inlets to the cell-culture chamber. The channel can be deformed, acting as a microvalve. At the right of the cell culture chamber, one outlet.

soft-bake it at 65 °C for 2 minutes and then at 95 °C for 7 minutes. Then, we exposed the wafer to UV light (150 mJ/cm^2) through a high-precision photolithography mask. We performed the postexposure baking of the wafer on a hot plate at 65 °C for 2 minutes and at 95 °C for 6 minutes. Finally, we dipped the wafer in SU-8 developer (MicroChem Corp, USA) for 6 minutes, to remove the unexposed resist before rinsing the chip with isopropanol to wash away the developer. We peformed the hard baking at 195 °C for 5 minutes, and then silanised the master to avoid sticking of the PDMS on the features: we placed the wafer in a desiccator with a tube containing 60 μl of liquid silane (Trichloro(1H,1H,2H,2H-perfluorooctyl)silane, Sigma-Aldrich, USA) and activated the pump for 1 hour at 15 mbar.

Thin layer: We used a CNC milling machine (MFG 4025P, Ergwind, Poland) to mill microchannels in a round polycarbonate plate with 5 mm

thickness and a diameter of 7 cm (step 1 on Figure 2.2). We were able to generate round and square section channels simply by adjusting the drill on the CNC machine, instead of using two-layer photolithography that would have required both positive and negative photoresists for such features.

The next step is to create a positive mould to spin-coat and produce the thin layer of the chip. To make a round replica of the polycarbonate plate, we fabricated a custom teflon rim where we could accommodate the plate (step 2 on Figure 2.2). We designed the rim to have an inner diameter of 70 mm (same width of the polycarbonate plate), and with a step at 8 mm height, where the inner diameter increased to 78 mm. We poured uncured PDMS on the polycarbonate layer (step 3 on Figure 2.2), and covered it with a silicon wafer (step 4 on Figure 2.2), creating a 3 mm thick PDMS layer between the plate and the wafer. After baking the master for two hours at 75 °C (step 5 on Figure 2.2), we carefully removed the polycarbonate plate from the rim, and then the silicon wafer together with the PDMS (step 6 on Figure 2.2). The wafer was not detached from the PDMS, in order to support the material during the spin-coating.

Finally, we silanised the mould by placing it for 1 hour at 15 mbar in a desiccator with 60 μl of liquid silane (Trichloro (1H,1H,2H,2H-perfluorooctyl) silane, Sigma-Aldrich, USA).

Preparation of two-layer PDMS chips We produced the two layers of the chip separately, then combined them and bonded the PDMS to a glass slide to obtain the final device.

We produced the *thick layer* by pouring fresh PDMS (10:1 ratio between PDMS and curing agent) on top of the silicon wafer, and baking it for two hours at 75 °C. We pulled the cured PDMS off the wafer and used a 1 mm biopsy puncher to form the valve inlet, and a scalpel to remove the undesired PDMS from the sidewalls of the chip.

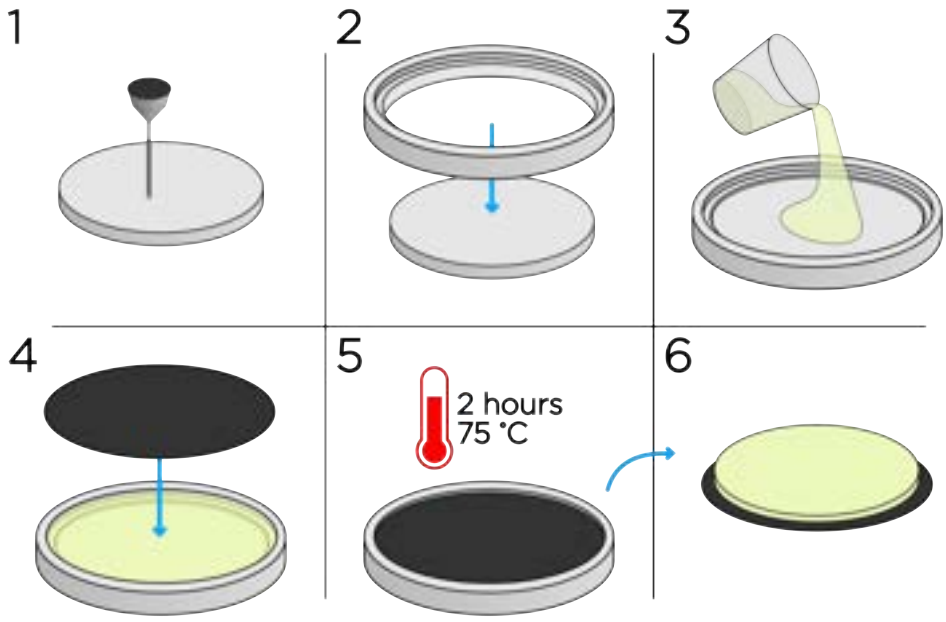

Figure 2.2: Scheme of the preparation of master for the thin layer. 1) Milling of microchannels in the polycarbonate plate, including channels with round and square section. 2) Inserting the polycarbonate plate in a PTFE holder to recreate the bath for the positive replica of the features. 3) Coating the master with PDMS carefully removing the bubbles from the channels. 4) deposing a silicone master on the uncured PDMS to seal the chamber. 5) Baking the chip for 2 hours at 75 °C. 6) Removing the PDMS and the silicone wafer from the chamber to obtain the final master.

To produce the thin layer, we poured 5 ml of PDMS mixture over the PDMS replica of the chip, and performed the spin-coating at 1500 rpm for 30 s. We chose a 20:1 elastomer-to-curing-agent ratio for this layer to guarantee a more elastic PDMS and decrease the pressure required to properly seal the valve. The PDMS layer was baked for two hours at 75 °C.

For the bonding of the two PDMS layers, we prepared a silicon wafer with a thin coating of curing agent, obtained by pouring a few drops of curing agent, and spinning the wafer for 45 seconds at 5500 rpm. The

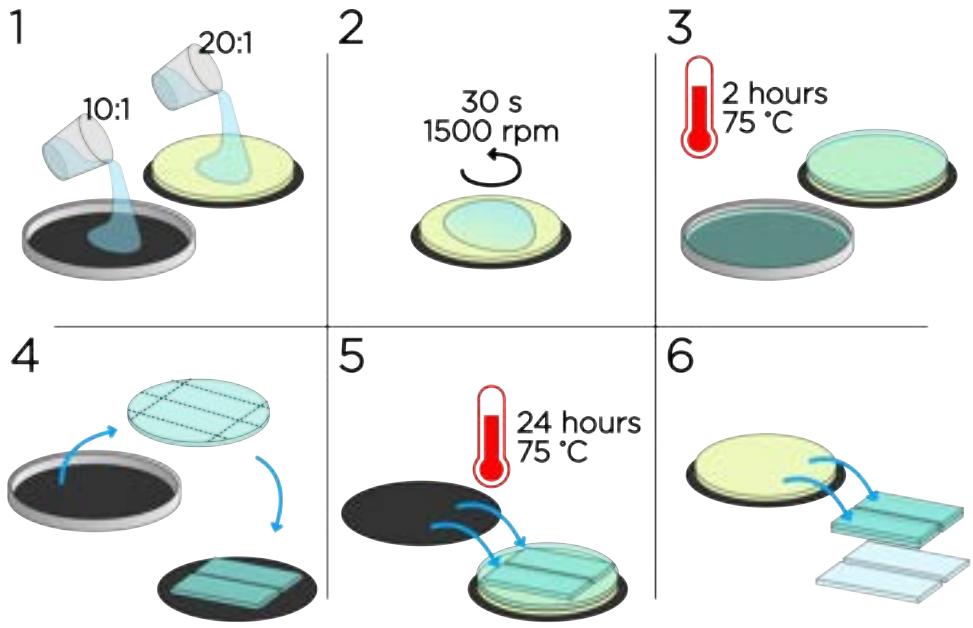

Figure 2.3: Scheme of the chip preparation. 1) Pouring PDMS on the masters for the thick and thin layer. 2) Spin-coating the thin layer master at 1500 rpm for 30 s to obtain a 100 μm PDMS layer. 3) Baking the two layers for two hours at 75 °C. 4) Removing the the thick PDMS layer from the master, cutting the chip outlines and stamping them on a surface coated with a few drops of curing agent. 5) Aligning the thick layers on the thin layer and bake for 24 hours. 6) Bonding the PDMS on a thin glass slide with oxygen plasma.

thick PDMS layer was stamped onto the wafer to wet its surface with curing agent [61]. We positioned a customized frame on the thin layer, following alignment markers, and then introduced the thick layer within the frame. The frame allowed to perform a precise alignment of the two layers without using microscopes or mask aligners. We baked the completed PDMS layers for 24 hours at 75 °C before removing them from the wafer, punching the chip inlets using a biopsy puncher, and proceeding with the conventional plasma-bonding of the microfluidic chip.
After sterilizing the microfluidic devices under UV light for 30 minutes, they were ready for use in cell research.

2.2.3 Experimental Procedures

Our method is summarised in four main steps, represented in figure 2.4. Each step includes precautions that are essential for the success of the experiments, so we will discuss them separately.

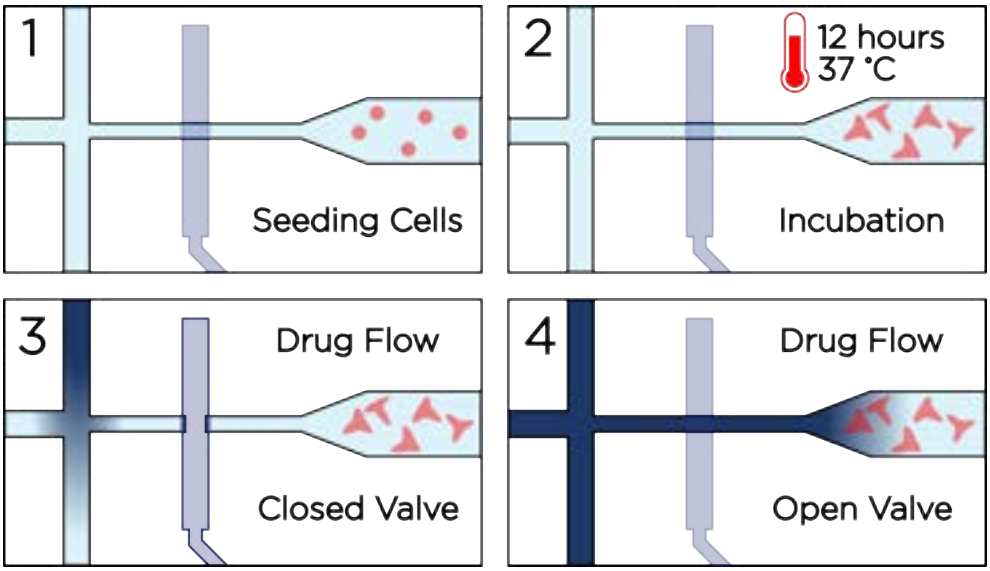

Figure 2.4: Scheme of the method for the measure of drug uptake. 1) We introduce the cells in the chamber for culture. 2) We incubate the cells overnight at 37 °C. 3) We position the chip on the confocal microscope and connect all the inlets. We apply pressure on the thin membrane and the microvalve is closed. We flush the drugs to obtain the required concentration on the left side of the chip. 4) We trigger the release of pressure and the drugs flow inside the chamber.

Seeding the cells within the chip To increase cell adhesion, we coated the glass substrate of the microfluidic device with fibronectin (Sigma-Aldrich, Germany) before seeding the cells, filling all the channels with a fibronectin solution with a concentration of 50 g/ml. Then we

incubated the microfluidic device at room temperature for 45 minutes. Then, we flushed pure medium within the channels of the chip to remove the fibronectin solution, and proceeded to seed the cells. We introduced the cell suspension within the chip at a flow rate of 1 ml/min, while monitoring the chip with a microscope (Nikon Eclipse Ti-S inverted) (Figure 2.4, 1). When a proper concentration of cells is observed within the cell culture chamber, we removed the tubing connected to the syringe, and sealed all the inlets of the chip with tubing filled with culture medium, to avoid the evaporation of the medium during the overnight incubation. During this and the following processes, it is necessary to avoid air bubbles within the chip, since they could detach the cells from the glass wall or destroy them.

Incubation of the cells We placed the chip in a Petri dish filled with a PBS buffer to half the height of the chip to avoid the evaporation of the medium from the chip's channels, and incubated the chip overnight at 37 °C in 5% CO2 (Figure 2.4, 2). During this process, the trapped cells adhere to the glass surface.

Preparing for the measures We position the chip on the single molecule detection system and we plug the tubing connected with pressurised air to the control layer. We verify that the valve is correctly closed, and then we connect the other inlets to the two syringes containing fluorescent drugs and PBS buffer (Figure 2.4, 3). We connect the outlets of the chip to to two containers for collection of waste reagents. We introduce the fluorescent drugs within the chip, reaching the proper drug concentration on one side of the valve, making sure that there is no leakage of fluorescent particles within the chamber. Finally, we focus the detection volume within one cancerous cell, recording the fluorescence

signal.

Measuring the uptake time of anticancer drugs in cancerous cells While recording the fluorescence signal inside the cell, we trigger the experiment from the custom made LabView program. Through a series of electric signals delivered to the FPGA, all the following steps are executed automatically. i) The LED emits a signal with the same wavelengths of the expected fluorescence, and therefore visible in the data acquisition as a square function. The LED is active for one second, then it turns off, and simultaneously the three-way valve switches, releasing the pressure on the on-chip microvalve, and the solenoid valve downstream the outlet of the chip closes. During this step, the drug flow is deflected directly inside the chamber (Figure 2.4, 3). The fluorescent signal is measured within the cell for 15 minutes.

Once the fluorescent drugs enter the chamber, the chip is contaminated, since they cannot be completely removed from the cells and from the walls. Nevertheless, the chip could still be used to measure two additional processes: drug removal from the cell, and the increase of the fluorescent signal in proximity the cells.

Drug removal: we closed the on-chip microvalve and stopped the flow of drugs within the chip. Instead, we flushed cell buffer for 5 minutes, washing away the drugs from one side of the chip. We started recording the fluorescence signal within the cell, and triggered the same measure as before.

Reference measurement in proximity of the cell: We moved the objective in the proximity of the cell and closed the valve. We prepared the chip for a second injection of drugs within the chamber, to obtain a signal that could be compared with the first signal measured within the cell.

2.2.4 Setup for the Automated Control of Drug Injection

The scheme of the custom setup for the control of reagents inside the chip is represented in figure 2.5.

We prepared two glass syringes (Hamilton gastight, USA) of 2.5 ml each, one containing the fluorescent drugs solution, and the other containing the phosphate-buffered saline solution (PBS solution, Sigma-Aldrich, USA) used as a buffer for the cells. The syringes were installed on two syringe pumps (Cetoni, Germany) and linked to the inlets of the chip through thin teflon tubing (ID/OD = 0.4/0.9 mm, Bola, Germany). The syringe pumps were computer controlled.

The flow of injected chemicals through the cell culture chamber is controlled by an on-chip pneumatic valve. The valve state (open or closed) is controlled by a three-way electromagnetic valve which controls the external airflow, and can be switched between room pressure and a pressure controller. One outlet of the chip is connected downstream to another electromagnetic valve.

Both electromagnetic valves are controlled by a Field Programmable Gate Array (FPGA, NI PCI-6703, National Instruments) linked to a computer and controlled by custom software written in LabView.

A Light Emitting Diode (L-7113SEC-J3, Kingbright electronic, Taiwan) is also linked to and controlled by the FPGA, allowing it to create light signals that can be detected from the measurement system and utilized as synchronizing signals.

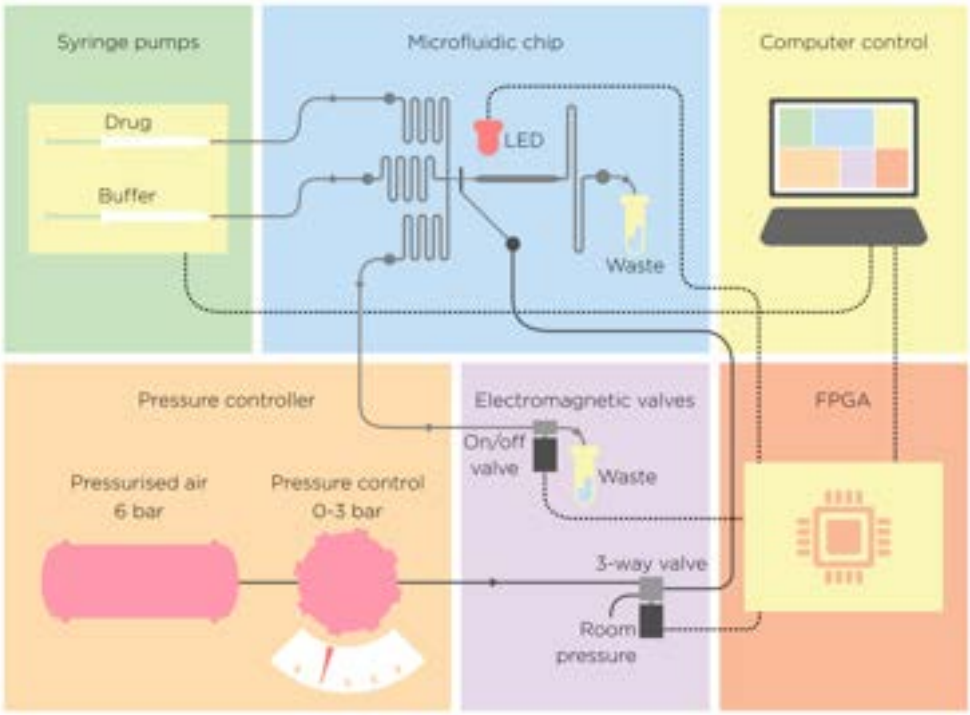

Figure 2.5: Scheme of the setup for the automated drug injection. Two syringes containing either drug or buffer solutions are connected to the inlets of the microfluidic chip. A computer controls two syringe pumps and the signals from an FPGA. The FPGA signals activate two electromagnetic valves. One valve (on/off valve) regulates the flow through the first outlet of the chip, while the second valve (three-way valve) is connected to the control layer of the chip and allows to switch between room pressure and the pressurised air regulated with a pressure controller.

2.2.5 Software for the Automated Execution of Experiments

In Figure 2.6, we present the user interface of our custom program designed for managing flow control and LED light emission during experiments. This program provides control over four microvalves and an LED within the experimental setup. The left panel features four indicators displaying the real-time status of the valves (open/close) and the LED (on/off). In the central panel, we included the manual controls of each valve and the LED, while the panel on the right enables the configuration of specific parameters for automated experiment execution. These parameters include: i) the time delay between initiating a command and execution, ii) the duration of LED activation (typically one second), and iii) the interval between the opening and closing of valves (typically 15 minutes). Additionally, two buttons are provided for executing experiments, with the choice between using either the dye or the medium.

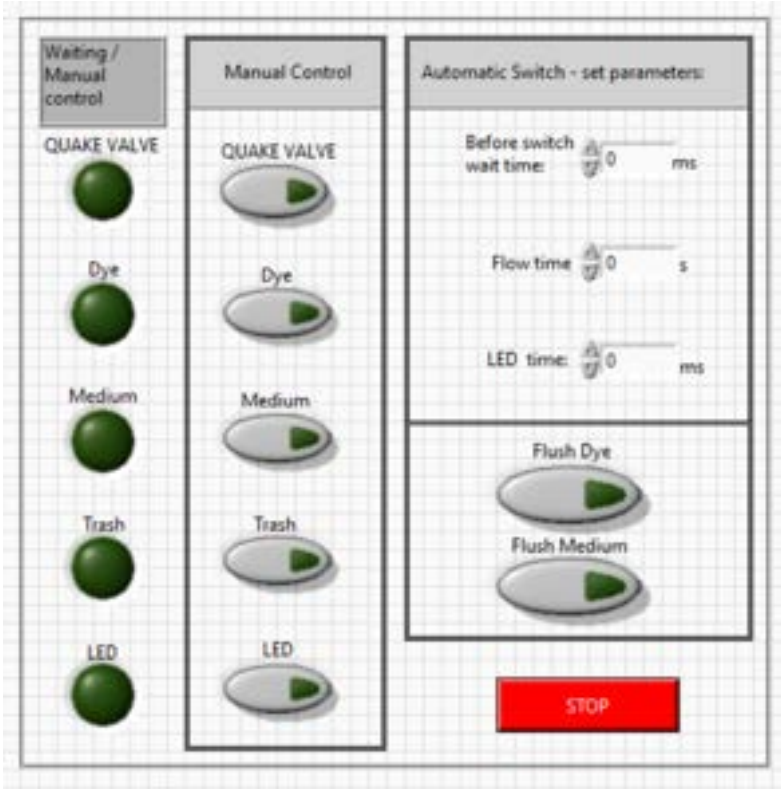

Figure 2.6: Picture of the user interface of the valve control program. The software includes the manual control of four different electromagnetic valves and one led. Moreover, the switch of flow in the chip can be triggered with an automated routine. When we trigger the switch, the LED emits light to give an optical feedback in the acquisition. When the light turns off, the pressure on the microvalve is released and the drug flows in the chamber. The program includes controls to trigger the buffer flow inside the chamber.

2.3 Results

As requested by other co-authors, I do not include the measures of uptake time of anticancer drugs in cancerous cells in my thesis. These results should be visible as soon as the paper will be published, either as a pre-print or in a peer-reviewed journal.

In this project we designed and tested a microfluidic chip based on two layers of PDMS bonded on top of a glass slide.
The bottom layer consisted of a thin PDMS layer (thickness ~ 100 μm) including the cell-culture chamber connected to three channels through a shallow round-section channel (height ~ 20 μm).
The top layer had a thickness of $\sim$5 mm and included a square-section channel aligned on top of the round-section channel to recreate the on-chip microvalve in the push-down configuration.
Our method included several steps from the preparation of the experiment to the execution. First, the cell suspension is introduced in the culture-chamber by a syringe pump, and incubated overnight at 37 °C to let the cells attach to the glass surface.
Then, the chip is connected to the custom made setup and the pressure on the valve layer is increased until the valve is fully closed, generally with a pressures $\sim$ 1300 mbar.
The fluorescent drugs enter from the first inlet (one example in Figure 2.7 a), while the microvalve is closed and flushed for a few minutes until we ensure the right drug concentration outside the cell-culture chamber (Figure 2.7 b).
When we trigger the drug injection, the LED positioned on top of the chip provides a light signal for 1 second (optical feedback for the detection), and immediately after that, the valve controlling the first outlet is closed, the pressure of the microvalve is released, and the drug stream is deflected inside the chamber (Figure 2.7 c). During the whole process, we record the

fluorescence signal with a single-photon avalanche diode (timing resolution <50 ps). After the measurement, we repeat the same procedure, flushing buffer solution from the second inlet (instead of drug solution), and we measure the decrease of the fluorescence intensity to study the drug removal time.

Figure 2.7: Preliminary measures introducing a red ink within a previous chip design. (**a**) Flushing the red solution through the side channels with the closed valve, (**b**) preparing for the experiment, and (**c**) opening the valve and flushing the die within te chamber.

We repeated the experiments measuring the fluorescence signal inside and outside the cell.
We quantified the time between the end of the LED signal and the start of the fluorescence signal to be $\sim$ 80 ms. This time includes the valve-opening time and the time for the drug to reach the cell. After that, we estimated a time of $\sim$ 4 ms ms to reach the proper drug concentration outside the cell.
The preliminary measures allowed to identify the characteristic time for drug uptake $\sim$ 760 ms and removal $\sim$ 15 s.

2.4 Conclusions

In this project, we developed a practical microfluidic device designed for precise drug delivery in close proximity to targeted cells.
By integrating this device with a custom experimental setup, coupled with Time-Correlated Single Photon Counting (TCSPC), we successfully recorded, for the first time, the period of cellular uptake of anticancer drugs in cancerous cells with sub-millisecond resolution. This comprehensive project encompassed the creation of a custom experimental setup, the development of software for automated experiment control, the synchronization of light signals with valve openings, and the establishment of protocols to ensure high repeatability in chip fabrication and experimental procedures.
Our innovative approach significantly expands the possibilities for investigating the cellular uptake of fluorescent molecules, offering valuable insights for non-clinical research aimed at the development of novel drugs and drug delivery nanocarriers.

3

High-throughput Culturomics of Gut Microbiota

Contents

3.1 Introduction

In section 1.3.2 we discussed the limitations in culturing species from the human microbiota, and the benefits from microfluidic-based approaches. While there have been instances of effective droplet-based culturing methods, the fusion of microfluidic technology with the stringent anaerobic conditions prevalent in the gut microbiota setting remains relatively uncommon. The intricate task of incorporating microfluidic devices within anaerobic environments has led to only few examples of this technology[95, 116, 117]. Notably, ensuring strict anaerobic conditions for droplet-based culturing throughout a comprehensive workflow, spanning from sample extraction to the isolation of bacterial strains for laboratory cultivation, has yet to be achieved.

In this project, in cooperation with Biomillenia SAS, we have developed a comprehensive and integrated microfluidic workflow optimized for high-throughput culturomics encompassing the isolation, cultivation, and taxonomic identification of bacteria sourced from both gut and oral microbiomes. Our methodology strictly adheres to anaerobic conditions throughout the entire process, from sample collection to the intricate microfluidic handling and the creation of cell banks. The end result is a substantial collection of bacterial cells consisting of clonal isolates that have been taxonomically classified.
The initial phase of bacterial isolation involves the creation of water-in-oil droplet libraries, that we achieved using a custom microfluidic chip. We consider this step pivotal since it maintains different bacterial species separated during culturing, preserving the diversity of the sample. The combination with microfluidics allowed to maintain such a diversity while offering high-throughput capabilities.

To enrich a wider spectrum of bacterial population memebers, we employed four distinct culture media.
As a result, our bacterial strain collection encompasses over 199 species, including both rare and previously uncultured representatives. Additionally, we've successfully cultured members from the "most-wanted" list highlighted in the Human Microbiome Project[118].

Contribution of the author This project is the fruit of cooperation with my supervisor Piotr Garstecki and scientists from Biomillenia SAS (Alex Dajkovic, Unai Escribano-Vazquez, Andrei Kiselev, and Dirk Loeffert). My participation within this project included designing and preparing the microfluidic chips, as well as integrating the microfluidics device within the workflow patented from the researchers of Biomillenia. Repeating the workflow for the great amount of samples, required the joint effort of me and other co-authors. I personally contributed in performing each step of the workflow, except for the sequencing of the nucleotide sequences and the taxonomy assignment (more information in subsection 3.2.1). Finally, I performed the data analysis and prepared the visual representations included within this thesis.

3.2 Materials and Methods

3.2.1 Workflow for Generation of Cell Banks

We can summarize the workflow to culture, isolate and identify bacterial species from the human gut microbiota in five phases (schematized in Figure 3.1): 1) Fecal and oral samples are collected from healthy donors and rapidly preserved in anaerobic conditions. 2) The samples are processed through a series of filtering steps to extract the bacterial population while excluding human cells or undigested food, and then diluted in a suitable growing medium. 3) A microfluidic chip is used to encapsulate bacteria in monodisperse droplets from the bacterial suspension. 4) After culture, the droplet libraries are distributed on microtiter plates and cultivated again.The growing colonies are selected, inoculated, and grown in microtiter plates which serve as the final cell banks. We withdrew aliquots from each well of the cell banks and inoculated them in two more microtiter plates, preserving the positional order. This allowed for three copies of each cell bank: the original, a backup, and one for species identification. 5) We performed Polymerase Chain Reaction (PCR) to amplify the V4 region of the 16S rRNA gene of the colonies using a distinct set of primers for each well, and then identified the species in each well through sequencing.
Each step is discussed more in details below.

Sample collection We collected 18 fecal and 13 oral samples from 18 healthy volunteers in Biomillenia facilities (Biomillenia SAS, 102 Avenue Gaston Roussel, 93230 Romainville, France). Before participating in the study, all the volunteers expressed written consent to participate in the study, and received the following instructions to deliver the samples autonomously. *Fecal samples*: each donor deposed the fresh fecal sample in a plastic tube, and placed it in a box with an anaerobic pouch to

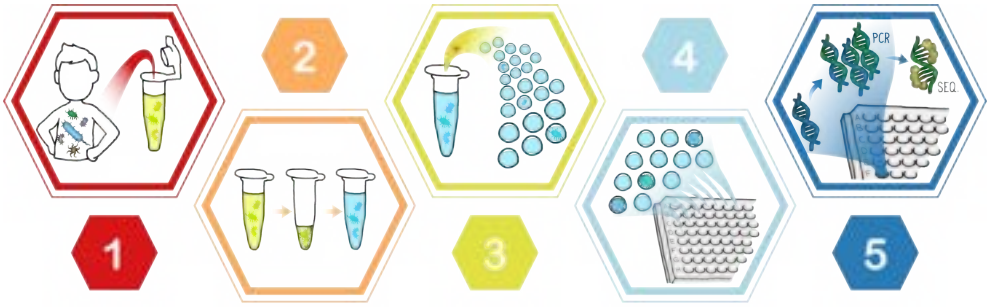

Figure 3.1: Scheme of the workflow for bacteria isolation, representing five steps. 1) Collection of fecal and oral samples. 2) Extraction of bacterial cells from the samples and resuspension in the selected medium. 3) Encapsulation and incubation of single bacterial cells in droplets. 4) Droplet deposition in microtiter plates. 5) PCR in wells and Illumina sequencing of the PCR products, with identification of the isolated species.

maintain the anaerobic conditions for the short time (less than 5 minutes) necessary to introduce the box within the anaerobic chamber of the lab. *Oral samples*: each donor received 20 ml of fresh sterile water to rinse the oral cavity twice, and collected the water into a 50mL Falcon tube that we introduced inside the anaerobic chamber in less than 5 minutes from the collection.

Maintaining anaerobic conditions Within 5 minutes from the collection, we put the samples within the Coy vinyl anaerobic chamber to ensure anaerobic conditions and preserve sample diversity. The chamber was filled with a gas mixture (nitrogen 90%, carbon dioxide 5%, hydrogen 5%) and a catalyst (Stak-Pak from Coy Lab Products) to eliminate any traces of oxygen that may have entered. The oxygen content was monitored with an oxygen sensor (Coy Lab Products Anaerobic Monitor CAM-12) that measured the oxygen content in the particle-per-million range. The chamber included all the instruments for the manual and

microfluidic processing of the samples, as well as a microscope with a camera connected to an external computer and pressure pumps powered with the same gas mixture of the chamber.

Extraction of bacterial cells from the fecal samples Within the anaerobic chamber, we processed the fecal samples through a series of filtering steps to separate the bacterial cells from unwanted elements such as undigested food. We placed a few grams of stool sample in a filtering bag (Nasco WHIRL-PAK 710 mL), where we added a cryopreservation solution (MD diluent, [119]) in a 1:4 w/t ratio, and manually homogenized sample and diluent within the bag. We collected the homogenate through the filtering bag into a 50 ml falcon, and proceeded to filter it through a sequence of cell strainers of decreasing size (100, 60 and 40 μm) followed by a 20 μm Steriflip (Millipore).
We aliquoted the resulting bacterial suspension pipetting 50 μl in separate glass vials that we stored at -80 °C.

Estimation of the bacterial concentration in the suspensions We diluted 10 μl of bacterial extract in 90 μl of PBS solution to obtain a 1:10 dilution, and consequently through 11 more dilutions maintaining the 1:10 ratio, for a total of 12 dilutions. During each step of the process, we discarded and replaced the pipette tips. From each dilution, we placed two aliquots of 4 μl each on the surface of an agar plate containing Gifu Anaerobic Medium (GAM) and agar. We let the deposited dilutions dry in the anaerobic tent, and then we incubated the samples for three days in anaerobic conditions at 37 °C. We counted the number of colonies ($N_{colonies}$) from the droplets of the highest yielding dilution ($D_{highest}$) and estimated the concentration of CFU/ml using the equation

$$\text{Concentration} = \frac{N_{colonies} 10^{D_{highest}}}{drop\ volume} = \frac{N_{colonies} 10^{D_{highest}}}{8 \text{ ml}} \qquad (3.1)$$

Preparing the culture media To cultivate the bacteria from fecal and oral extracts in droplets, four different growth conditions were used: Gifu Anaerobic Medium (G condition; HyServe, 5433), G medium + 7.5 mg/L vancomycin and 100 mg/L kanamycin (N condition, to enrich for Gram-negative bacteria), G medium + 10 mg/L colistin and 5mg/L nalidixic acid (P condition, to enrich for Gram-positive species), and E condition, to enrich for spore formers, as described from *Browne et al.*[100]. The E condition included a 4-hour pre-treatment of the sample with an ethanol in water (70% w/t) solution in a 1:1 ratio between sample and solution, followed by culture in G medium. We diluted the fecal and oral extracts in each of the above-mentioned growth media to achieve a final bacterial concentration of 3 x 106 CFU/mL. The reagents for droplet generation (media and oil) were introduced into the anaerobic chamber one month before the experiment to ensure full gas exchange in the fluorinated oil (NOVEC 7500, 3M, USA) used to create microfluidic droplets and the culture media. Antibiotic supplies for selective growth were aliquoted and kept at $-80\,^{\circ}\mathrm{C}$ to maintain long-term stability, and introduced to the anaerobic chamber shortly before the start of the experiment.

Single-cell encapsulation of bacteria in droplets To encapsulate single bacterial cells in microdroplets, we relied on a non-deterministic technique[120] based on Poisson probability distribution (equation 3.2). Assuming that the cells are sparsely distributed in the suspension, it is possible to calculate the probability distribution $p(k, \lambda)$ of having k cells in a droplet, with λ the average number of cells per droplet volume: the probability distribution follows the equation

$$p(k, \lambda) = \frac{\lambda^k e^{-\lambda}}{k!} \tag{3.2}$$

By setting $\lambda \sim 0.1$ CFU/droplet, only 0.47% of droplets will contain more than one cell. We controlled the droplet volume ~ 35 pl and the

concentration of cells in the suspension $\sim 3 \cdot 10^6$ CFU/ml to reach a similar concentration of CFU/droplet .

Droplet generation in the microfluidic millipede device In a handmade microfluidic device described below, we created 33 pl droplets of bacterial suspension in fluorinated oil (NOVEC 7500, 3M, USA) with 2.5% surfactant (008-FluoroSurfactant, RAN, USA). We collected the emulsion in a 1.5 ml reservoir (Eppendorf) sealed with a Polydimethylsiloxane (PDMS) cap and containing one inlet and one outlet tubing.
The first step of droplet generation is to store the bacterial suspension and the fluorinated oil in two separate tubes (2 ml, Eppendorf) that are individually sealed with pressurised caps (P-caps, Fluigent). The structure of the P-caps allowed us to regulate the pressure inside the two tubes with pressure controllers (Fluigent). When we apply pressure, generally 600 mbar for the oil and 400 mbar for the aqueous phase, the reagents flow through thin tubing and directly into the microfluidic chips (outer diameter 0.75 mm) where the emulsion is produced.
The emulsion is collected in a 1.5 ml tube and incubated for three days at 37 °C under anaerobic conditions. The pressure source is provided with the same gas mixture used to fill the anaerobic chamber, and the reagents are stored within the chamber as previously described.
To assure sterile conditions inside the microfluidic chips, we conducted chip bonding and surface modification in a sterile environment, and we immediately sealed the modules for droplet formation separately using adhesive tape. When creating droplets, the tape is taken from each module individually, and each module is for a single-use, i.e. for a single condition of medium, donor, and sample. The sterility of the setup was confirmed by making and cultivating droplets with media alone, without the bacterial extract, and microbiologically and by sequencing the lack of bacterial growth.

Creation of the cell banks First, we quantified the number of droplets containing bacterial colonies per milliliter (mL) of microfluidic emulsion with the following procedure. We withdrew a small amount of emulsion (a few microliters) from the tube, and placed it on glass slides. We observed the droplets under a microscope, estimating the ratio between positive droplets $N_{positive}$ and total number of observed droplets N_{total}. The, we calculated the concentration of positive droplets in each ml of emulsion, following the equation

$$\text{Concentration} = \frac{N_{positive}}{N_{total} \times V_{droplet}[\text{ml}]} \tag{3.3}$$

Where $V_{droplet}$ is the droplet volume expressed in ml.
We diluted the emulsion to obtain a concentration of one positive droplet every 10 wells in the microtiter plates (meaning 0.1 droplets/90 μl). with this approach, we utilized once again the Poisson distribution to ensure that the bacterial colonies were well-separated in the plates.
We prepared enough dilution to dispense 90 μl in each well of 12 microtiter plates with 96 wells each.
We cultured the colonies for three days and then we hand-picked the growing strains and inoculated them in a new 96-well plates containing fresh growth medium. By selecting only the colonies that were actively growing, we ensured the viability of the selected species. Finally, to preserve our collection, we made two additional copies of the colony-containing plates. One copy was stored at a very low temperature (-80 °C) as a backup, while the other was used for further analysis like PCR and species sequencing. The order of the wells was maintained to ensure accurate identification and analysis.

PCR, Sequencing and processing We performed PCR to amplify the V4 region of the bacterial 16S rRNA gene with different couples of primers for each well of the cell banks. With this approach, the primers act as labels on the amplified sequences, and the original position of the species can be identified afterwards.
My co-authors performed the sequencing with the Dada2 pipeline[121] to generate the amplicon sequencing variants (ASVs), and the Taxonomy assignment of the ASVs using the SILVA database[122].

Data analysis and Montecarlo simulations I conducted the data analysis using R[123] and generated Phylogenetic trees using the ggtree libraries[124].
I carried out Monte Carlo simulations by developing software in C++. I made use of specific functionalities from Root[125], with a focus on the TRandom class for generating random numbers.

3.2.2 Chip Preparation

I realized the scheme of the chip using CAD (Autodesk AutoCAD) and prepared the master with standard two-layer photolithography [7, 39] on a silicon wafer to create a chip master with thin (height ~ 10 μm) and thick channels (height ~ 100 μm) (scheme in Figure 3.2).
I prepared the thin channels by spin-coating the wafer with SU8-2010 (Microchem Corp., USA) at 2500 rpm for 30 seconds. I soft-baked the master at 95 °C for 2.5 minutes before exposing it through a high-precision photolithography mask (CAD files available upon request). After exposure, I baked the wafer at 95 °C for 3.5 minutes and then immersed the chip in a bath of SU8-developer (Microchem Corp., USA) for 4 minutes to remove the unexposed SU8. I rinsed the wafer with isopropanol to clean

it from the developer, and then used compressed air to evaporate the isopropanol.

I prepared the thick channels by spin-coating the wafer at 2500 rpm with SU8-2075 (Microchem Corp., USA). Then I baked the wafer for 5 minutes at 65 °C and 20 minutes at 95 °C, before exposing the layer through the second mask. Before exposing the chip to UV light, I aligned the markers included in the design of the first layer with the markers on the second mask, to ensure coherence between the two layers. The post-exposure baking was done at 65 °C for 5 minutes and 95 °C for 10 minutes. After 10 minutes within the SU8-developer bath, the unexposed resist is removed and the chip is rinsed with isopropanol and dried with compressed air.
I placed the master on a hot plate and performed the hard baking with a heating ramp from 65 °C to 195 °C in 30 minutes. Then I turned off the hot plate and waited for it to reach room temperature. Finally, I silanized the master to avoid sticking of the PDMS on the SU8 features, by placing it in a vacuum chamber with 30 μl of silane (Trichloro(1H, 1H, 2H, 2H-perfluorooctyl) Silane, Sigma Aldrich, USA), and activating the pump for 45 minutes at 10 mbar.
When the master is ready, I cover it with freshly mixed PDMS (10:1 ratio with a cross-linking agent) and oven-bake the PDMS for minimum two hours at 75 °C. I peel away the cured PDMS from the master, cut the outlines of the chip and punch the inlets for with biopsy punchers. I placed the PDMS and a clean glass slide in a plasma chamber to activate the surfaces and perform the standard plasma-bonding. I performed a hydrophobic surface modification filling the channels with a 5% v/t solution of Silane (Trichloro(1H, 1H, 2H, 2H-perfluorooctyl) silane; reference 448931 Sigma Aldrich) in HFE 7500 (NOVEC 7500, 3M, USA). I eliminated the silane solution after 20-30 minutes by flushing a stream of compressed air through the microfluidic channels.

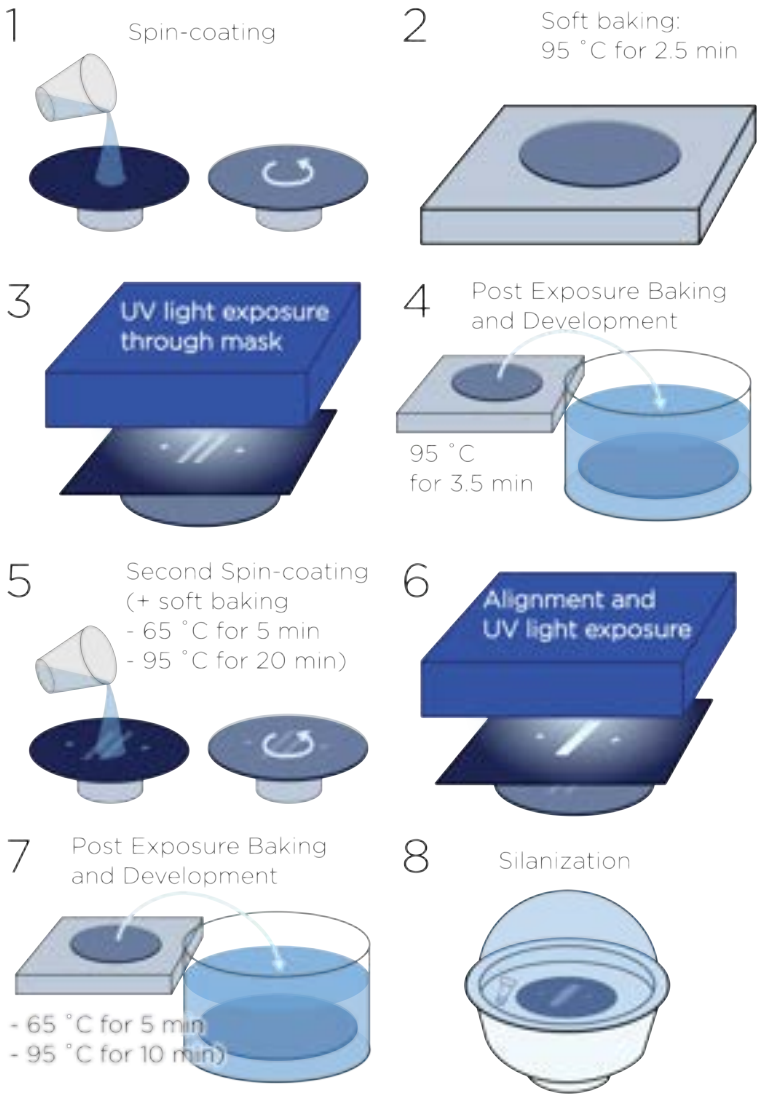

Figure 3.2: Scheme of the multilayer photolithography including 1) Spin-coating, 2) Soft baking, 3) Exposure to UV light through precision mask, and 4) Post-Exposure Baking and development of the first layer. 5) Spin-coating and soft baking, 6) Alignment and exposure to UV light, 7) Post-Exposure Baking and development of the second layer, and 8) Silanization of the master.

3.3 Results

3.3.1 Characterization of the Original Samples

First, we characterized the bacterial distribution of the samples. Using a kit for DNA extraction, we obtained 33 DNA extracts from the 18 fecal and 13 oral samples. Then, we performed the PCR reaction to amplify the V4 region of the bacterial 16S rRNA gene with a different couple of primers for each extract. The co-authors pooled the resulting amplicons together to perform the illumina sequencing obtaining ~ 1.34 million reads (for the fecal samples we obtained on average $6 \pm 2 \times 10^4$ reads, and for the oral samples $2.1 \pm 0.8 \times 10^4$). The co-authors performed the taxonomy assignment of the ASVs using the SILVA database.

Most abundant Genera in the DNA extracts I characterized the abundances from the Genera contained within the DNA extracts, and showed the overall abundances from the ten most abundant genera in Figure 3.3. For the fecal samples (Figure 3.3 a), the ten most abundant genera included *Bifidobacterium*, *Blautia*, *Prevotella*, *Bacteroides*, *Faecalibacterium*, *Ruminococcus*, *Subdoligranulum*, *Agathobacter*, *Collinsella* and *Eubacterium*, and altogether they constituted the 68% of all the reads.

Moreover, in Figure 3.3 a, I compared the abundance of each genus in different donors. I calculated the standard deviation for the abundances of each genus, and then showed the Coefficient of Variability (CV) as the ratio between the standard deviation and the avarage value of the same abundance.

These values showed a significant interindividual variation between the donors,since CV ranged from 0.41 for *Blautia* to 1.5 for *Prevotella* (dots in Figure 3.3 a). In the DNA extracts from fecal samples, we identified 183 different genera. Between these genera, 85 (46%) had a prevalence

below 20%, meaning that they could be found only in one-fifth of the of the donors.

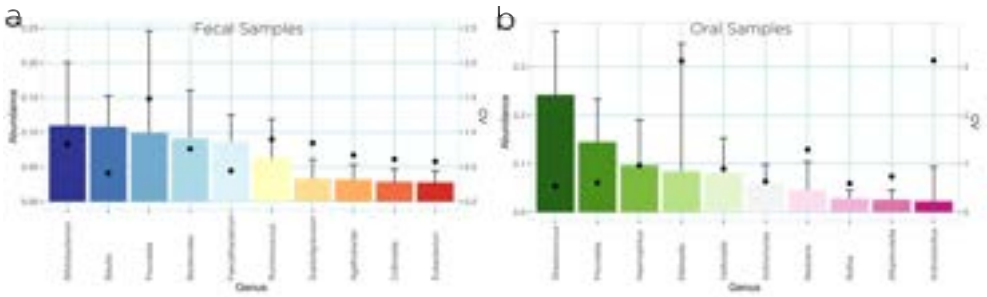

Figure 3.3: Average abundance of the ten most abundant genera for DNA extracts from (**a**) fecal and (**b**) oral samples. Histograms representing the average abundance of each genus are displayed with error bars showing the standard deviation and dots representing the coefficient of variability (CV).

Similarly, I characterized the ten most abundant genera for the DNA extracts from oral samples (Figure 3.3, b). The ten most represented genera were *Streptococcus*, *Prevotella*, *Haemophilus*, *Klebsiella*, *Veillonella*, *Actinomyces*, *Neisseria*, *Rothia*, *Alloprevotella* and *Actinobacillus*. This time, they constituted the 83% of all the reads, a significantly higher fraction of the total diversity than for fecal samples. This observation is compatible with previous studies [126], where it was shown that the number of genera dominating the bacterial diversity is smaller in the oral microbial ecosystem than in the fecal.

Over the ten most abundant genera, eight are characterised by a high prevalence (>90%) and two (*Actinobacillus* and *Klebsiella*) have a prevalence below 50%. Although *Klebsiella* constitutes the fourth most abundant genus (8.4% of the reads from oral samples), we could identify it only in five donors, corresponding to a prevalence of 38%. Actinobacillus is the tenth most abundant genus (2% of the reads) and has a prevalence of 46%.

In total, the oral samples included 81 different genera, 27 (33%) of which had a prevalence below 20%. As for the fecal samples, there was large interindividual variation in the abundances of various genera, measured with the CV (dots in Figure 3.3, b). The least variation was for *Streptococcus* for whom the CV of the abundance was 0.5, while the most variation is seen with *Actinobacillus* with a CV above 3 (Figure 2D).

Distribution of the genera for each donor Figure 3.4 depicts the distribution of the 10 most abundant genera in fecal (3.4, a) and oral (3.4, b) samples. The distribution from the oral sample of donor *D 07* stands out from the others, due to the high abundance of *Klebsiella* that was rarely if not at all seen in the other samples. This high abundance definitely influenced the value of CV observed in Figure 3.3 b. Moreover, these distributions will assume higher importance when compared with the abundances of genera in the collection of isolates.

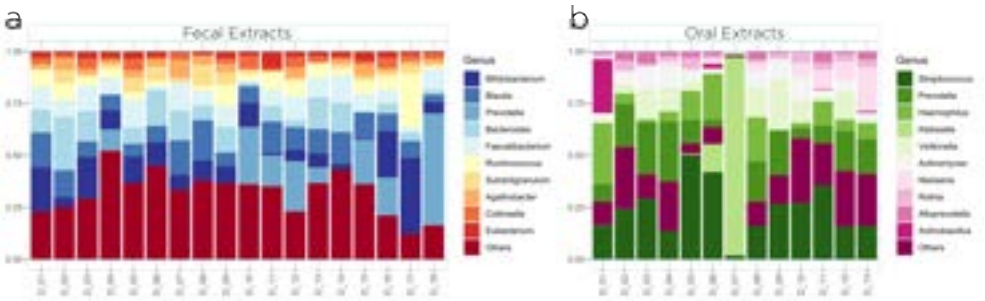

Figure 3.4: Distribution of the ten most abundant genera identified in the DNA extracts from (**a**) fecal and (**b**) oral samples. Here, the distributions are represented in relation to the donors.

3.3.2 Droplet Generation

I designed a microfluidic chip (Figure 3.5 a) based on the previously reported millipede device[39]. The chip included one inlet for the oil

phase, and one for the aqueous phase. When the bacterial suspension, pushed through the nozzles, reaches the step with the larger channels, it is passively emulsified (Figure 3.5 b) and then the oil flow flushes it to the chip outlet where we collect it in a reservoir (Figure 3.5 c).
We flushed bacterial suspension and fluorinated oil (with 2.5% surfactant) within our chip, controlling the flow of reagents with pressure controllers, at constant pressures of 600 mbar for the oil and 400 mbar for the aqueous phase.
In these conditions, the chip produced droplets with an average volume of 33 ± 2 pl corresponding to a coefficient of variance of 6%. The rate of droplet generation was 10-15 kHz, allowing us to generate around $200 - 300$ μl of emulsion (2-3 million droplets) in less than 5 minutes.

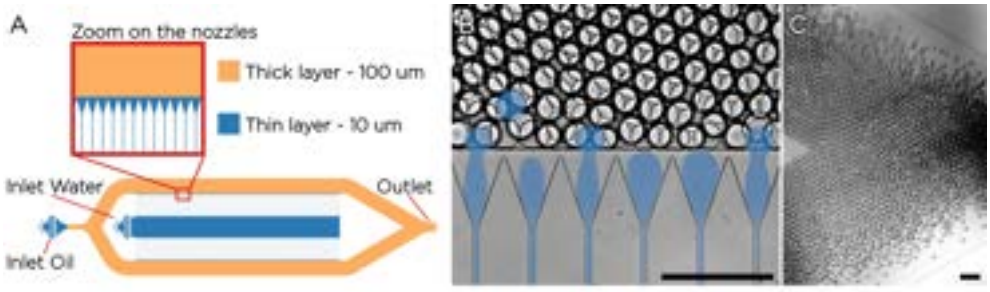

Figure 3.5: **a**) Design of the microfluidic chip with description of the channel depth. **b**) Zoom on the nozzles during droplet generation. The stream from the nozzles is highlighted with blue and one of the droplets is colorized to guide the reader. **c**) zoom on the stream of droplets collected at the outlet of the chip.

3.3.3 Creation of the Cell Banks

Following droplet generation, we incubated the droplet libraries for three days as stated in section 3.2.1. After incubation, we examined a few microliters of emulsion under the microscope to count the positive droplets,

obtaining a ratio of positive droplets between 5 and 15%. We diluted the droplets in G medium and we distributed them on microtiter plates. We diluted the droplet libraries to achieve one positive droplet per 900 μl, so that by filling each well with 90 μl, we would only observe one colony every ten wells, using the Poisson distribution once again.
We incubated the colonies for three more days and then selected the growing colonies to inoculate within the wells of the final cell banks. The cell banks were also cultured and small aliquots were inoculated within two additional copies. Finally, we used one of the copies for the PCR, sequencing and taxonomic assignment of the species.
To acquire a wide range of strains, we repeated the workflow with four different media for each sample. Having 18 fecal and 13 oral samples, we obtained a total of 124 conditions that resulted in a total of 13000 isolates (8238 fecal and 4724 oral isolates). The precise number of isolates obtained for each condition is represented in the heatmap in Figure 3.6.

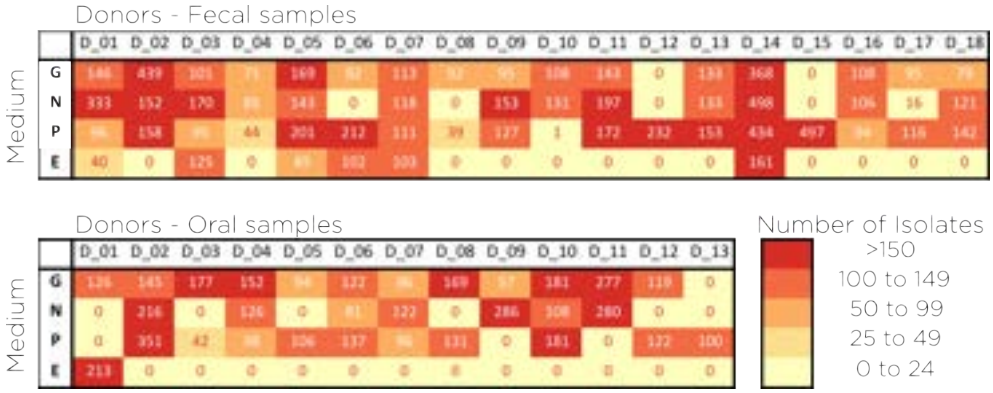

Figure 3.6: Heatmaps representing the number of isolates from each donor and each sample, in relation to the medium used for culturing.

We used a previously disclosed dual-indexing approach [127] together with NGS sequencing to do the PCR, which enabled us to label the content of each well. We received hundreds to thousands of reads of the

V4 region of the 16S gene for each well of a 96-well plate, allowing us to taxonomically identify the bacteria detected in the well. Moreover, this method enables us to identify the clonally pure wells as those that contain readings from just one strain [127].

3.3.4 Characterization of the Collection of Isolates

Once again, I characterized the abundances from the genera in our isolates collection, focusing especially on the ten most abundant (Figure 3.7).

Most abundant genera in the isolates collection *Bacteroides*, *Bifidobacterium*, *Collinsella*, *Odoribacter*, *Escherichia-Shigella*, *Butyricimonas*, *Actinomyces*, *Parabacteroides*, *Ligilactobacillus*, and *Eggerthella* were the ten most abundant genera in the bacterial collection obtained from fecal samples, accounting for 90% of the isolates (Figure 3.7 a). We detected 81 distinct genera in total; 57 of them had a prevalence of less than 20%, implying that 70% of the genera are present in fewer than one in every five donors.

The abundance distribution varied significantly across various donor samples (black dots in Figure 3.7 a). *Bacteroides* had the highest degree of homogeneity among the donors, with a coefficient of variability of 0.38. *Actinomycetes*, on the other hand, displayed the greatest variability, with a coefficient of variation of 3.5.

For the oral isolates the ten most abundant genera were *Bacteroides*, *Streptococcus*, *Klebsiella*, *Veillonella*, *Actinomyces*, *Atopobium*, *Granulicatella*, *Capnocytophaga*, *Bifidobacterium*, and *Escherichia-Shigella* (Figure 3.7 b), accounting for 84% of the collection.

The distribution of genera for the oral isolates differed significantly from donor to donor, as it did for the fecal isolates. The prevalence of the most

abundant genera confirms this high variability: just six of the ten most numerous genera have a frequency over 50%, three have a prevalence above 70%, and even the most prolific genus (*Bacteroides*) is isolated from only 62% of the donors. In total, 69 distinct genera were isolated from oral samples, with 47 of them having a prevalence of less than 20% (i.e. 68% of the detected genera).

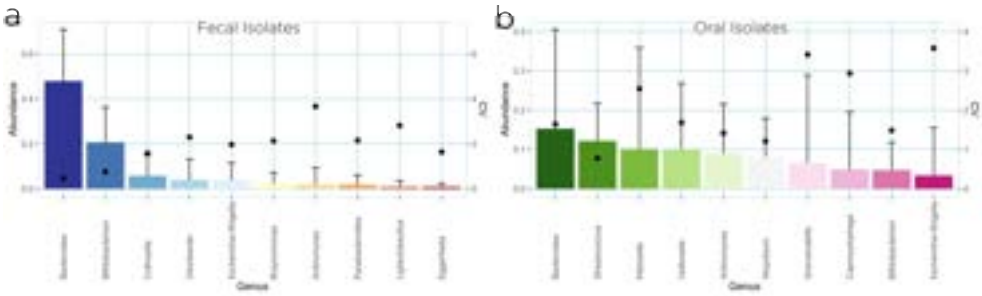

Figure 3.7: Average abundance of the ten most abundant genera for the isolates from (**a**) fecal and (**b**) oral samples. The average abundance of each genus is represented with the bars of the histograms, and the error bars show the standard deviation. The black dots represent the coefficient of variability (CV).

Genera distribution in the isolates for each donor In Figure 3.8 we show the abundance of the ten most numerous genera for the fecal (Figure 3.8 a) and the oral isolates (Figure 3.8 b).

When compared to the DNA extracts from the original samples, the distribution of the genera for the isolate collection looks less regular amongst various donors (compare Figures 3.3 and 3.4 with Figures 3.7 and 3.8). For example, the *Bacteroides* genus dominates the fecal isolates collection, accounting for 48% of all isolates. Even though, when the donors are examined individually, the abundance of this species ranges from 92% (donor 2) to just 5% (donor 18) (Figure 3.8 a).

Because the most prevalent genera have relatively low prevalence values,

the collection of oral isolates exhibits even greater swings (Figure 3.8 b). *Bacteroides*, for example, is the most common genus in this collection (15% abundance), although it is only discovered in 8 of 13 donors (prevalence 62%). *Klebsiella* is the third most common genus in oral isolates (10%), however it is identified in fewer than half of donors (46%).
Streptococcus, the most prevalent genus in the DNA extracts from oral samples (24% abundance and found in every sample), is the second most abundant genus in the isolate collection from oral samples (12% abundance), and it is detected in 12 of the 13 samples with a 92% frequency. Its CV is the lowest for oral isolates: 0.78. The same genus has a modest abundance in the Extracts from Fecal samples (0.4% abundance with 0.83 prevalence), and a lower value of abundance in the isolate collection (0.6%), being discovered in just six samples out of 18 (33% prevalence).

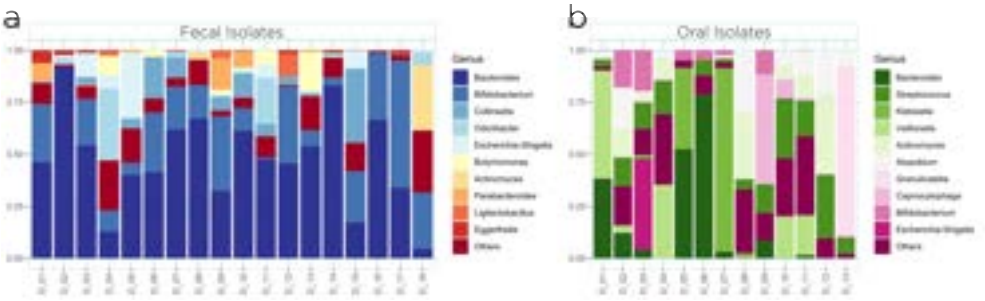

Figure 3.8: Abundance of the top ten genera identified in the collections of isolates from fecal (**a**) and oral (**b**) samples. The distributions are represented in relation to the donors.

Phylogenetic tree of the isolates Overall, the resulting bacterial collection contains at least 199 different species. We represented all these species, highlighting the phylogenetic relationships between them in the phylogenetic tree in Figure 3.9. We coloured the five branches related to the most abundant phyla with the colours in the legend.

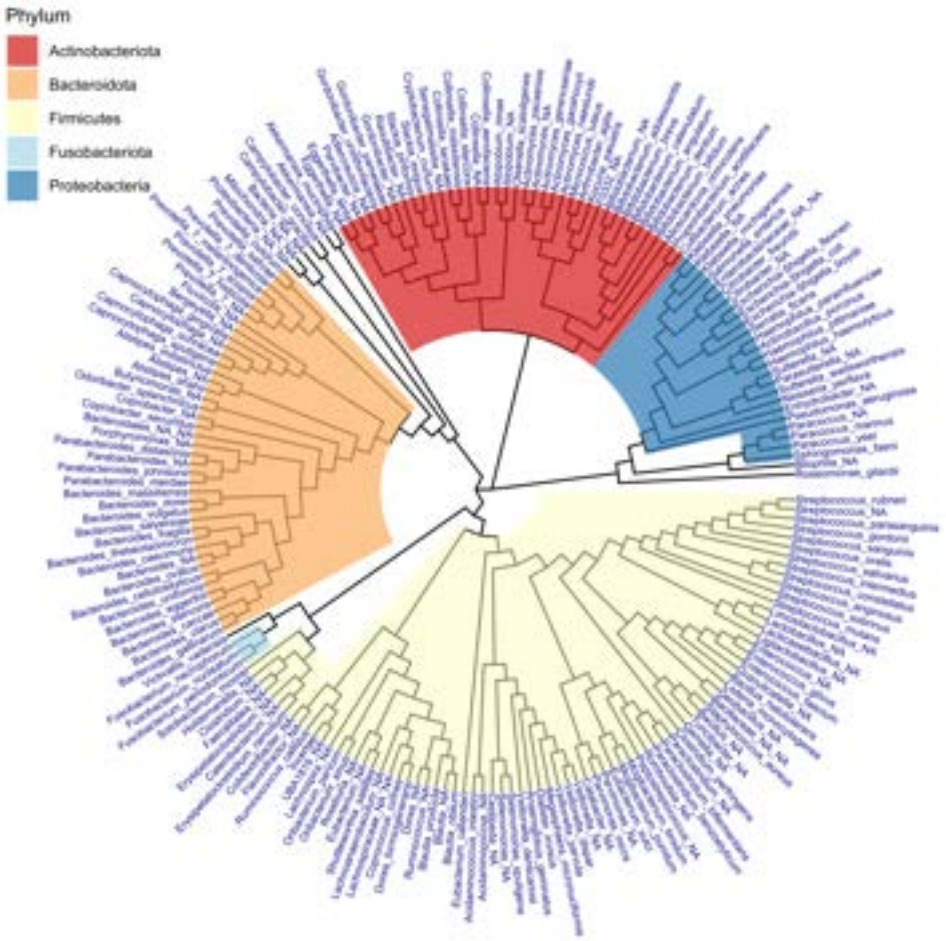

Figure 3.9: Phylogenetic tree of the species in the collection of isolates.

Complementarity of different media used for culture The goal of using diverse media to establish the strain collection was to catch a broader variety of bacteria than a single medium would enable. On average, we recovered 460 ± 300 isolates from each of the 18 fecal extracts and 350 ± 160 isolates from each of the 13 oral extracts. For each culture condition, our collection contained 114 isolates from fecal samples and 87 isolates from oral samples.

Due to the extremely selective character of the E medium, only 35 (fecal) and 14 (oral) isolates were obtained per sample.
There were 199 species in the collection of isolates from 18 fecal and 13 oral samples, which we studied in connection to the medium used to isolate them. There were 143, 88, 118, and 35 distinct species in the G, N, P, and E media, respectively. Although there was significant overlap among the strains recovered from various media (Figure 3.10), each medium also contributed to the overall variety of the bacterial collection.

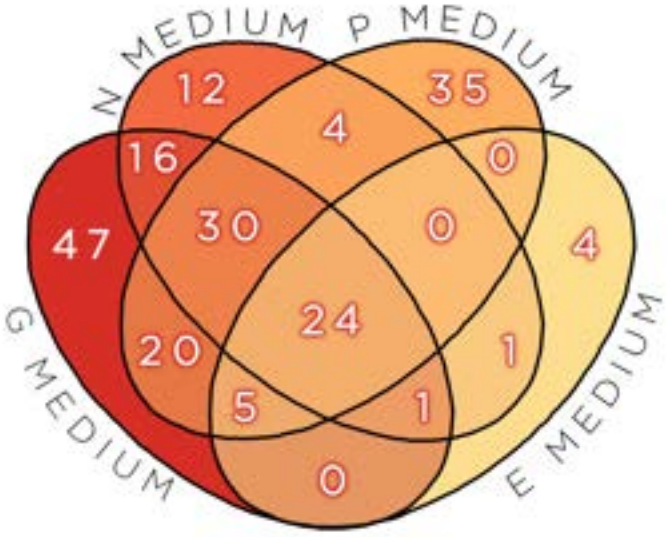

Figure 3.10: Venn diagram representing the number of species obtained with each medium and the species in common.

3.3.5 Comparison between the Collection of Isolates and the DNA Extracts from the Samples

We compared the taxonomy of the DNA extracts from the original sample, with the taxonomy of the isolates to quantify the shift in taxonomical

distribution that was originated within our workflow.

Comparing DNA extracts and isolates from fecal samples The bacterial collection from fecal samples shows a notable relative loss of *Firmicutes* and a corresponding expansion of the *Bacteroidota* and *Actinobacteria* phyla (Figure 3.11 a, left panel). For the fecal extracts, the most abundant phylum is *Firmicutes* (75%), followed by *Bacteroides* (14%) and *Actinobacteriota* (6%), while the distribution in the isolates collection shifts to 3% *Firmicutes*, 66% *Bacteroidota*, 25% *Actinobacteriota*, and 6% *Proteobacteria* and 0.1% *Fusobacteriota* that was completely unnoticed in the sample extracts.

Comparing DNA extracts and isolates from oral samples The taxonomic distributions of the original samples and the bacterial collection were more consistent in the oral samples (Figure 3.11 a, central panel). *Firmicutes* are the most abundant philum, accounting for 34% of readings in DNA extracts and 39% of isolates in the bacterial collection.
The other major phyla had similar distributions, with *Bacteroidota* being the second most prevalent (26% for extracts and 23% for isolates), *Actinobacteriota* coming in third (14% and 21%), *Proteobacteria* coming in fourth (10% and 16%), and *Fusobacteriota* coming in fifth (8% and 0.2%).

Comparing DNA extracts and isolates in the entire collection When the fecal and oral samples are combined, the variations in the relative distribution of taxa between isolates and extracts are remarkably comparable to those seen for the fecal samples. The abundance of *Firmicutes* is reduced in the bacterial collection, in favour of an increase of *Bacteriodota* and *Actinobacteria* (Figure 3.11 a, right panel).
When we observe the taxonomical distributions of each donor (Figure

3.11 b), it is clear how the majority of DNA extracts from fecal samples displayed a high abundance of *Firmicutes*, and how this philum was replaced by *Bacteroidota* in the isolates from the same samples.
For the oral samples, the distributions from different donors seem less homogeneous, and once again *D 07* stands out for the unbalanced distribution that favours *Proteobacteria* for both the DNA extracts and the isolates.

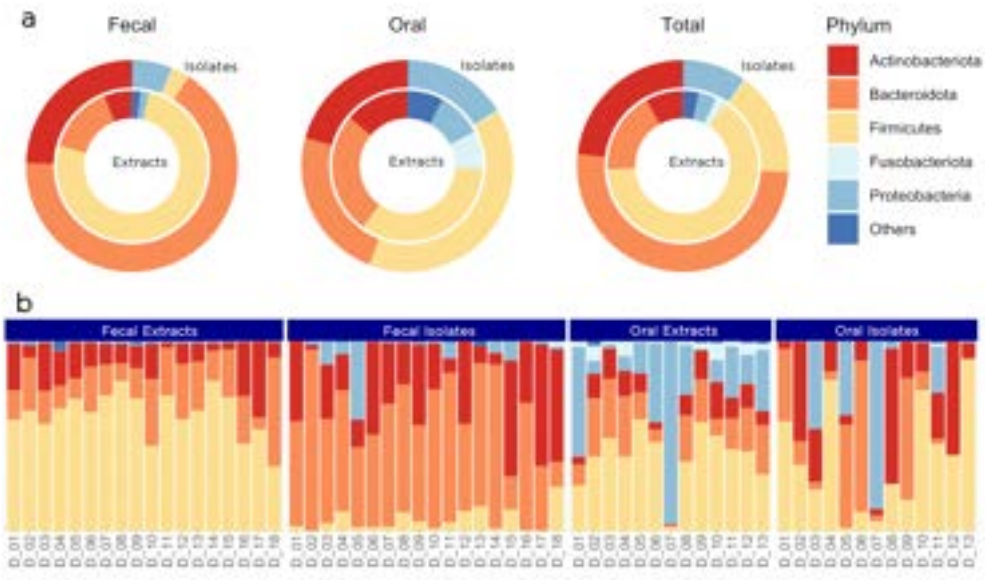

Figure 3.11: **a**) donut charts representing the distribution of the top five Phyla from fecal samples, from oral samples and from the total collection. In each chart we compare the collection of isolates with the bacteria identified from the DNA extracts. **b**) Distribution of the top five Phyla for each donor, in relation to the sample. We compare the results from DNA extracts and from the collection of isolates.

Comparison of species in DNA extracts and workflow isolates

We compared the species identified in the original extracts from fecal and oral samples with the diversity of the obtained isolates (Figure 6B and C).

Overall, the original samples contained 443 distinct species (292 from the fecal and 181 from the oral samples). The isolation of bacterial species through our workflow resulted in 199 different species, 140 from fecal and 127 from oral samples.

In total, the collection of isolates contains 146 of the species identified from DNA extracts. The sum of the abundances of these species covers 59% of the abundance distribution in the DNA extracted from the samples. Comparing the isolate collection with the DNA extracted only from fecal samples, we noticed 98 species in common (34% of the species), covering 45% of the abundance distribution (Figure 6B and C). Similarly, we obtained 69 of the species observed in DNA extracts from the oral samples (38% of the species), covering the 72% of the overall abundance (Figure 6B and C).

Interestingly, the collection of isolates included 53 species that were not observed in the sample extracts: 20 only found in the fecal isolates collection, 21 only found in the oral isolates collection, and 12 in common between fecal and oral isolates collections (Figure 6C). These 53 species were not identified in the original samples, likely due to the fact that they were present in very low abundance preventing their detection via sequencing, and they could only become detected when their biomass was amplified by laboratory culture.

One fundamental difference between extracts and isolates, is that the diversity of isolates includes all the live bacterial biomass in our cell banks, whereas the diversity of original samples just includes microbial DNA. Thus, the variety of the initial samples may contain dead microbial cells whose DNA has not degraded, overestimating the diversity of active cells.

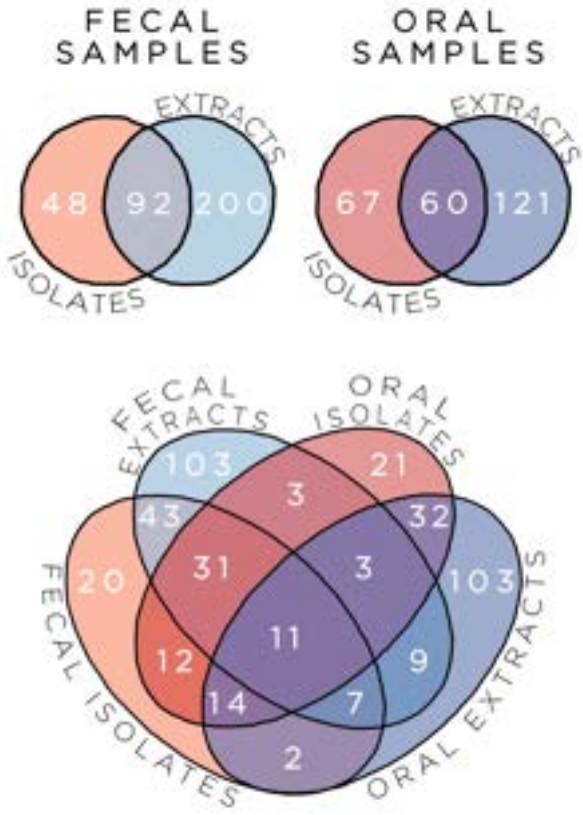

Figure 3.12: Venn diagrams comparing the number of species in the collection of isolates with the ones identified in the DNA extracts. The comparison is represented first for fecal samples, then for oral samples, and finally for all the samples together.

3.3.6 Isolation and Culturing of Previously Uncultured Bacteria

Many representatives from the human microbiota include species that share the same name between cultured and uncultured. Therefore, it is often impossible to tell whether the species we recovered has been cultured. However, we identified some taxa that show only uncultured representatives in Almeida unified catalog of reference genomes[128]. We isolated seven in lab culture: *Adlercreutzia*, *Bilophila*, *Catabacter*, *Gemella*,

Lachnospira, *Selenomonas*, *Senegalimassilia*. This shows that microfluidic culture is a valid approach to extend the domestication of fecal and oral microorganisms. We also found several isolates that could not be classified with the Silva database at different taxonomic levels[122]. We found two isolates with unassigned phylum, seven with unassigned genus, and 72 species without assignment (Figure 3.13).
It's probable that a considerable number of the isolates that couldn't be categorized taxonomically at the phylum or genus tiers have not yet been cultured in a lab setting.

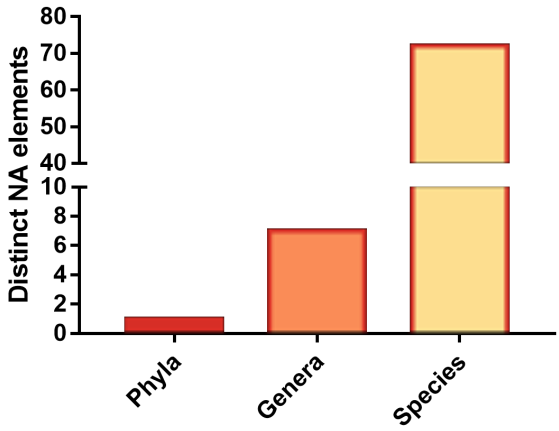

Figure 3.13: Number of isolates that were not assigned within the Silva database [122] at various levels of taxonomy.

3.3.7 Montecarlo Simulation of Bacteria Culturing

I created Monte Carlo simulations of bacterial species isolation to better understand the phenomena of culturing new species and make predictions on the anticipated outcomes from repeating the process.
These simulations include different steps that are summarised in the following paragraphs.

Designing the bacterial distribution The first step is understanding the distribution of species in the sample. We wanted to make simulations for many possible scenarios to describe a wide range of cases, starting from a low diversity of just a few species and increasing the number of total species up to a high diversity.

The most-abundant species in the human gut microbiota can be modelled as the square root of a negative exponential, while the extremely rare species are generally isolated only once during the culturing. For this reason I modelled the bacterial distribution for a number N of species S_i, coupling the exponential with a constant baseline of equally probable events, following the equation:

$$p_i = \frac{P_i}{\sum P_i} \quad \text{with} \quad P_i = e^{-\frac{i}{2}} + k \tag{3.4}$$

where p_i is the probability to find S_i, and P_i is the value of probability before normalization. In this formula, k is a parameter that is needed to increase the importance of the baseline with respect to the exponential values. In our simulations, we assumed $k = 1/20'000$ since it gave us a good approximation of the values observed in previous probability distributions.

With this formula, we generated probability distributions for a total number of species that could go from 10 to 100'000. In Figure 3.14 we show the probability distributions for 10 species.

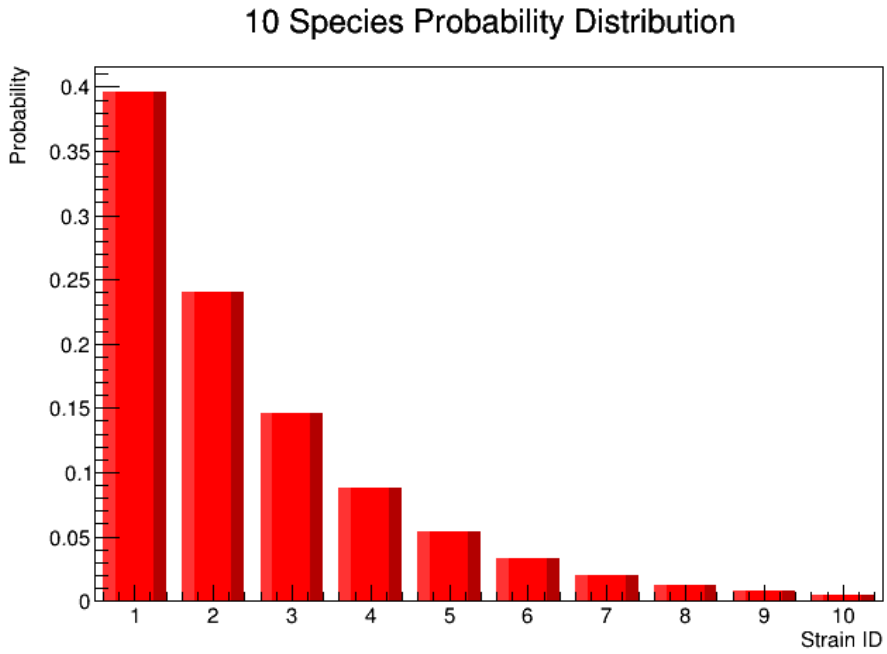

Figure 3.14: Probability distribution following the equation 3.4 for 10 different species

Simulation of events After defining the p_i, I defined ranges R_i for each species with the following equation:

$$R_i = R_{i-1} + p_i \tag{3.5}$$

with $R_0 = 0$. With this approach, the species S_i will have an interval between R_{i-1} and R_i, ending with $R_N = 1$. The width of each interval will be exactly the normalised probability p_i to find that exact species. When we generate random numbers in the interval between 0 and 1, they fall within one of these intervals, and they are counted as one event. One event represents one successful isolation of the species S_i.
We can generate an arbitrary number of events N_{events} for a selected probability distribution, and in this way, we predict the outcome of the culturing and isolation of N_{events} isolates for a taxonomical distribution

in our sample.
This allows to answer to different questions. For example, in Figure 3.15 we generated 1000, 2000,... events for different distributions that represent a pool of species going from 10 to 11'000 species. We counted how many different intervals are hit during the simulation, and we plotted the number of different intervals (number of different species isolated) in function of the total number of species assumed.

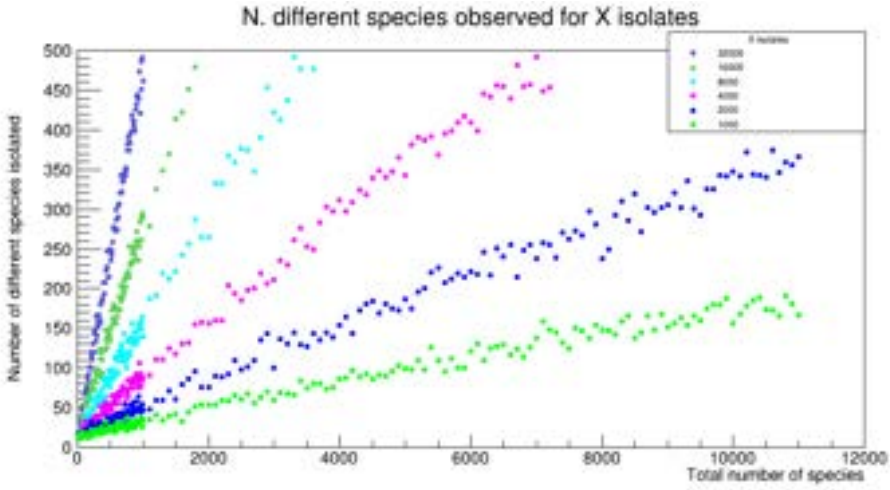

Figure 3.15: Number of different species isolated in function of the total species available in the sample. Different colours represent the results for the selected total numbers of isolates.

From this figure it appears clear how maintaining the original distribution is highly beneficial for the isolation of different species, since 1000 isolates would produce a much higher diversity in a distribution of 11'000 bacteria rather than in a distribution of 10.
Moreover, we wanted to show the number of isolates that are necessary to culture a certain percentage of the available species. For each probability distribution, we set the percentage that we aimed to isolate, and generated

events until this amount of species is found (Figure 3.16).

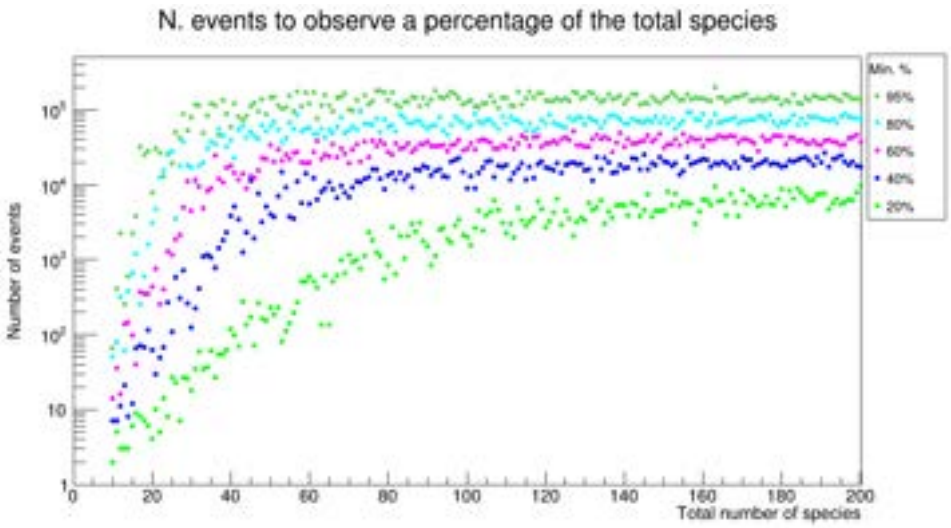

Figure 3.16: Minimum number of isolates necessary to observe a defined percentage of the total number of species in the sample. Different colours represent different percentage.

From the figure, we identify the challenge in reaching a higher percentage of species, for example, to go from 20% to 40% we might need even 10 times more isolates. This shows once again how preserving the distribution is important to isolate different species without increasing the number of isolates.
These simulations can be used as a tool to support the measures with predictive analysis. For example, from the number of species and the distribution in 1000 isolates, we could guess the total number of species in the original sample, and therefore make predictions on the expected number after repeating the workflow.

3.4 Conclusions

Within this project we showed a novel high-throughput microfluidic workflow that constitutes a promising option for the isolation, cultivation, and taxonomic characterization of bacteria from gut and oral microbiomes. This is accomplished while upholding stringent anaerobic conditions and employing diverse culture media to enhance the enrichment of varied bacterial populations.

The approach facilitates the creation of an extensive collection of bacterial strains spanning a diverse range of taxonomical units, encompassing even rare and potentially undiscovered species. This breakthrough has the potential to drive further insights into comprehending the intricate interplay of the human microbiome in both well-being and disease states. Furthermore, this work provides a comprehensive characterisation of the microbiota from 18 healthy donors in the northern France area, as well as a comparison of the diversity identified using culture-independent and culturing approaches. It's worth noting that the diversity of each of these techniques presented evidence of species that were undetected in the diversity of the alternate technique.

Finally, we created software for Montecarlo simulations. These simulations have proven useful in characterizing the cultivation of a diverse array of species, and they stand as a promising tool for generating predictions that can guide us in performing following studies.

4

Tunable Step for Droplet Generation with Dynamic Volume

Contents

4.1 Introduction

In subsection 1.2.5, we delved into the attractive attributes of Step emulsification, while also addressing some of its inherent limitations. Furthermore, in subsection 1.3.3, various microfluidic techniques for producing porous materials were explored, among them being step-emulsification.
In the context of this project, we developed a novel microfluidic device to address a specific limitation of step emulsification: the requirement to fabricate a new chip for each desired droplet size and the impossibility of adjusting droplet sizes in real-time.
The development of this design required custom procedures for the preparation of the chips and the masters. Moreover, we investigated both the generation of Oil-in-Water and Water-in-Oil droplets; this task required the development of a novel method for surface modification that we described in subsection 4.2.2. Finally, we developed a parallelized version of our design, to prove its suitability for high-througput droplet generation.

Contribution of the Author This project is the fruit of collaborative efforts involving my supervisors, Piotr Garstecki and Marco Costantini, alongside researchers from IChF and the Broad Institute of MIT and Harvard (respectively, Maria Celeste Tirelli and Witold Postek). My involvement within this project covered all the aspects from conceptualization and development of the methods, to the validation and characterization of the system, with exception for the hydrophilic surface modification, for which I only contributed in validating the method.

4.2 Materials and Methods

4.2.1 Chip Preparation

Design of the chip We designed a two-layer PDMS chip to modify the on-chip valve technology[56] positioning the thin PDMS membrane below a nozzle for step emulsification. Figure 5.3 depicts the chip, consisting of two PDMS layers bonded together on a 1 mm thick glass slide. The chip membrane and one entry for the pressurised air source are included in the thin layer (100 μm), which is in contact with the glass slide. The top layer is 5 mm thick and includes the inlets for the disperse phase, the continuous phase and the outlet to collect the generated emulsion.

Master preparation The scheme of the chip was created with CAD (Autocad, Autodesk), and the masters for the two layers were realised with two distinct approaches. 1) *Thin layer*: The master was created with standard lithography[6], coating the silicon wafer with a few cl of SU8-2050 (Microchem Corp., USA) and spinning the wafer at 3000 rpm for 30 s. The chip was soft baked for 1 minute at 65 °C and then for 6 minutes at 95 °C. Then, we exposed the chip to UV light through high precision lithography masks for 19 seconds, and performed the post-exposure baking (1 minute at 65 °C followed by 5 minutes at 95 °C). We immersed the wafer in SU8-developer (Microchem Corp., USA) for 5 minutes to remove the unexposed resist and then rinsed the chip with isopropanol. We used compressed air to evaporate the isopropanol and hard baked the chip at 195 °C for 5 minutes before allowing the wafer to cool to room temperature. To reduce the PDMS adherence on the master, we silanized the wafer by placing it in a vacuum chamber with two test tubes holding 30 μl of silane (Trichloro (1H, 1H, 2H, 2H-perfluorooctyl) Silane, Sigma Aldrich, USA), and activating the pump for 45 minutes at 10 mbar.

2) *Thick layer*: we prepared the master by CNC milling on 5 mm polycarbonate plates. We prepared the negative replica by coating the milled polycarbonate plates with PDMS and baking it for 2 hours at 75 °C. Then, we silanized the negative mold to prevent adhesion, by placing it in a vacuum chamber with silane for 45 minutes at 10 mbar.

Chip assembly 1) *Thin layer*: We used the spin coater to depose a thin layer of uncured PDMS (10:1 ratio between PDMS and crosslinking agent) on the silicon wafer. The rotation speed (1500 rpm for 30 s) and the time after mixing the PDMS with its curing agent (3 hours) were adjusted to obtain a layer with a ~ 100 μm thickness. This allowed to obtain a membrane with a ~ 50 μm thickness, thanks to the ~ 50 μm lithography-prepared features. The thin layer was baked for 2 hours at 75 °C. 2) *Thick layer*: we filled the PDMS mould (obtained from the replica of the CNC-milled polycarbonate plate) with fresh PDMS, and baked it for 2 hours at 75 °C. We removed the chip from the mould and we used biopsy punchers to create the inlets. 3) *PDMS on PDMS bonding*: we placed a few drops of PDMS curing agent on a clean silicon wafer that rotated in the spin-coater at 5500 rpm for 45 s to obtain a homogeneous thin coating. The thick layer of PDMS was gently placed on the silicon wafer to wet its surface with curing agent, and removed after a few seconds [61]. We designed a homemade frame that could be positioned on the thin PDMS layer following some alignment markers. We inserted the thick PDMS layer in the frame carefully avoiding bubbles, facilitating the alignment with the thin layer. The curing agent promoted the bonding between thick and thin layers during the overnight baking at 75°C. Then, we gently peeled away the chip from the silicon master, and punched the hole for the thin membrane inlet in the two bonded layers of PDMS. We sealed the chip with a clean glass slide via standard plasma bonding, and then baked the chip for 10 minutes at 75°C to help the adhesion of the PDMS on the glass.

4.2.2 Surface Modification

Hydrophobic surface modification We flushed the channels with a 5% w/t solution of silane (Trichloro (1H, 1H, 2H, 2H-perfluorooctyl) Silane, Sigma Aldrich, USA) in fluorinated oil (NOVEC 7500, 3M, USA) after bonding. We took care to avoid the contacts between the membrane and the glass slide, since they could bond and make the chip useless. The approach we adopted, was to place one tubing to connect the outlet of the chip with a small container filled with silane solution. We used a syringe to induce negative pressure from the chip's inlet, sucking the solution into the channels. After a few minutes, we used the same syringe to extract the fluid from the channels, and let the chip dry inside the oven at 75°C for 5-10 minutes.

Hydrophilic surface modification After bonding the chip, we placed it in a vacuum chamber, together with a test tube containing 30 ml of Vinyltrichlorosilane (ThermoFisher, Germany). We activated the pump for one hour with a set pressure of 5 mbar. Then, we removed the chip from the vacuum chamber and filled the channels with a 1% w/t solution of Gelatin-methacryloyl (GelMA) in water at a constant flow rate of 20 l/min. The flow rate was controlled with syringe pumps (Nemesys, Cetoni). Meanwhile, we positioned a source of UV light on top of the chip for 5 minutes, to activate the bonding between GelMA polymers and the previously injected Vinyltrichlorosilane. After this process, we flushed distilled water within the channels to remove the GelMA solution.
The main steps of our custom hydrophilic surface modification are represented in Figure 4.1 and discussed in the results (Figure 4.4).

Figure 4.1: Scheme of hydrophilic surface modification: following standard plasma bonding of the chip, we depose vapours of Silane on the surface, positioning the chip in a vacuum chamber with 30 μl of Vinyltrichlorosilane for 1 hour. Finally, we flush the GelMA solution inside the channels while using UV light to promote the bonding between GelMA polymers and the Vinyltrichlorosilane.

4.2.3 Droplet Generation

We used our device to generate Water-in-Oil and Oil-in-Water droplets (subsections 4.3.2 and 4.3.4). The reagents and the procedures are described below.

Reagents During the generation of Water-in-Oil droplets, we used distilled water as disperse phase, and as continuous phase we used a 2% w/t solution of surfactant in fluorinated oil (Novec 7500, 3M, USA with 2% w/t PFPE-PEG-PFPE surfactant, synthetized according to the protocol described by Holtze et al.[21]).
For the generation of Oil-in-Water droplets, we used Hexadecane (n-Hexadecane, 95%, ThermoFisher, Germany) as disperse phase, and three different aqueous solutions as continuous phases, including Gelatin-methacryloyl (GelMA), Dextran methacrylate (DexMA),and fibrinogen.
GelMA solution: a 3% w/v solution of GelMA in a previously prepared 0.5% w/t solution of Plantacare surfactant in distilled water.
DexMA solution: a 20% w/v solution of DexMA in a previously prepared solution of distilled water with 0.5% w/t surfactants (Plantacare). A

100 mg/ml solution of Irgacure (Irgacure 2959) in a 70% w/t solution of Ethanol in water was used in a 100x dilution as photo-initiator for the polymerization, and hence added to the DexMA solution shortly before experiments.
Fibrinogen solution: a 1.4% w/t solution of fibrinogen in 0.5% w/t solution of Plantacare in water.

Operational procedures We loaded two glass syringes (Hamilton gastight) with the two phases selected for emulsification. Each syringe is plugged into a 0.5 mm O.D. steel needle and then to the inlet of the chip through a Teflon tubing (0.8 mm O.D., 0.5 mm I.D.). The flowrates were regulated using precision syringe pumps (Nemesys, Cetoni) and the associated software (Nemesys user interface). A teflon tubing (0.8 mm O.D., 0.5 mm I.D.) plugged into the outlet of the chip permits to send the generated emulsion to collecting tubes. We used a pressure controller (OB1-MK3+, Elveflow) to regulate the pressure on the thin membrane, creating fixed pressure gradients or alternating pressure curves with the associated software.

Data analysis We recorded videos of the droplet generation with a camera (UI-3220CP-C-HQ, IDS, Germany) equipped with a fixed focal length lens (FL-CC2514-5M - F1.4/25mm, RICOH, Germany). We measured the droplet diameters with an automatic custom script on Fiji ImageJ[129] based on the MorpholibJ libraries[130] to identify the droplets from their boundaries, and extract their features like radius, area, and speed. Then, the droplet diameters were analysed with a custom script on Rscript[123, 131].

4.3 Results

4.3.1 Design and Working Principle of the Tunastep Device

I designed a microfluidic chip consisting on two layers of PDMS bonded on a glass slide, to recreate the on-chip microvalve technology [56, 115, 132] (Figure 4.2 a-c, g). The top layer (thick layer) includes a narrow channel that connects the inlet for the droplet phase with a wide emulsification chamber. Two additional channels connect the inlet of the continuous phase to the sides of the nozzle, to continuosly deliver external phase to the chamber. At the end of the chamber, the chip outlet allows to collect the emulsion. The square chamber located below the nozzle in the intermediate layer (thin layer) permits to adjust the nozzle section, since just a thin PDMS membrane (thickness 50 μm) separates the square chamber and the nozzle. When we increase the pressure within the middle layer channels, we deflect the membrane and consequently reduce the size of the nozzle (Figure 4.2 e, f).

We filled the chip channels with a fluorescent polymer and used a confocal microscope to examine membrane deflection at various applied pressures (Figure 4.2 f). The nozzle size decreased with the increase in pressure. For pressures greater than 50 mbar, the membrane makes contact with the opposing nozzle wall, resulting in two streams of liquid from the sides of the step, which we call side nozzles.

With increasing pressure, the cross-sectional area of the side nozzles shrinks, and then, when the pressure is released, the elastic membrane returns to its original configuration.

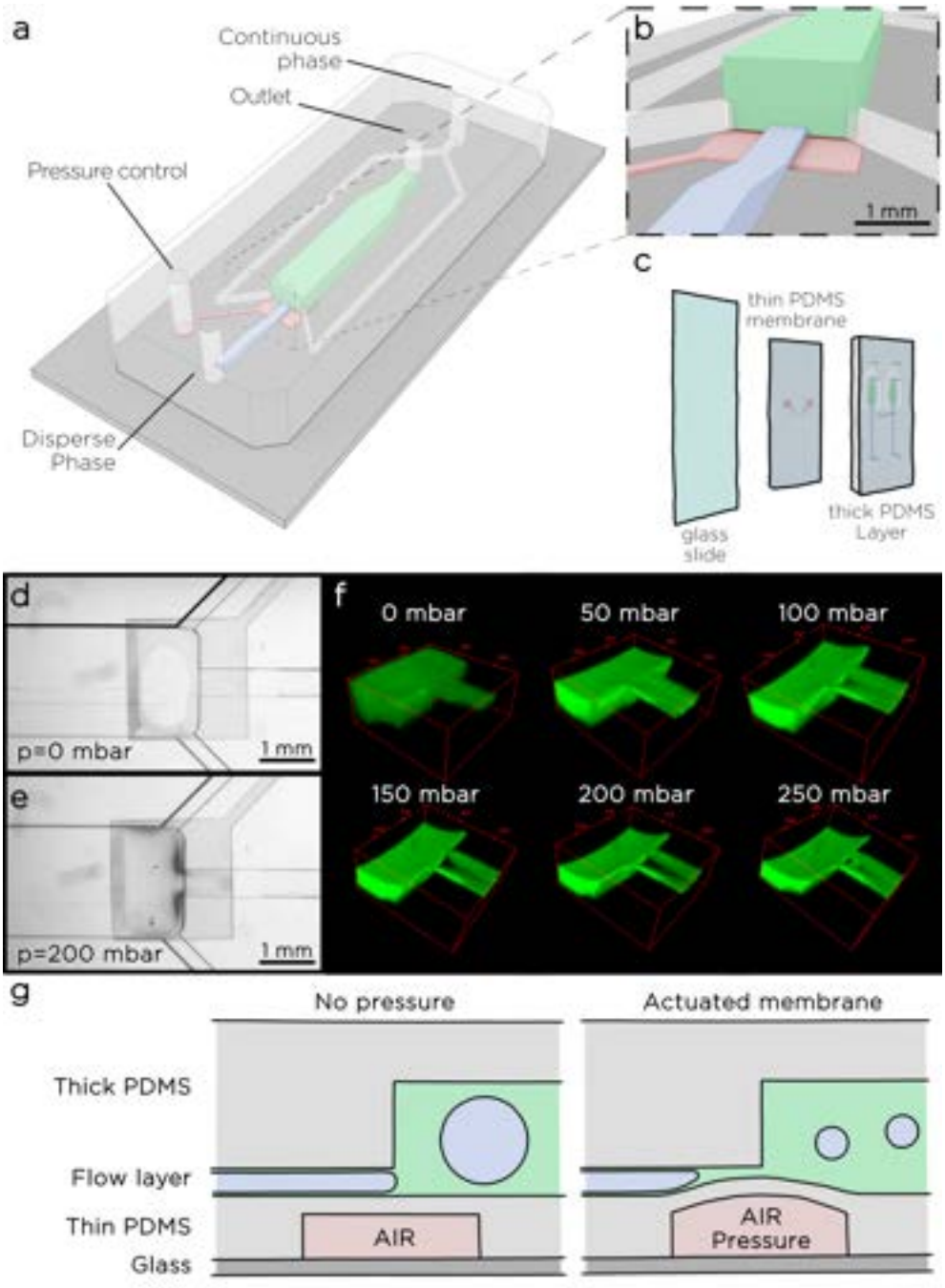

Figure 4.2: Scheme of the chip and membrane actuation. (Continued on next page)

Figure 4.2: continued from previous page
a) Scheme of the chip including one inlet for disperse phase, one for continuous phase, one for the pressure control and one outlet. **b**) Zoom on the emulsifying nozzle. **c**) Scheme of the three layers of the chip. **d, e**) Pictures of the valve with a P_m of 0 and 200 mbar. **f**) Confocal images of the chip filled with fluorescent particles during actuation. **g**) Graphical representation of the change in nozzle section with the membrane actuation.

4.3.2 Generation of Water-in-Oil Droplets

I generated droplets at a constant flow rate for the oil (1 μl/min) and different values of the flow rate for the aqueous phase (0.5, 1, 2, 3, and 5 μl/min). After setting the flow rates, I recorded the droplet generation in function of the pressure P_m applied on the actuatable membrane, beginning at 0 mbar and increasing with 10 mbar increments (Figure 4.3 a). When the system ceased running smoothly, I released the pressure and concluded the acquisition.
I observed that the maximum P_m was inversely related to the droplet flow rate: greater values of flow rates were accompanied by lower values of the maximum pressure viable for stable and reliable generation of droplets.
When the nozzle was not operated, the maximum diameter of the droplets was observed, and then the volume decreased inversely to the applied pressures, as expected. I observed that high flow rates might push the non-actuated membrane towards the glass during droplet production, without constituting a real issue for the droplet formation. Moreover, at P_m= 10 mbar, the membrane was not deflected reliably, due to the too-low applied pressure, therefore we measured droplets with inconsistent sizes at this pressure (see larger error bars in Figure 4.3 b). The generation returned reliable at 20 mbar and higher pressures (Figure 4.3 b). We obtained droplets with diameters in a range between 64 ± 4 μm and 551 ± 2 μm corresponding to volumes between 140 ± 30 pl and 88 ± 1 nl.

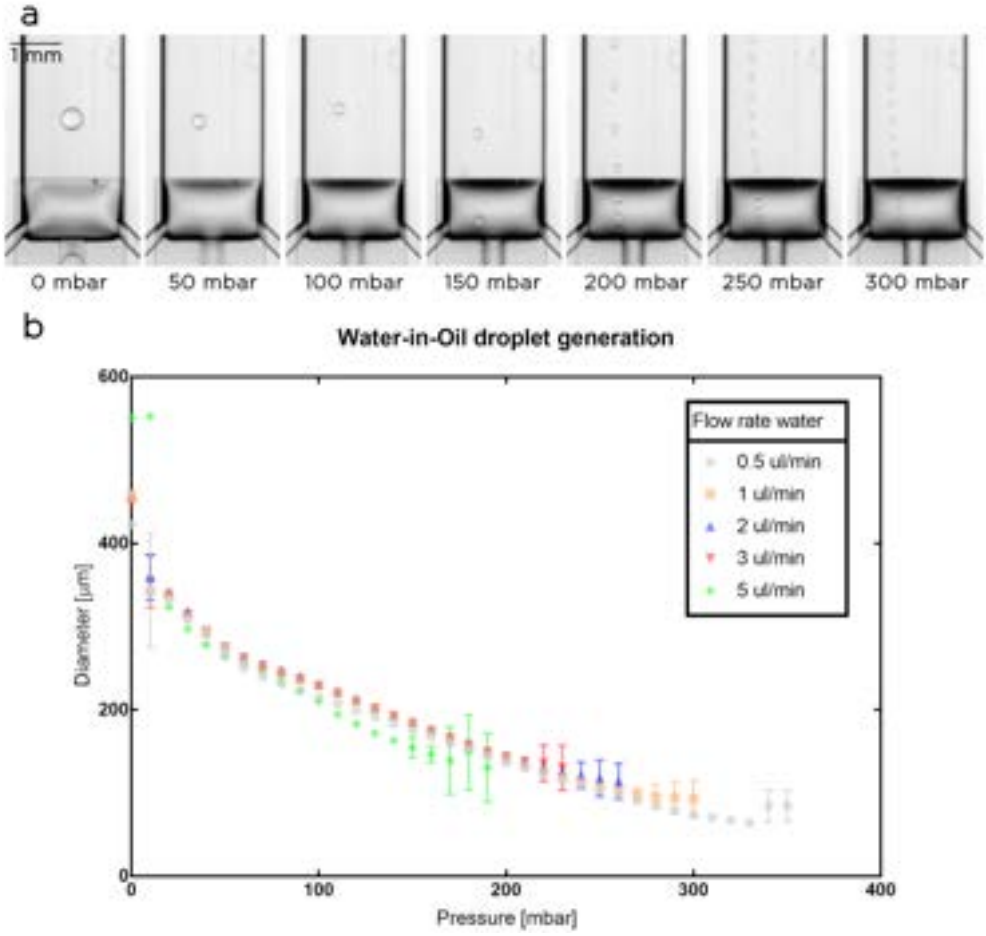

Figure 4.3: Generation of water-in-oil droplets. **a**) Pictures of droplets generated at a stable flow rate, increasing the pressure on the membrane layer. **b**) Graph representing the diameters of droplets in function of the pressure applied on the membrane. The flow rates of the aqueous phase (0.5, 1, 2, 3, 5 μl/min) are represented by different shapes and colours of the dots. The flow rate of the oil phase was 1 μl/min.

4.3.3 Novel Surface Modification

We adapted the chip for the production of O/W emulsions with a custom surface modification that met two critical requirements: i) hydrophilic surfaces within the microfluidic channels to avoid droplets sticking to the surfaces, and ii) impermeability of the chip to the organic solvents used as dispersed phase, since PDMS is significantly permeable to the majority of these compounds [133].
We investigated our surface modification for long-term emulsion generation, first validating the hydrophilicity of the surfaces (Figure 4.4, second row), and then their impermeability to the oil phase during droplet generation (Figure 4.4, third row).

Hydrophilicity of the surfaces The surface modification is accomplished through two steps: i) coating the microchannels with vinyltrichlorosilane, and ii) flushing a Gelatin-methacryloyl (GelMA) water solution (containing a photoinitiator) in the channels under UV light to chemically bond GelMA polymer chains to the vinyl groups previously introduced onto the PDMS surface. As a result, we compared water droplet contact angles on three PDMS slices: i) untreated PDMS, ii) PDMS after silane coating, and iii) PDMS after total surface modification. The contact angle of untreated PDMS was $116.5 \pm 0.6°$, as shown in Figure 4.4; following silanization with vinyltrichlorosilane, the value reduced to $107.7 \pm 0.3°$, whereas the one of GelMA-treated PDMS was $71 \pm 8°$, indicating the hydrophilicity of the PDMS surface.

Long term generation of O/W droplets We utilized hexadecane as the droplet phase to create O/W emulsions and captured time-lapse movies for up to 24 hours. While the droplet generation in the surface-modified chip remained stable for the entire study period (24 hours of emulsion generation), the other two chips (plasma bonded only, plasma bonded and silanized) showed visible swelling of the PDMS channels after 30 minutes (Figure 4.4).

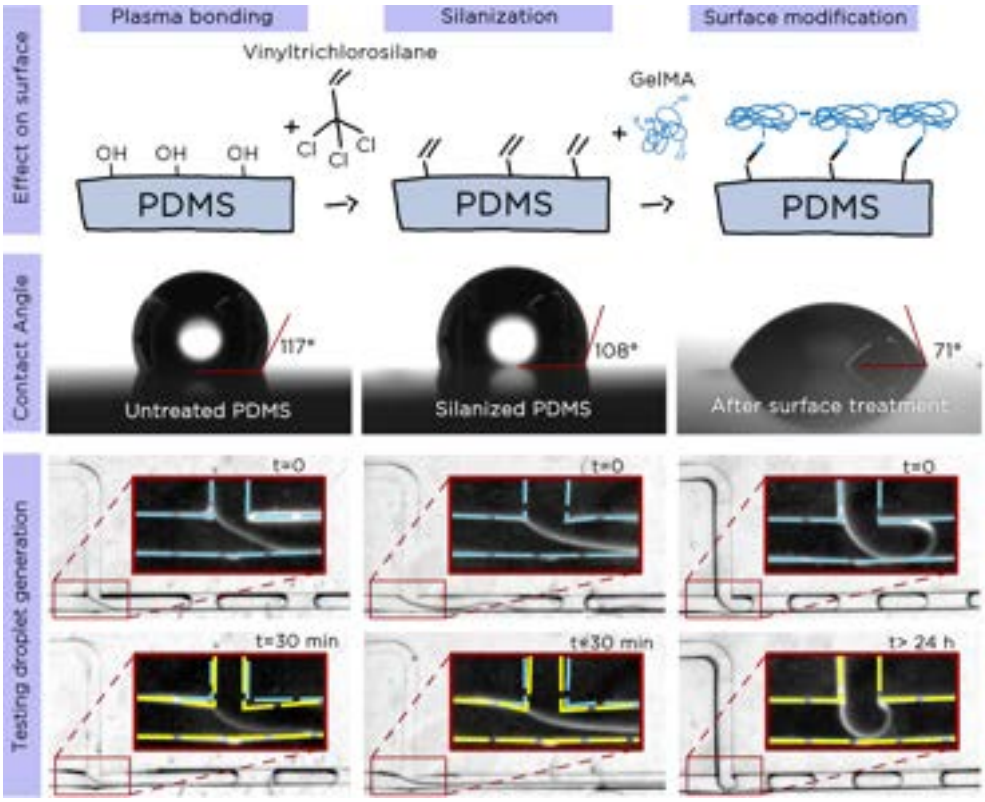

Figure 4.4: Surface modification. First row: scheme of the chemical composition on the surface of PDMS. Second row: measures of contact angle of water drops on untreated PDMS, silanized PDMS and after surface modification. Third row: test of the surface modification during droplet generation. To help the reader, we highlighted in blue the channels at t = 0, and in yellow the channels after the measured time.

4.3.4 Generation of Oil-in-Water Droplets

After developing the surface modification (Subsection 4.3.3), we tested the hydrophyllically modified Tuna-step device for the generation of Oil-in-Water droplets with three different biopolymer solutions, including Dextran methacrylate (DexMA), Gelatin-methacryloyl (GelMA), and fibrinogen, as aqueous phases. These biopolymers are often employed in the manufacture of porous hydrogels which are useful in tissue engineering. We chose one of these polymers (DexMA) as the constituent material for 3D printing of porously graded hydrogels in chapter 5. The oil selected to constitute the disperse phase was hexadecane.

We tested one flow rate for the aqueous phase (1 μl/min) and three flow rates for the oil phase (0.5, 1, and 2 μl/min), generating emulsions with volume fractions of 33%, 50% and 67% respectively.

The Tuna-step device produced O/W droplets very similarly as it produced W/O droplets. With the unactuated membrane, we reached the maximum droplet volumes, and then, as P_m increased, and the nozzle square-section decreased, we obtained smaller volumes. We observed that the droplets were generated near the nozzle's center location at low values of P_m, but when we increased P_m, they displayed a preference for one side of the actuated nozzle. We noticed that we could shift the preferred side with a slight tilt of the chip. Also in this case, an additional increase in pressure deformed the membrane with the change in step geometry that created two distinct side nozzles (Figure 4.5 a). The two nozzles generated droplets in parallel until the critical pressure was reached, bringing to an unstable droplet generation.

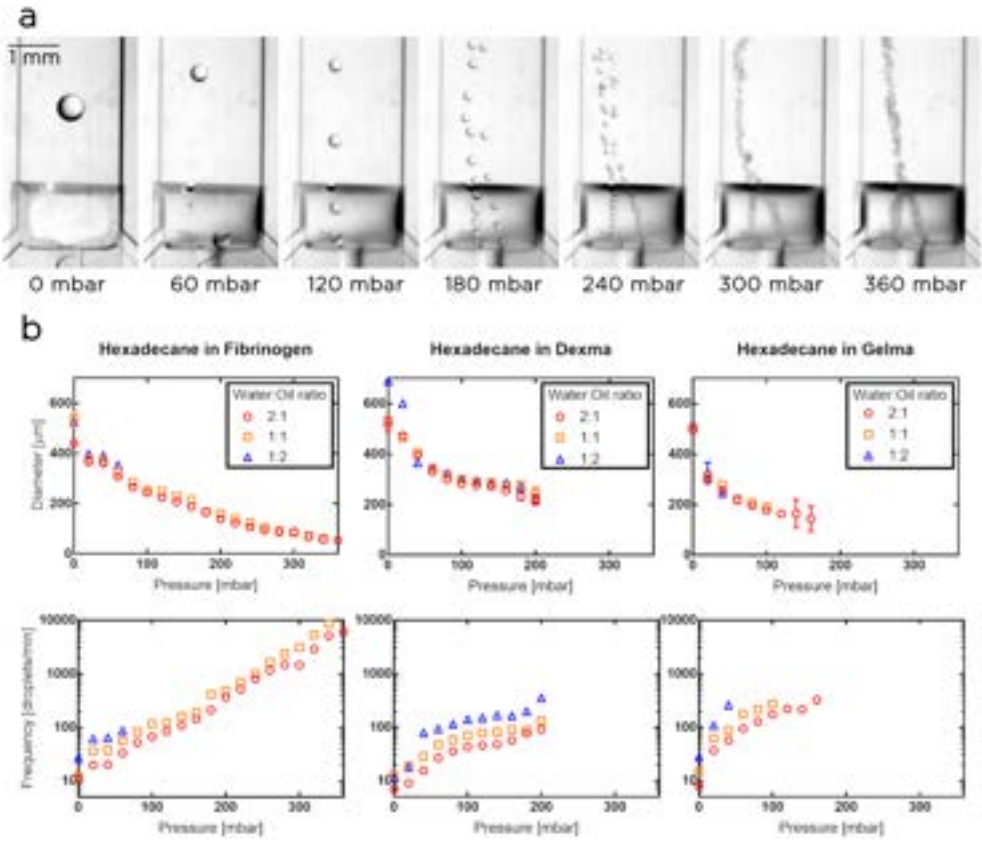

Figure 4.5: Generation of oil-in-water droplets. **a**) Pictures of droplets generated at a stable flow rate, increasing the pressure on the membrane layer. **b**) Graphs representing the change in diameter and in droplet generation frequency, in function of the pressure applied on the membrane. The graphs are for hexadecane droplets in three different solutions of fibrinogen, DexMA and GelMA. The flow rate of the aqueous phase was stable (1 μl/min) and the flow rate of the disperse phase was changed to obtain differnt ratios between water and oil (2:1, 1:1, 1:2, respectively represented by circles, squares and dots.

Different aqueous phases provided different dynamic ranges of the droplet sizes, as shown in Figure 4.5 b: i) for the fibrinogen solution,

we obtained droplets in a range between 54 and 538 μm in diameter, corresponding to a volume range of 82 pl and 82 nl; ii) for the DexMA solution, droplets had a diameter between 218 and 688 μm, corresponding to a volume range of 5 and 170 nl; iii) for the GelMA solution, droplet diameters varied between 143 and 518 μm, corresponding to a volume range of 1.5 and 73 nl. The droplets generated with the fibrinogen solution had the widest pressure range, reaching 360 mbar, and the widest range of volumes (3 orders of magnitude). However, in Chapter 5 we selected DexMA to synthesize porous hydrogels, since in comparison with the other two biopolymers, it can be photopolymerized easily and quickly, and the resulting gels have greater stability and mechanical response[134, 135].

4.3.5 Parallelization of the Tuna-step Nozzle

I designed a microfluidic device with 14 parallel nozzles to show the adaptability of Tuna-step for parallelization. In the parallelized version, one single inlet delivers the droplet phase to 14 parallel nozzles that are aligned with a large membrane (Figure 4.6). The inlet channel has a height of 400 μm while the narrow nozzles are thinner (100 μm) to guarantee stronger hydrodynamic resistance in the nozzles.
We used a linear slope connection (previously described in [54]) to achieve a smooth transition between intake and nozzles. This design criterion is critical for ensuring a balanced flow rate for each nozzle and encouraging emulsification homogeneity.
I calibrated and tested the multi-nozzle Tuna-step chip for the generation of water droplets in NOVEC 7500 oil (with 2% w/t surfactant). I started with a constant flow rate of 60 μl/min for the oil phase and 34 μl/min for the water (Figure 4.6 a), applying increasing values of P_m until I reached 200 mbar. The droplet production became unstable above this value of P_m, so I reduced the flow rates to 14 μl/min for the oil and 8 μl/min for the water, and increased the pressure up to 300 mbar (Figure 4.6 b). I

measured the droplet diameters and observed a progressive reduction, with a diameter range between 150 ± 10 μm to 460 ± 20 μm, corresponding to volumes ranging from 1.8 ± 0.4 nl to 51 ± 7 nl (Figure 4.6 c).

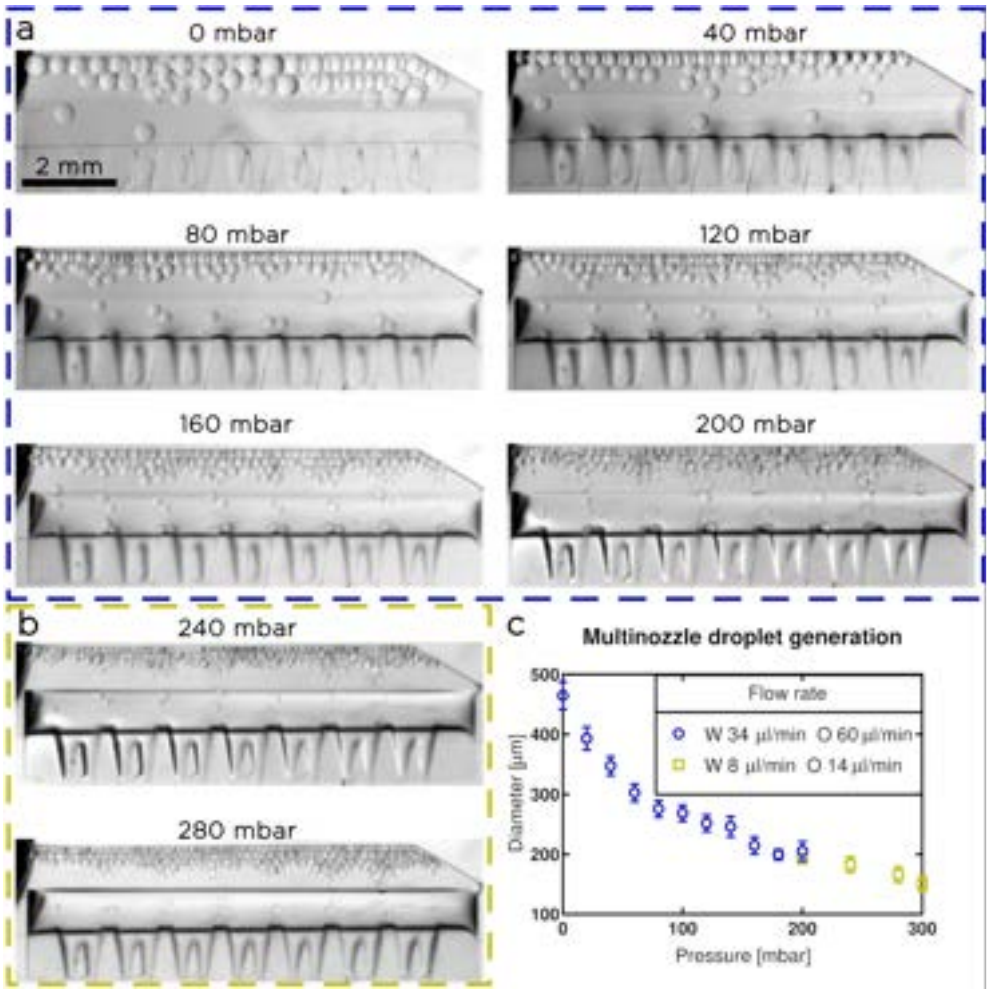

Figure 4.6: Generation of Water-in-Oil droplets in the parallelized tuna-step device. **a**) Droplet generation with membrane actuation in a range between 0 and 200 mbar while keeping constant flow rates for oil (60 μl/min) and water (34 μl/min) **b**) Droplet generation at 240 and 280 mbar, keeping a flow rate of 14 μl/min for the oil phase and 8 μl/min for the aqueous phase. **c**) Average droplet diameters in function of different P_m. Different colours represent the two flow rate regimes used to generate emulsion.

4.4 Conclusions

The main focus of this project was Tuna-step, a novel microfluidic system for manipulating droplets that effectively overcomes a key limitation of step emulsification: the fixed droplet size.
Through the implementation of Tuna-step, a spectrum of droplet sizes and compositions was successfully generated utilizing a dynamic step-emulsifying nozzle. Rigorous characterization of our device under varying flow rates was conducted to ascertain the operational parameters for both oil-in-water and water-in-oil emulsions. By modulating the pressure applied to the Tuna-step membrane, consistent reduction in droplet size was achieved across the entire range of tested flow rates.
To allow the production of oil-in-water emulsions, we developed a specialized hydrophilic surface modification, effectively preventing PDMS swelling in the presence of hexadecane oil. With this adaptation, we achieved the continuous production of oil-in-water droplets for more than 24 hours.
Moreover, we proved the suitability of the Tuna-step configuration for parallelization, enabling the simultaneous operation of 14 nozzles to create tailor-made emulsions.
We anticipate further development of our technology with the increase in the parallelization of these systems, paving the way for high-throughput emulsion generation while actively controlling droplet size regardless of flow rate or volume fraction.

5

3D Printing of Functionally Graded Porous Materials

Contents

5.1 Introduction

In subsection 1.3.3, we explored different microfluidic-based approaches for 3D printing porous functional materials, underlining the potential implications of these strategies.
Indeed, the ability to incorporate compositional, micro-architectural, or combined gradients within a single material holds the promise of generating an almost boundless array of novel materials with uniquely customized structural and functional attributes. Even though early research has shown promising foundations, the field is still in its early stages, and there are a number of technical problems that need to be solved before these ideas can be turned into useful, advanced solutions. More specifically, it would be required to overcome the challenges related with the throughput of production and achieve precise, on-demand control over parameters such as droplet size, volume fraction, and spatial arrangement.
In this chapter, we discuss our strategy for addressing these challenges, which grants us enhanced control over local properties of the material such as porosity and composition. Our method involves the integration of 3D printing techniques for porous materials with the customized chip design outlined in Chapter 4. This innovative design permitted to extrude emulsions while decoupling the flow rate from the droplet size.
As proofs of our method, we performed 2.5D printing to show the change in porosity, 3D printing of self-sustaining porous hydrogels, and multimaterial printing.

Contribution of the author My involvement in this project aligns with what is outlined in Chapter 4, except for the creation of the custom 3D printer that was available from a previous project.

5.2 Materials and Methods

5.2.1 3D Printing

The 3D deposition of emulsions requires to extrude the emulsion from a printing nozzle that can be controlled on the XYZ directions. We positioned our chip on a motorized XYZ stage (Figure 5.1, a) to ensure a small dead-volume and a short delay between the emulsion generation and the extrusion. A thin teflon tubing connected the outlet of the chip to the printing nozzle, that could be immersed in the supporting bath where the emulsion was extruded.
The process to produce 3D porous materials included four steps, represented in Figure 5.1, b: 1) 3D design of the features and generation of the code for the XYZ movements 2) production of emulsion and 3D printing in the supporting bath, 3) exposure to UV light, and finally 4) extraction of the material from the supporting bath.

Production of emulsion We stored Hexadecane oil and DexMA solution in glass syringes (Hamilton gastight) to generate Oil-in-Water emulsions. The DexMA solution was prepared as described in 4.2.3, and the photo-initiator was added to the solution shortly before printing, to avoid the polymerization of materials before extrusion. The two syringes, controlled with syringe pumps (Nemesys, Cetoni), were connected to the chip on the motorized stage through teflon tubing (0.8 mm O.D. and 0.5 mm I.D.), and the pressure acting on the thin membrane was controlled with a pressure controller (OB1-MK3+, Elveflow). We generated pressure curves following custom functions, including gradients, square functions and gradual decrease.
When testing multi-material printing (Figure 5.4), we prepared two syringes of DexMA solution with a few mg/ml of fluorescent dyes to show the change in external phase. We modified the chip design with a two-channel inlet split that allowed to transition smoothly between the two materials without interrupting the droplet generation.

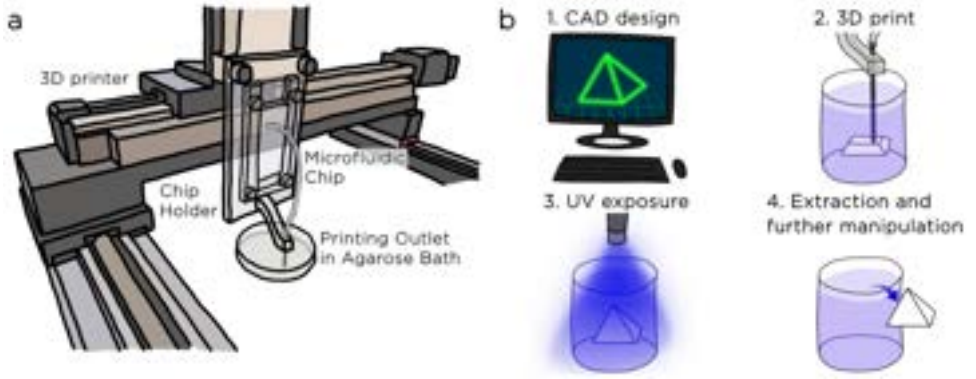

Figure 5.1: a) Scheme of the configuration for 3D printing: we mounted the chip on a holder attached to a custom 3D printer. The outlet of the chip is connected to a metal needle that acts as a printing nozzle. The needle is immersed in an agarose bath. b) Scheme of the procedure fo r3D printing of porous materials: 1) CAD design of the object and generation of the *.gcode* file to instruct the 3D printing. 2) Extrusion of the emulsion in the agarose gel, following the XYZ movements. 3) Exposure of the printed material to UV light to solidify the structures. 4) Extraction and further manipulation of the printed object.

Generation of the code for XYZ movements We designed the 3D models of the object with computer-aided design (CAD, Autodesk Inventor), and we used a free software (Slic3r) to convert the CAD file into a file holding the instructions for the XYZ motions of the printer stage (G-code file). The fixed parameters for the automated slicing of the 3D models were i) nozzle diameter of 0.5 mm and ii) slice thickness of 0.2 mm.

To realize custom patterns like the chess pattern in Figure 5.2, we designed the curves on Autodesk AutoCAD, and exported the file on a free vector graphic software (Inkscape) to use a free extension (Gcodetools) to generate the G-code file following a constrained curve. Without our customized slicing process tailored to the specific object, automated slicers would optimize paths by deviating from the intended pattern. This occurs because slicing software is primarily designed for optimizing the

printing of solid plastic materials, operating on a different logic compared to the intricate 3D printing of emulsions.

5.2.2 Preparation of the Supporting Bath for 3D Printing

3D printing emulsions to create self-sustaining porous structures necessitates the use of a supporting sacrificial material onto which the emulsion may be deposed during extrusion, and held until the emulsion exterior phase is polymerized by the UV light radiation. The supporting material should meet two conditions: 1) keeping the extruded material in the exact position where we extruded it, and 2) allowing the nozzle to move freely without disrupting its movement or the surrounding material, i.e. it should be a yield-stress fluid that behaves as a solid if we apply a shear stress below a yield value, and as a liquid if we exceed this value. Furthermore, the material must be translucent in order for UV light to reach the printed emulsion.

For this purpose, we prepared a solution of water with agarose spiky microparticles, as previously reported[108], which we employed as a sacrificial supporting material. We added 0.5% w/t agarose in water and autoclaved the solution for 20 minutes at 121 °C. During the autoclaving, the agarose melts and the solution is sterilized. The solution was then allowed to cool overnight while being stirred at 700 RPM. The progressive reduction in temperature, together with the stirring, produced the microparticles necessary for the agarose fluid gel.

5.3 Results

I connected the Tuna-step device (Chapter 4) with a custom 3D printer to demonstrate how our device may be used to generate functionally graded hydrogels (Figure 5.1). On the motorized stage, the chip was put on a special chip holder, and the outlet was attached to a metal needle. During the printing process, the needle moves smoothly through an agarose fluid gel that serves as a support material for the extrusion of the emulsion. It was recently shown how this method may be useful for 3D printing, enabling complex structures to be printed independently of the viscosity of the extruded material [108].

5.3.1 2.5D Printing in Agarose Gel Bath

Initially, I generated droplets of Hexadecane in DexMA solution, and tested the extrusion of emulsion within the agarose bath. To have a clear view over the position and size of the deposited droplets, I used a planar XY movement of the nozzle to print several 2.5D emulsion patterns while using varied pressure profiles for membrane actuation (Figure 5.2).
I proved that our technology is capable of producing sophisticated spatial emulsion patterns by synchronizing pressure profiles with robotic motion control (see, for example, the chess spatial organization of tiny and large droplets). Figures 5.2 c and d show how two independent printing pathways (serpentine and chess-like movements) syncronized with the identical square-function pressure profile resulted in diverse spatial configurations. We demonstrated how the synchronization of pressure profiles with spatial deposition enables the creation of a broad variety of spatial structures that would be difficult to replicate without the use of microfluidics and 3D printing.

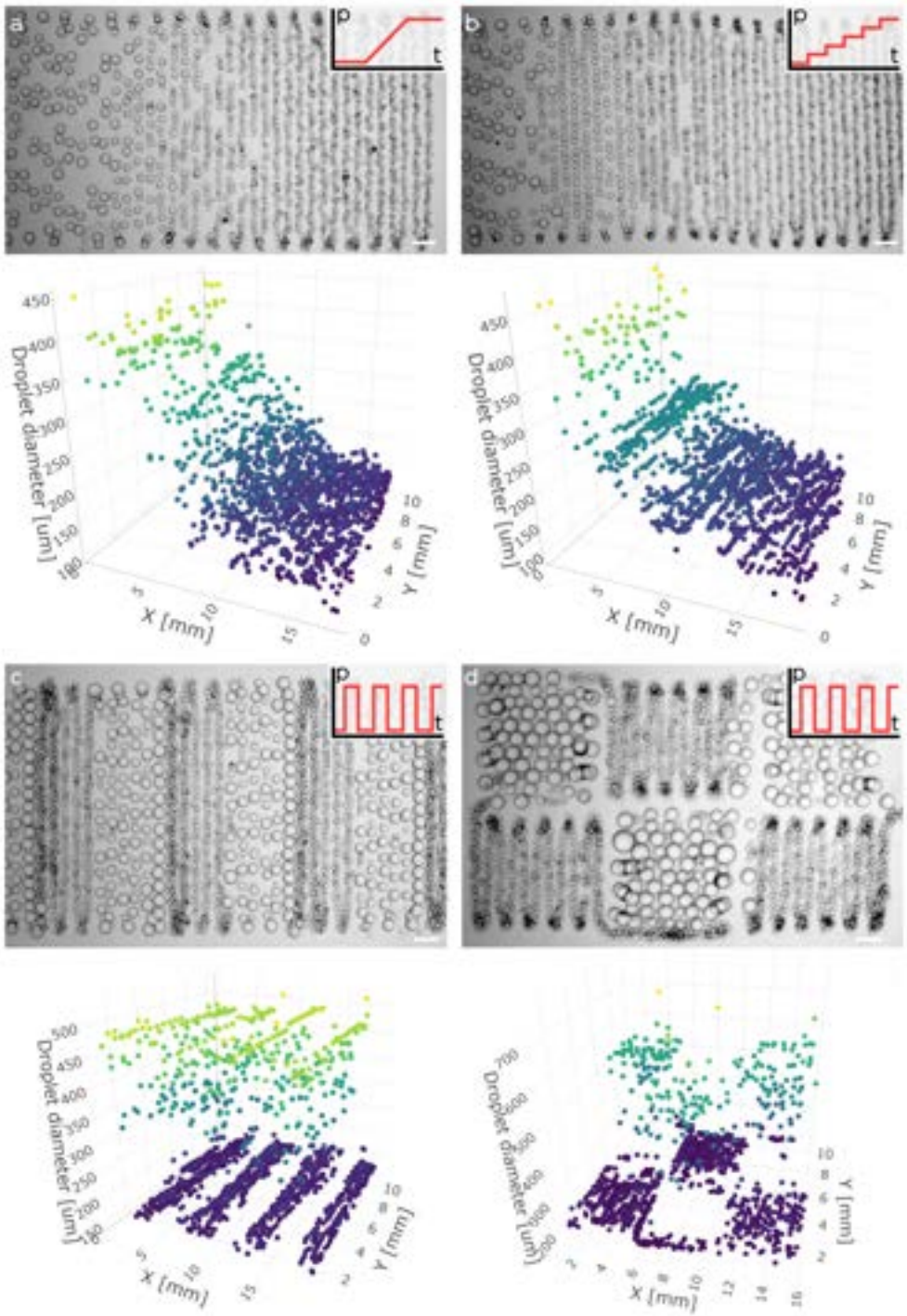

Figure 5.2: 2.5D extrusion of emulsion. (Continued on next page)

Figure 5.2: continued from previous page
The emulsion, once printed, is photographed before UV light exposure, to enhance droplet visibility. In each illustration, we integrated the nozzle's two-dimensional motion with alterations in pressure. Specifically, we applied a gradient of increasing pressure (**a**) an incremental increase in pressure (**b**), and a periodic square function for (**c**) and (**d**). Corresponding graphs beneath each illustration depict how droplet size varies with spatial position. The 2D patterns predominantly follow a sinusoidal trajectory, with the exception of image (**d**), which follows a chessboard-like path.

5.3.2 3D Printing of Porous Hydrogels

After testing the synchronization between emulsion generation and 2.5D spatial deposition, I proceeded to test the 3D printing of self-standing porous structures. To demonstrate the capabilities of our technology, we chose six unique geometries, ranging from simple platonic solids and rotational figures, to more sophisticated constructions such as the double cone with cavities. We used a free software to generate g-code files to control the movement of the stage, starting from the 3D CAD drawings in Figure 5.3 a. To enable a quicker printing, we used an O/W emulsion with a 20% oil volume fraction that we deposed in an agarose fluid gel bath (Figure 5.3 b). We exposed the structures to UV light after printing and then took them from the support bath to demonstrate their suitability for further manipulation (Figure 5.3 c).
The constructions exhibited only small differences between the model design and the printed material, proving the technique's practicality.

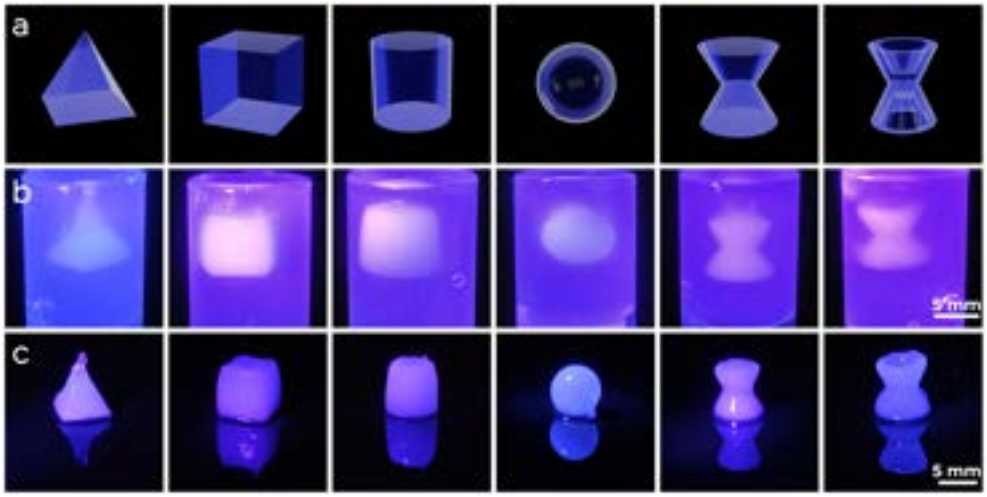

Figure 5.3: 3D printing of porous structures. **a**) 3D models of the objects to print. **b**) 3D objects in the agarose gel bath. **c**) 3D objects after removal from the supporting material and rinsing with water.

5.3.3 Multimaterial Printing

In the end, we decided to demonstrate Tuna-step's usefulness in the manufacture of products with changing compositions. To print multi-materials, I modified the chip design with a Y-junction connector incorporated into the continuous phase inlet (Figure 5.4). This design allowed us to connect two distinct solutions.

For a clear visual representation, we opted once again for 2.5D printing, and this time we prepared two DexMA solutions containing modest quantities (a few mg/ml) of two different fluorescent dyes. We kept the two reagents in syringes and used syringe pumps to regulate them. We created two distinct flow profiles to have an automated switch between syringes with the program to control presssure pumps pressure pump. To have an automatic transition between syringes, we built two separate flow profiles. We printed three complicated designs (chess pawn, beer cup, and concentric circles) with visible change in composition and porosity, as shown in Figure 5.4.

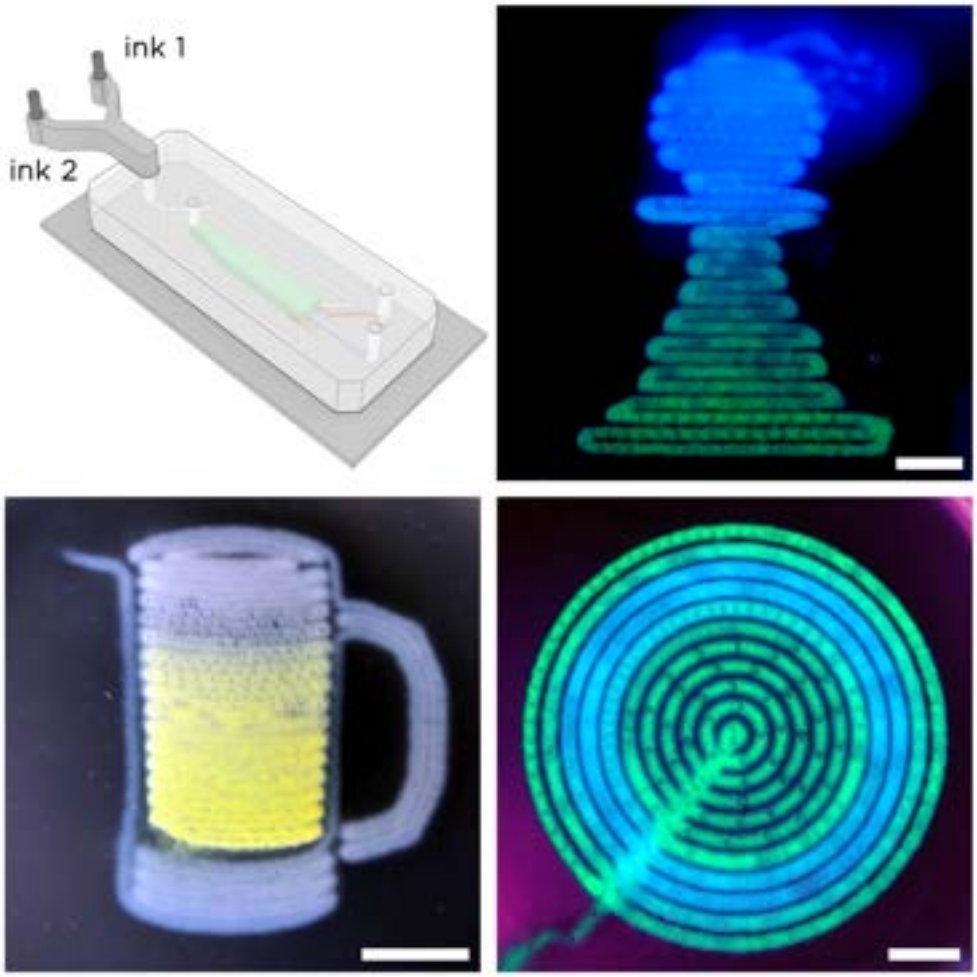

Figure 5.4: Multimaterial printing. **a**) Scheme of the chip with the two-channel inlet split to introduce two different inks. **b**), **c**) and **d**) three different shapes with color changes obtained switching the ink of the outer phase during printing. Scale bars corresponding to 5 mm.

5.4 Conclusions

In this chapter, we described the utilization of the apparatus outlined in Chapter 4 to engage in the 3D printing of functionally graded materials. By integrating the device with a custom 3D printer, we successfully generated porous materials that exhibited variations in both porosity and material composition. Through the process of extruding emulsion into an agarose gel support bath, followed by exposure to UV light for polymerization, we obtained self-sustaining 3D structures capable of being extracted from the bath.

Our efforts not only substantiate the adaptability of the Tuna-step design for 3D emulsion printing and materials science but also unlock possibilities for an extended array of future applications.

We believe that enhancing the throughput of our technology via extensive parallelization stands as a pragmatic prospect. This potential advancement could significantly amplify its impact, particularly in the realm of producing porous materials, even within industrial settings.

6
Conclusions

Within this thesis, I illustrated the remarkable versatility and ease of customization of microfluidics, adapting current technologies or designing new ones for diverse applications in different sectors of biotechnology. Each application resulted in a relevant project that is summarised in a chapter within this thesis.

1. In Chapter 2 I discussed the development of a method for the precise quantification of drug uptake time in cancer cells. This method was obtained from the combination of Time-Correlated Single-Photon Counting with a microfluidic chip for the precise control of the flow of reagents that employed on-chip microvalves.

2. In Chapter 3 I described the the isolation and cultivation of bacterial representatives of interest from the human gut microbiota, obtained with a microfluidics-based workflow that included the high-throughput encapsulation of single bacterial cells in droplets

3. In Chapter 4 I reported a novel microfluidic device for the generation of droplets with a dynamic volume range, where microfluidic step emulsification was combined with on-chip microvalve technology

4. In Chapter 5 I illustrated the generation of functionally graded porous hydrogels with a high level of customization, by leveraging the intrinsic advantages of the developed microfluidic device described in Chapter 4 and combining it with a custom 3D printer.

Digging deeper into the projects, it is possible to highlight not only the achievement of noteworthy results but also the successful resolution of practical challenges related with the most intricate technical aspects of research.
In the first project we reported the measure of cellular uptake time with an unprecedented resolution of hundreds of microseconds. Performing these

measurements required not only to create a custom microfluidic chip for the precise and controlled drug delivery, but also to synchronise the signal acquisition with the automated execution of the experiments. Within this project I solved technical challenges in the creation of the setup, the design of the software, and the definition of standard operational procedures to prepare consistent series of more than 100 microfluidic modules with a reduced rate of failure.

In the second project we isolated and cultured 199 different bacterial species from the human gut microbiota, including rare species of interest. The procedure would not have been possible without the integration of microfluidics within the workflow. To this aim, I developed a microfluidic chip that could generate droplets with a high-throughput regardless of the flow rates applied (until a critycal value), and therefore more stable within the anaerobic chamber where the experiments were carried on. Moreover, I performed the analysis reported within this thesis, dealing with the representation of the extensive database of isolates within simplified figures.

In the third project we reported a novel microfluidic design that showed for the first time a tunable step-emulsification where the emulsifying nozzle is dynamically changed to regulate the droplet size regardless of the flow rate (until a critycal value). The definition of the capabilities of such system required not only an extensive calibration, but most importantly an iterative optimization process through several versions of nozzles and chips. This system was tested for both Oil-in-Water and Water-in-Oil droplet generation, requiring the developement of a novel surface modification resistant to hexadecane and hydrophilic. The parallelization of the system required even more tests, including the development of double nozzles and multiple nozzle designs.

Finally, in the fourth project, we presented a relevant application of the aforementioned tunable step device for the synthesis of highly customizable porous structures in 2.5D and 3D. Not only we showed a excellent control

of gradients of porosity and multi-material printing, but we also displayed the generation of different patterns on the plane. This project required the precise coordination between the flow of the reagents, the emulsion generation, and the movement of the printing nozzle on the XYZ directions. Moving the chip in unconventional patterns required a non-standard procedure for designing the path on CAD and exporting the commands to the printer through Inkscape.

Altogether, these projects demonstrate the validity of this thesis and of the work carried on during my PhD studies under different aspects, including

(i) originality of the proposed solutions, including contributions to the fields of microfluidics, drug discovery, microbiology and biomaterial engineering;

(ii) impact of the research addressing relevant challenges in these areas;

(iii) interdisciplinary nature of the research, combining physics with engineering, biology, and materials science, and fostering collaboration and integration of diverse perspectives in different fields

(iv) technical proficiency demonstrated through the successful development and integration of several microfluidic technologies like on-chip valves and droplet generation techniques, the implementation of microfluidics within custom setups and workflows, the design of setup and software, and the analysis of data.

In conclusion, I present the outcomes of my doctoral thesis as concrete evidence of my dedication and contributions to my field of study. I humbly request the consideration and evaluation of this thesis by the Scientific Committee, with the fervent hope of being awarded a well-deserved Ph.D. degree.

References

[1] Pijush K. Kundu, Ira M. Cohen, and David R. Dowling. *Fluid mechanics: Sixth edition*. Elsevier, 2015, pp. 1–921.

[2] E M Purcell. "Life at Low Reynolds Number". In: *American Journal of Physics* 45 (1977), pp. 3–11.

[3] Pierre-Gilles de Gennes, Françoise Brochard-Wyart, and David Quéré. "Capillarity and Wetting Phenomena". In: *Capillarity and Wetting Phenomena* (2004).

[4] George M. Whitesides. "The origins and the future of microfluidics". In: *Nature 2006 442:7101* 442.7101 (2006), pp. 368–373.

[5] Younan Xia and George M. Whitesides. "SOFT LITHOGRAPHY". In: *https://doi.org/10.1146/annurev.matsci.28.1.153* 28.1 (2003), pp. 153–184.

[6] Patrick M. Winter et al. "Photolithography". In: *Encyclopedia of Nanotechnology* (2012), pp. 2051–2060.

[7] Qiming Chen et al. "Fabrication of multi-layer SU-8 microstructures". In: *Journal of Micromechanics and Microengineering* 16 (2006), pp. 276–284.

[8] David J. Guckenberger et al. "Micromilling: a method for ultra-rapid prototyping of plastic microfluidic devices". In: *Lab on a Chip* 15.11 (2015), pp. 2364–2378.

[9] Rafael R. Gattass and Eric Mazur. "Femtosecond laser micromachining in transparent materials". In: *Nature Photonics 2008 2:4* 2.4 (2008), pp. 219–225.

[10] Todd M. Squires and Stephen R. Quake. "Microfluidics: Fluid physics at the nanoliter scale". In: *Reviews of Modern Physics* 77.3 (2005), pp. 977–1026.

[11] Milton J. Rosen. “Surfactants and Interfacial Phenomena”. In: *Surfactants and Interfacial Phenomena* (2004).

[12] J. Bibette et al. “Stability criteria for emulsions”. In: *Physical Review Letters* 69.16 (1992), p. 2439.

[13] J. Bibette, F. Leal Calderon, and P. Poulin. “Emulsions: basic principles”. In: *Reports on Progress in Physics* 62.6 (1999), p. 969.

[14] Jean-Christophe Baret and Jean-Christophe Baret Surfactants. “Surfactants in droplet-based microfluidics”. In: *Lab on a Chip* 12.3 (2012).

[15] Bing Dai and L. Gary Leal. “The mechanism of surfactant effects on drop coalescence”. In: *Physics of Fluids* 20.4 (2008).

[16] Thomas Krebs, Karin Schroën, and Remko Boom. “Coalescence dynamics of surfactant -stabilized emulsions studied with microfluidics”. In: *Soft Matter* 8.41 (2012), pp. 10650–10657.

[17] P. Taylor. “Ostwald ripening in emulsions”. In: *Advances in Colloid and Interface Science* 75.2 (1998), pp. 107–163.

[18] Yunpeng Bai et al. “A double droplet trap system for studying mass transport across a droplet-droplet interface”. In: *Lab on a Chip* 10.10 (2010), pp. 1281–1285.

[19] Diego Romano Perinelli et al. “Surfactant Self-Assembling and Critical Micelle Concentration: One Approach Fits All?” In: *Langmuir* 36.21 (2020), pp. 5745–5753.

[20] L. Spencer Roach, Helen Song, and Rustem F. Ismagilov. “Controlling nonspecific protein adsorption in a plug-based microfluidic system by controlling interfacial chemistry using fluorous-phase surfactants”. In: *Analytical Chemistry* 77.3 (2005), pp. 785–796.

[21] C. Holtze et al. “Biocompatible surfactants for water-in-fluorocarbon emulsions”. In: *Lab on a Chip* 8.10 (2008), pp. 1632–1639.

[22] Mohammad Suman Chowdhury et al. “Dendronized fluorosurfactant for highly stable water-in-fluorinated oil emulsions with minimal inter-droplet transfer of small molecules”. In: *Nature Communications 2019 10:1* 10.1 (2019), pp. 1–10.

[23] Jenifer Clausell-Tormos et al. “Droplet-based microfluidic platforms for the encapsulation and screening of Mammalian cells and multicellular organisms”. In: *Chemistry & biology* 15.5 (2008), pp. 427–437.

[24] K. P. Johnston et al. “Toxicology of a PFPE Surfactant”. In: *Science* 272.5269 (1996), 1726b–1726b.

[25] Jinwen Zhou, Amanda Vera Ellis, and Nicolas Hans Voelcker. “Recent developments in PDMS surface modification for microfluidic devices”. In: *ELECTROPHORESIS* 31.1 (2010), pp. 2–16.

[26] Qin Tu et al. “Surface modification of poly(dimethylsiloxane) and its applications in microfluidics-based biological analysis”. In: *Reviews in Analytical Chemistry* 31.3-4 (2012), pp. 177–192.

[27] Jonathan A. Vickers, Meghan M. Caulum, and Charles S. Henry. “Generation of hydrophilic poly(dimethylsiloxane) for high-performance microchip electrophoresis”. In: *Analytical Chemistry* 78.21 (2006), pp. 7446–7452.

[28] Raffaella Suriano et al. “Femtosecond laser ablation of polymeric substrates for the fabrication of microfluidic channels”. In: *Applied Surface Science* 257.14 (2011), pp. 6243–6250.

[29] Sajjad H. Maruf et al. “Use of nanoimprinted surface patterns to mitigate colloidal deposition on ultrafiltration membranes”. In: *Journal of Membrane Science* 428 (2013), pp. 598–607.

[30] Jörg F. Friedrich et al. “New Plasma Techniques for Polymer Surface Modification with Monotype Functional Groups”. In: *Plasma Processes and Polymers* 5.5 (2008), pp. 407–423.

[31] Adam R. Abate et al. “Glass coating for PDMS microfluidic channels by sol–gel methods”. In: *Lab on a Chip* 8.4 (2008), pp. 516–518.

[32] Guodong Sui et al. “Solution-phase surface modification in intact poly(dimethylsiloxane) microfluidic channels”. In: *Analytical Chemistry* 78.15 (2006), pp. 5543–5551.

[33] Witold Postek et al. “Microfluidic screening of antibiotic susceptibility at a single-cell level shows the inoculum effect of cefotaxime on: E. coli”. In: *Lab on a Chip* 18.23 (2018), pp. 3668–3677.

[34] Piotr Garstecki et al. “Formation of droplets and bubbles in a microfluidic T-junction—scaling and mechanism of break-up”. In: *Lab on a Chip* 6.3 (2006), pp. 437–446.

[35] Krzysztof Churski, Piotr Korczyk, and Piotr Garstecki. “High-throughput automated droplet microfluidic system for screening of reaction conditions”. In: *Lab on a Chip* 10.7 (2010), pp. 816–818.

[36] Piotr Garstecki, Howard A. Stone, and George M. Whitesides. “Mechanism for flow-rate controlled breakup in confined geometries: A route to monodisperse emulsions”. In: *Physical Review Letters* 94.16 (2005), p. 164501.

[37] Christophe Serra et al. “A predictive approach of the influence of the operating parameters on the size of polymer particles synthesized in a simplified microfluidic system”. In: *Langmuir* 23.14 (2007), pp. 7745–7750.

[38] Adrien Dewandre et al. “Microfluidic droplet generation based on non-embedded co-flow-focusing using 3D printed nozzle”. In: *Scientific Reports 2020 10:1* 10.1 (2020), pp. 1–17. arXiv: 2002.06909.

[39] E. Amstad et al. “Robust scalable high throughput production of monodisperse drops”. In: *Lab on a Chip* 16.21 (2016), pp. 4163–4172.

[40] Jean Christophe Baret et al. “Fluorescence-activated droplet sorting (FADS): Efficient microfluidic cell sorting based on enzymatic activity”. In: *Lab on a Chip* 9.13 (2009), pp. 1850–1858.

[41] Kirk Mutafopulos et al. “Selective cell encapsulation, lysis, picoinjection and size-controlled droplet generation using traveling surface acoustic waves in a microfluidic device”. In: *Lab on a Chip* 20.21 (2020), pp. 3914–3921.

[42] Lothar Schmid, David A. Weitz, and Thomas Franke. “Sorting drops and cells with acoustics: Acoustic microfluidic fluorescence-activated cell sorter”. In: *Lab on a Chip* 14.19 (2014), pp. 3710–3718.

[43] Adam R Abate and David A Weitz. “Lab on a Chip Faster multiple emulsification with drop splitting”. In: (2011), pp. 1911–1915.

[44] David W. Inglis et al. “Critical particle size for fractionation by deterministic lateral displacement”. In: *Lab on a Chip* 6.5 (2006), pp. 655–658.

[45] Gabriel Amselem et al. “Universal microfluidic platform for bioassays in anchored droplets”. In: *Lab on a Chip* 16.21 (2016), pp. 4200–4211.

[46] Ciro Semprebon et al. “Deviation of sliding drops at a chemical step”. In: *Soft Matter* 12.40 (2016), pp. 8268–8273.

[47] Andrea Montessori et al. “Elucidating the mechanism of step emulsification”. In: *Physical Review Fluids* 7.3 (2018), pp. 1–7. arXiv: 2006.11065.

[48] Andrea Montessori et al. “Jetting to dripping transition: Critical aspect ratio in step emulsifiers”. In: *Physics of Fluids* 31.2 (2019).

[49] Shinji Sugiura et al. “Interfacial Tension Driven Monodispersed Droplet Formation from Microfabricated Channel Array”. In: *Langmuir* 17.18 (2001), pp. 5562–5566.

[50] Rémi Dangla et al. “The physical mechanisms of step emulsification”. In: *Journal of Physics D: Applied Physics* 46.11 (2013), p. 114003.

[51] Chengxiang He et al. “Droplet formation in a step-emulsification microdevice: effect of fluid’s viscosity”. In: *Chemical Engineering and Processing - Process Intensification* 185 (2023), p. 109309.

[52] Yu Kai Lai et al. “A double-step emulsification device for direct generation of double emulsions”. In: *Soft Matter* 18.33 (2022), pp. 6157–6166.

[53] M. L. Eggersdorfer et al. “Tandem emulsification for high-throughput production of double emulsions”. In: *Lab on a Chip* 17.5 (2017), pp. 936–942.

[54] W. Postek, T. S. Kaminski, and P. Garstecki. “A passive microfluidic system based on step emulsification allows the generation of libraries of nanoliter-sized droplets from microliter droplets of varying and known concentrations of a sample”. In: *Lab on a Chip* 17.7 (2017), pp. 1323–1331.

[55] Joseph Michael de Rutte, Jaekyung Koh, and Dino Di Carlo. "Scalable High-Throughput Production of Modular Microgels for In Situ Assembly of Microporous Tissue Scaffolds". In: *Advanced Functional Materials* 29.25 (2019), p. 1900071.

[56] Marc A. Unger et al. "Monolithic microfabricated valves and pumps by multilayer soft lithography". In: *Science* 288.5463 (2000), pp. 113–116.

[57] Mark A. Eddings, Michael A. Johnson, and Bruce K. Gale. "Determining the optimal PDMS-PDMS bonding technique for microfluidic devices". In: *Journal of Micromechanics and Microengineering* 18.6 (2008).

[58] Carlo S. Effenhauser et al. "Integrated Capillary Electrophoresis on Flexible Silicone Microdevices: Analysis of DNA Restriction Fragments and Detection of Single DNA Molecules on Microchips". In: *Analytical Chemistry* 69.17 (1997), pp. 3451–3457.

[59] Mark A. Eddings and Bruce K. Gale. "A PDMS-based gas permeation pump for on-chip fluid handling in microfluidic devices". In: *Journal of Micromechanics and Microengineering* 16.11 (2006), p. 2396.

[60] Srinath Satyanarayana, Rohit N. Karnik, and Arunava Majumdar. "Stamp-and-stick room-temperature bonding technique for microdevices". In: *Journal of Microelectromechanical Systems* 14.2 (2005), pp. 392–399.

[61] Björn Samel, M. Kamruzzaman Chowdhury, and Göran Stemme. "The fabrication of microfluidic structures by means of full-wafer adhesive bonding using a poly(dimethylsiloxane) catalyst". In: *Journal of Micromechanics and Microengineering* 17.8 (2007), p. 1710.

[62] F. H.C. Crick and A. F.W. Hughes. "The physical properties of cytoplasm: A study by means of the magnetic particle method Part I. Experimental". In: *Experimental Cell Research* 1.1 (1950), pp. 37–80.

[63] Jean L. Marx. "Organizing the cytoplasm". In: *Science* 222.4628 (1983), pp. 1109–1111.

[64] Howard Gest. "The discovery of microorganisms by Robert Hooke and Antoni van Leeuwenhoek, Fellows of The Royal Society". In: *Notes and Records of the Royal Society of London* 58.2 (2004), pp. 187–201.

[65] Andrew I. Minchinton and Ian F. Tannock. "Drug penetration in solid tumours". In: *Nature reviews. Cancer* 6.8 (2006), pp. 583–592.

[66] Tianyu Liu et al. "Quantitatively Mapping Cellular Viscosity with Detailed Organelle Information via a Designed PET Fluorescent Probe". In: *Scientific Reports 2014 4:1* 4.1 (2014), pp. 1–7.

[67] Tomasz Kalwarczyk et al. "Comparative analysis of viscosity of complex liquids and cytoplasm of mammalian cells at the nanoscale". In: *Nano Letters* 11.5 (2011), pp. 2157–2163.

[68] Karina Kwapiszewska et al. "Nanoscale Viscosity of Cytoplasm Is Conserved in Human Cell Lines". In: *Journal of Physical Chemistry Letters* 11.16 (2020), pp. 6914–6920.

[69] Marta Pilz et al. "Transport of nanoprobes in multicellular spheroids". In: *Nanoscale* 12.38 (2020), pp. 19880–19887.

[70] Ruimin Xing et al. "Characterization and cellular uptake of platinum anticancer drugs encapsulated in apoferritin". In: *Journal of Inorganic Biochemistry* 103.7 (2009), pp. 1039–1044.

[71] Sai Manasa Jandhyala et al. "Role of the normal gut microbiota". In: *World Journal of Gastroenterology : WJG* 21.29 (2015), p. 8787.

[72] Junjie Qin et al. "A human gut microbial gene catalogue established by metagenomic sequencing". In: *Nature 2010 464:7285* 464.7285 (2010), pp. 59–65.

[73] Wing Yin Cheng, Chun Ying Wu, and Jun Yu. "The role of gut microbiota in cancer treatment: friend or foe?" In: *Gut* 69.10 (2020), pp. 1867–1876.

[74] Ana Larroya-García et al. "Impact of gut microbiota on neurological diseases: Diet composition and novel treatments". In: *Critical Reviews in Food Science and Nutrition* 59.19 (2018), pp. 3102–3116.

[75] Attila Bodor et al. "Challenges of unculturable bacteria: environmental perspectives". In: *Reviews in Environmental Science and Bio/Technology 2020 19:1* 19.1 (2020), pp. 1–22.

[76] Alan W. Walker et al. “Phylogeny, culturing, and metagenomics of the human gut microbiota”. In: *Trends in microbiology* 22.5 (2014), pp. 267–274.

[77] Eric J. Stewart. “Growing unculturable bacteria”. In: *Journal of Bacteriology* 194.16 (2012), pp. 4151–4160.

[78] Doris Vandeputte et al. “Stool consistency is strongly associated with gut microbiota richness and composition, enterotypes and bacterial growth rates”. In: *Gut* 65.1 (2016), pp. 57–62.

[79] S. S. Epstein. “The phenomenon of microbial uncultivability”. In: *Current Opinion in Microbiology* 16.5 (2013), pp. 636–642.

[80] Curtis Huttenhower et al. “Structure, function and diversity of the healthy human microbiome”. In: *Nature 2012 486:7402* 486.7402 (2012), pp. 207–214.

[81] Alexandre Almeida et al. “A new genomic blueprint of the human gut microbiota”. In: *Nature* 568.7753 (2019), pp. 499–504.

[82] Stephanie L. Schnorr et al. “Gut microbiome of the Hadza hunter-gatherers”. In: *Nature Communications* 5 (2014).

[83] Lawrence A. David et al. “Diet rapidly and reproducibly alters the human gut microbiome”. In: *Nature* 505.7484 (2014), pp. 559–63.

[84] Dirk Gevers et al. “The treatment-naive microbiome in new-onset Crohn’s disease”. In: *Cell host & microbe* 15.3 (2014), pp. 382–392.

[85] Rob Knight et al. “The Microbiome and Human Biology”. In: *https://doi.org/10.1146/annurev-genom-083115-022438* 18 (2017), pp. 65–86.

[86] Nan Zhou et al. “Harnessing microfluidic streak plate technique to investigate the gut microbiome of Reticulitermes chinensis”. In: *MicrobiologyOpen* 8.3 (2019).

[87] Karsten Zengler et al. “Cultivating the uncultured”. In: *Proceedings of the National Academy of Sciences of the United States of America* 99.24 (2002), pp. 15681–15686.

[88] Armand E.K. Dichosa et al. “Capturing and cultivating single bacterial cells in gel microdroplets to obtain near-complete genomes”. In: *Nature Protocols 2014 9:3* 9.3 (2014), pp. 608–621.

[89] Fu Yousi et al. “Evaluation of the effects of four media on human intestinal microbiota culture in vitro”. In: *AMB Express* 9.1 (2019), pp. 1–10.

[90] Andrew L Goodman et al. “Extensive personal human gut microbiota culture collections characterized and manipulated in gnotobiotic mice”. In: 108.15 (2011).

[91] William J. Watterson et al. “Droplet-based high-throughput cultivation for accurate screening of antibiotic resistant gut microbes”. In: *eLife* 9 (2020), pp. 1–22.

[92] Melanie Tramontano et al. “Nutritional preferences of human gut bacteria reveal their metabolic idiosyncrasies”. In: *Nature Microbiology 2018 3:4* 3.4 (2018), pp. 514–522.

[93] Anna Pryszlak et al. “Enrichment of gut microbiome strains for cultivation-free genome sequencing using droplet microfluidics”. In: *Cell Reports Methods* 2.1 (2022), p. 100137. arXiv: 2106.01455.

[94] Cheng Ying Jiang et al. “High-throughput single-cell cultivation on microfluidic streak plates”. In: *Applied and Environmental Microbiology* 82.7 (2016), pp. 2210–2218.

[95] Jianan Yin et al. “A droplet-based microfluidic approach to isolating functional bacteria from gut microbiota”. In: *Frontiers in Cellular and Infection Microbiology* 12.August (2022), pp. 1–12.

[96] Jennifer T. Lau et al. “Capturing the diversity of the human gut microbiota through culture-enriched molecular profiling”. In: *Genome Medicine* 8.1 (2016), pp. 1–10.

[97] Thomas C.A. Hitch et al. “Recent advances in culture-based gut microbiome research”. In: *International Journal of Medical Microbiology* 311.3 (2021), p. 151485.

[98] J. C. Lagier et al. “Microbial culturomics: paradigm shift in the human gut microbiome study”. In: *Clinical Microbiology and Infection* 18.12 (2012), pp. 1185–1193.

[99] Jean Christophe Lagier et al. “Culture of previously uncultured members of the human gut microbiota by culturomics”. In: *Nature Microbiology 2016 1:12* 1.12 (2016), pp. 1–8.

[100] Hilary P. Browne et al. “Culturing of ’unculturable’ human microbiota reveals novel taxa and extensive sporulation”. In: *Nature* 533.7604 (2016), pp. 543–546.

[101] Ami Diakite et al. “Optimization and standardization of the culturomics technique for human microbiome exploration”. In: *Scientific Reports 2020 10:1* 10.1 (2020), pp. 1–7.

[102] Melhem Bilen et al. “The contribution of culturomics to the repertoire of isolated human bacterial and archaeal species”. In: *Microbiome* 6.1 (2018), pp. 1–11.

[103] Maryam Tidjani Alou et al. “State of the art in the culture of the human microbiota: New interests and strategies”. In: *Clinical Microbiology Reviews* 34.1 (2020), pp. 1–21.

[104] Lisa Mahler et al. “Highly parallelized droplet cultivation and prioritization on antibiotic producers from natural microbial communities”. In: *eLife* 10 (2021).

[105] Ott Scheler, Witold Postek, and Piotr Garstecki. “Recent developments of microfluidics as a tool for biotechnology and microbiology”. In: *Current Opinion in Biotechnology* 55 (2019), pp. 60–67.

[106] Logan W. Macintyre et al. “An Ichip-Domesticated Sponge Bacterium Produces an N-Acyltyrosine Bearing an α-Methyl Substituent”. In: *Organic Letters* 21.19 (2019), pp. 7768–7771.

[107] Losee L. Ling et al. “A new antibiotic kills pathogens without detectable resistance”. In: *Nature 2015 517:7535* 517.7535 (2015), pp. 455–459.

[108] Martina Marcotulli et al. “Microfluidic 3D Printing of Emulsion Ink for Engineering Porous Functionally Graded Materials”. In: *Advanced Materials Technologies* 2201244 (2022), pp. 1–12.

[109] Gianluca Cidonio et al. “3D printing of biphasic inks: beyond single-scale architectural control”. In: *Journal of Materials Chemistry C* 9.37 (2021), pp. 12489–12508.

[110] Jonas Elsing, Aggeliki Quell, and Cosima Stubenrauch. “Toward Functionally Graded Polymer Foams Using Microfluidics”. In: *Advanced Engineering Materials* 19.8 (2017), p. 1700195.

[111] Marco Costantini et al. “3D-Printing of Functionally Graded Porous Materials Using On-Demand Reconfigurable Microfluidics”. In: *Angewandte Chemie International Edition* 58.23 (2019), pp. 7620–7625.

[112] Philipp Weber et al. “Microfluidic bubble-generator enables digital light processing 3D printing of porous structures”. In: *Aggregate* (2023), e409.

[113] Merve Yuce et al. “Live Cell Imaging of Peptide Uptake Using a Microfluidic Platform”. In: *International Journal of Peptide Research and Therapeutics* May (2021).

[114] Stefan Bálint et al. “Diffusion and cellular uptake of drugs in live cells studied with surface-enhanced Raman scattering probes”. In: *https://doi.org/10.1117/1.3369844* 15.2 (2010), p. 027005.

[115] Todd Thorsen, Sebastian J. Maerkl, and Stephen R. Quake. “Microfluidic large-scale integration”. In: *Science* 298.5593 (2002), pp. 580–584.

[116] Sasan Jalili-Firoozinezhad et al. “A complex human gut microbiome cultured in an anaerobic intestine-on-a-chip”. In: *Nature Biomedical Engineering 2019 3:7* 3.7 (2019), pp. 520–531.

[117] Max M. Villa et al. “Interindividual Variation in Dietary Carbohydrate Metabolism by Gut Bacteria Revealed with Droplet Microfluidic Culture”. In: *mSystems* 5.3 (2020).

[118] Anthony A. Fodor et al. “The “Most Wanted” Taxa from the Human Microbiome for Whole Genome Sequencing”. In: *PLOS ONE* 7.7 (2012), e41294.

[119] Sebastian D. Burz et al. “A Guide for Ex Vivo Handling and Storage of Stool Samples Intended for Fecal Microbiota Transplantation”. In: *Scientific Reports 2019 9:1* 9.1 (2019), pp. 1–16.

[120] David J. Collins et al. “The Poisson distribution and beyond: Methods for microfluidic droplet production and single cell encapsulation”. In: *Lab on a Chip* 15.17 (2015), pp. 3439–3459.

[121] Benjamin J. Callahan et al. “DADA2: High resolution sample inference from Illumina amplicon data”. In: *Nature methods* 13.7 (2016), p. 581.

[122] Christian Quast et al. “The SILVA ribosomal RNA gene database project: improved data processing and web-based tools”. In: *Nucleic Acids Research* 41.D1 (2013), pp. D590–D596.

[123] R Core Team. “R: A Language and Environment for Statistical Computing”. In: *R Foundation for Statistical Computing* Vienna, Au (2022).

[124] Guangchuang Yu. “Using ggtree to Visualize Data on Tree-Like Structures”. In: *Current Protocols in Bioinformatics* 69.1 (2020), e96.

[125] Rene Brun and Fons Rademakers. “ROOT — An object oriented data analysis framework”. In: *Nuclear Instruments and Methods in Physics Research Section A: Accelerators, Spectrometers, Detectors and Associated Equipment* 389.1-2 (1997), pp. 81–86.

[126] Nicola Segata et al. “Composition of the adult digestive tract bacterial microbiome based on seven mouth surfaces, tonsils, throat and stool samples”. In: (2012).

[127] James J. Kozich et al. “Development of a dual-index sequencing strategy and curation pipeline for analyzing amplicon sequence data on the miseq illumina sequencing platform”. In: *Applied and Environmental Microbiology* 79.17 (2013), pp. 5112–5120.

[128] Alexandre Almeida et al. “A unified catalog of 204,938 reference genomes from the human gut microbiome”. In: *Nature Biotechnology 2020 39:1* 39.1 (2020), pp. 105–114.

[129] Johannes Schindelin et al. “Fiji: an open-source platform for biological-image analysis”. In: *Nature Methods 2012 9:7* 9.7 (2012), pp. 676–682.

[130] David Legland, Ignacio Arganda-Carreras, and Philippe Andrey. “MorphoLibJ: integrated library and plugins for mathematical morphology with ImageJ”. In: *Bioinformatics* 32.22 (2016), pp. 3532–3534.

[131] Hadley Wickham et al. “Welcome to the Tidyverse”. In: *Journal of Open Source Software* 4.43 (2019), p. 1686.

[132] Yuan Sheng Lee, Nirveek Bhattacharjee, and Albert Folch. “3D-printed Quake-style microvalves and micropumps”. In: *Lab on a Chip* 18.8 (2018), pp. 1207–1214.

[133] Rémi Dangla, Franois Gallaire, and Charles N. Baroud. "Microchannel deformations due to solvent-induced PDMS swelling". In: *Lab on a Chip* 10.21 (2010), pp. 2972–2978.

[134] Michael C. McManus et al. "Mechanical properties of electrospun fibrinogen structures". In: *Acta Biomaterialia* 2.1 (2006), pp. 19–28.

[135] Daniel L. Matera et al. "Fiber Density Modulates Cell Spreading in 3D Interstitial Matrix Mimetics". In: *ACS Biomaterials Science and Engineering* 5.6 (2019), pp. 2965–2975.